Electronic State Distributions of $YBa_2Cu_3O_{7-x}$ Laser Ablated Plumes

DISSERTATION

Patrick D. Kee, Lieutenant Colonel, USAF

AFIT/DSP/ENP/08-S05

DEPARTMENT OF THE AIR FORCE
AIR UNIVERSITY

AIR FORCE INSTITUTE OF TECHNOLOGY

Wright-Patterson Air Force Base, Ohio

The views expressed in this dissertation are those of the author and do not reflect the official policy or position of the United States Air Force, Department of Defense, or the United States Government.

AFIT/DSP/ENP/08-S05

Electronic State Distributions of $YBa_2Cu_3O_{7-x}$ Laser Ablated Plumes

DISSERTATION

Presented to the Faculty

Graduate School of Engineering and Management

Air Force Institute of Technology

Air University

Air Education and Training Command

In Partial Fulfillment of the Requirements for the

Degree of Doctor of Philosophy

Patrick D. Kee, BA, MS

Lieutenant Colonel, USAF

September 2008

AFIT/DSP/ENP/08-S05

Electronic State Distributions of $YBa_2Cu_3O_{7-x}$ Laser Ablated Plumes

Patrick D. Kee, BA, MS
Lieutenant Colonel, USAF

Approved:

/signed/	25 Aug 2008
Glen P. Perram (Chairman)	Date
/signed/	25 Aug 2008
Anthony N. Palazotto (Dean's Representative)	Date
/signed/	25 Aug 2008
William F. Bailey (Member)	Date
/signed/	25 Aug 2008
David E. Weeks (Member)	Date
/signed/	25 Aug 2008
David A. Dolson (Member)	Date

Accepted:

/signed/	3 Sep 2008
M. U. Thomas Dean, Graduate School of Engineering and Management	Date

Abstract

The application of spectral and imagery diagnostics to $YBa_2Cu_3O_7$ (YBCO) laser-ablated plumes was systematically studied to determine their effectiveness for process control. Emission signatures were collected for plumes created by ablating bulk YBCO with a pulsed laser source. A KrF (λ=248 nm) laser source operating at 4-10 J/cm^2 at a 4-10 Hz pulse repetition frequency was used to ablate a bulk YBCO target at O_2 background pressures ranging from 50 to 400 mTorr. Emission spectra were collected over the 500 to 860 nm bandpass at distances from the target ranging from 31.4 to 55.0 mm. Of 87 observed emission lines, 76 were assigned to specific transitions with the aid of calibration lamps and reference to tables of energy levels. Line fluences were corrected for self-absorption, and electronic state distributions were calculated using the most recent NIST transition probabilities. Electronic temperatures ranged from 0.28 $\pm$ 0.01 eV to 0.37 $\pm$ 0.03 eV for yttrium, 0.28 $\pm$ 0.01 eV to 0.35 $\pm$ 0.03 eV for barium, and 0.40 $\pm$ 0.02 eV to 0.48 $\pm$ 0.05 eV for copper, and are consistent with prior reported results. These results were relatively insensitive to position and oxygen background pressure. Imagery data obtained with a spectrally-filtered intensified CCD camera was used to determine plume velocities, shock strengths, and time-of-flight curves. A model using the time-of-flight data was developed to investigate the possible effect of time-varying temperatures and number densities on time-integrated electronic state distributions. This model predicted a slight elevation of Cu temperatures compared to Ba, however, the difference was not sufficient to explain experimental results. Surprisal analysis of Y, Ba, and Cu neutral emission spectra resulted in linear constraints, consistent with an exponential gap law for electronic excitation, with a different constraint for each type of emitter.

Acknowledgements

My father once told me to never trust a carpenter with a shiny hammer. This was his way of saying that experience is important. Fortunately, in this effort I benefited from the support of many who were experts in key parts of this research.

First, I would like to thank my advisor, Dr. Glen Perram, for steering me onto this topic. This turned out to be an interesting effort, as I was able to exploit what I had learned in my 'day job' in the AFRL Electro-optics Division.

Next, I would like to thank my committee members, Dr William Bailey, Dr David Dolson, and Dr David Weeks, for their participation in this research. Their discussion and debate shaped the ultimate direction of this investigation

Also, I received significant support from the AFRL Materials Directorate, in particular from the late Dr. Rand Biggers and 1Lt Neil Fore who supported me by operating their PLD system. I am also thankful for Tim Peterson allowing me access to Dr Biggers' lab notebooks after his unfortunate passing.

I must also recognize a pair of fellow students. Like the fictional Harry Callahan, I've never worked well with a partner. Fortunately, I was given a very competent lab partner. Carl Druffner collected all imagery data and showed me how to use the spectrometer. His attention-to-detail was key to obtaining high quality data for this analysis. I would also thank Charles 'Dusty' Phelps, who wrote several Matlab™ scripts that I used to extract time-of-flight data from the imagery. This easily saved me several weeks of programming and debugging time.

I should also mention the support of my supervisors during this effort by thanking Mr. Chris Ristich, Mr. Barry Karch, Dr. Michael Bryant, and especially Dr. Adedeji Badiru for their generosity in giving me time to continue this effort.

Finally, I would like to thank my wife, friends, family, and coworkers for their moral support during this effort. For them, I am truly grateful.

Patrick D. Kee

Table of Contents

Page

List of Figures

List of Tables

Electronic State Distributions of $YBa_2Cu_3O_{7-x}$ Laser Ablated Plumes

I. Introduction

1.1 Background

The achievement of high current densities ($\sim$ 1 MA/cm^2) in high temperature superconductors such as $YBa_2Cu_3O_{7-x}$ (YBCO), [54, 69] has resulted in significant interest in maturation and transition of this technology for military and commercial applications. Unlike metal superconductors, ceramic superconductors such as YBCO can not be drawn into wires, and instead are deposited on buffered metal substrates using gas phase techniques such as pulsed laser deposition (PLD) or metal-oxide chemical vapor deposition (MOCVD). [69,76] Because it has been observed that samples of deposited YBCO grown under identical deposition equipment settings may result in materials with different characteristics, [83] *in situ* diagnostic techniques are desirable for deposition process control. Multiple diagnostic techniques have been used to characterize YBCO plumes produced in PLD, and can be categorized into two groups: time-of-flight measurements (to characterize the kinetic energy of the plume), and atomic and molecular spectroscopy (to determine plume composition and degree of internal excitation).

Time-of-flight measurements have included optical [25, 26, 36, 68] and ion probe time-of-flight measurements [29,38], which have been very successful at characterizing the kinetic energy of ablation plumes according to free streaming, drag, or shock models, depending on the stage of the plume evolution. [36] Spectroscopic techniques have included absorption [37] and emission spectroscopy [8–10, 27–29, 91], as well as laser induced fluorescence. [63] Spectroscopy has been very successful at identifying plume components, including atomic, ionic, and molecular, however, measurement and interpretation of excited state populations has resulted in conflicting results.

The central issue that has yet to be resolved in the interpretation of spectroscopic data is the apparent contradiction between the commonly accepted assumption of the existence of local thermodynamic equilibrium (LTE) in the plume and observed excited state distributions. [10, 27–29, 40, 90] The existence of LTE implies kinetic energies distributions are Maxwellian, state distributions are Boltzmann, ion particle densities given by the Saha equation, common temperatures among the various energy channels, and collisional processes dominate over radiative processes. [43] The LTE assumption is critical to the suitability of emission spectroscopy as a plume diagnostic, because its presence would establish a linkage between electronic state populations and the electron temperature. However, disagreement has been observed among electronic temperatures for different emitting species, [91] as well as the electronic, vibrational, and rotational populations within a single emitting species. [89] Attempts to explain the inconsistency between LTE and experimental results appear to lack sufficient rigor. [91]

In addition, the technique used in prior work is deficient in several aspects. First, many of the prior results were derived from a sparse sampling of spectral lines, or from line ratios. [8, 27–29] Second, most of the prior work predated the discovery of significant self-absorption in the plume, [72, 73] which could have significant consequences on electronic temperatures derived from line ratios if the self-absorption effect differs from line-to-line. Third, it has been asserted in the literature that temporal signal averaging effects may distort electronic temperatures calculated from spectral data if the plume temperature changes significantly during signal collection. [56] Finally, most of the prior work predates a significant revision in transition probabilities for many relevant emission lines. [51]

Because of the many experimental deficiencies in prior work, and the lack of follow-through on the apparent contradictions between assertion of the presence of LTE and measured electronic temperatures, emission spectroscopy of laser-ablated YBCO plumes is ripe for reexamination using a systematic experimental approach to

address prior deficiencies in technique, as well as a critical look at electronic excitation mechanisms in the plume.

1.2 Problem Statement

The purpose of this effort is to conduct a systematic measurement, analysis, and interpretation of electronic state distributions (ESDs) of Y, Ba, and Cu neutrals in plumes created by the pulsed laser ablation of bulk YBCO. Prior work in this topic is deficient with respect to spectral coverage, self-absorption, temporal effects, transition probabilities, and interpretation of results. Each of these deficiencies will be addressed in this work to provide the most thorough and systematic measurement and interpretation of ESDs in laser-ablated YBCO plumes.

ESDs will be determined from the emission spectra ($\lambda = 500$ - 860 nm) collected by a calibrated optical multichannel analyzer (OMA), under various conditions of oxygen gas background pressure and distance from the ablation target. Emission line assignments will be systematically performed using a combination of spectral calibration lamps and comparison to energy level diagrams. Corrections for self-absorption will be made prior to calculating upper state population levels. Also, the latest NIST-validated values will be used to calculate population levels.

ESDs will be interpreted in the context of a dynamically evolving plume. To this end, time-of-flight data collected on the YBCO plumes using gated, intensified CCD imagery will be analyzed to provide information on plume motion, including position, velocity, shock width, shock strength, and gas temperature. Possible correlations between ESDs and plume kinetic variables will be investigated with the goal of obtaining insight to electronic excitation mechanisms. In addition, time-of-flight waveforms will be used to evaluate temporal signal averaging effects on ESDs.

The spectral and time-of-flight data collection will provide the information needed to conduct a systematic analysis of electronic excitation mechanisms, specifically: whether it is justified to assume electron-impact under LTE is the dominant

electronic excitation mechanism in the plume. The answer to this question is essential to assessing whether emission spectroscopy is a suitable technique for process control of YBCO superconductor manufacturing.

II. Background

The context and motivation for this research effort can be explained by a review of prior developments in superconductivity, a review of YBCO properties, and prior work in YBCO PLD diagnostics.

2.1 Developments in Superconductivity

The discovery of superconductivity by Onnes in 1911 was an unexpected and serendipitous event that occurred as a result of exploiting emerging cryogenic technologies to test the classical theory of low temperature conductivity. [62] The development of the process for liquefying helium enabled Onnes to achieve temperatures as low as 4.2 K. [62] In this temperature regime, the prevailing classical theory of low temperature conductivity predicted a conductor would become highly resistive at sufficiently low temperatures because free electrons would freeze-out, depriving the conductor of charge carriers. [62] However, Onnes discovered solid Mercury, when cooled to 4.2 K, exhibited an abrupt drop in resistance. [62] Understanding the physical explanation of this phenomenon would await the development of quantum mechanics.

Superconductivity would soon be discovered in other metals including lead, pure niobium, and niobium alloys. [20] However, the next key step in understanding superconducting physics would be the discovery of the Meissner effect in 1933. In their work, Meissner and Ochsenfeld observed superconducting materials expelled magnetic fields from their interior. [33] This effect, in combination with negligible resistance below a transition (or critical) temperature would become the two defining properties of superconducting materials.

Discovery of the Meissner effect was soon followed by the development of the London equations, [55] which described the relationship between superconducting current density $\bar{J}_s$ and the electric and magnetic fields ($\bar{E}$ and $\bar{B}$). The first of these equations, referred to as the acceleration equation [55] and developed earlier by Becker, *et al*, [11] relates the time-rate of change of the superconducting current to the applied electric field:

$$\Lambda \frac{d\bar{J}}{dt} = \bar{E} \tag{2.1}$$

where $\Lambda = m/ne^2$, and m, n, and e, are respectively the mass, number density, and charge of the superconducting charge carriers. Unlike Ohm's Law, which states current is linearly proportional to the applied electric field, the first London equation says the *time-rate of change* of current is linearly proportional to the applied electric field. The corollary is that a supercurrent, once established, will continue to flow in the absence of an applied force.

The second of the London equations is derived from the first by taking the curl of both sides of the above equation, and invoking Faraday's Law, $\nabla \times \bar{E} = -\frac{1}{c}\frac{d\bar{B}}{dt}$: [55]

$$\nabla \times \Lambda \bar{J} = -\frac{1}{c}\bar{B} \tag{2.2}$$

The significance of the second London equation is seen when substituting Ampere's law ($\nabla \times \bar{H} = \frac{4\pi}{c}\bar{J}$), into the left-hand side, resulting in the following differential equation:

$$\nabla^2 \bar{H} - \frac{1}{\lambda^2}\bar{H} = 0 \tag{2.3}$$

where $\lambda = \frac{mc^2}{4\pi ne^2}$. The solution to this equation is an exponential decay, with the decay constant, or skin depth, equal to λ. At high number densities of charge carriers, the magnetic field is strongly attenuated at the skin of the superconductor, consistent with the observed Meissner effect. [85]

The next major theoretical development was the Ginzburg-Landau theory, (sometimes referred to as the ψ theory [41]), which successfully applied second-order phase transition theory to model the change from the normal to the superconducting state. [22] In this approach, the number density of superconducting charge carriers is represented as the amplitude-squared of a pseudowavefunction, ψ, and the free energy of

the system expressed as a virial expansion in ψ and $\nabla\psi$, with expansion coefficients α and β. An important result of this theory was the definition of the the coherence length, ξ, of the pseudowavefunction, ψ:

$$\xi = \sqrt{\frac{\hbar^2}{2m\,|\alpha|}} \tag{2.4}$$

The definition of a parameter, ξ, which defines a distance metric for superconducting behavior, and, the definition of a penetration depth, λ, of a magnetic field, the absence of which is necessary for a superconducting state, are combined in a derived parameter, κ, known as the Ginzburg-Landau, or GL parameter: [22]

$$\kappa = \frac{\lambda}{\xi} \tag{2.5}$$

which is useful in characterizing the degree of superconductivity in the presence of a magnetic field.

Further developments of the Ginzburg-Landau theory were made by Abrikosov, who investigated the consequences of high values of the GL parameter. [7] In this condition, applied magnetic fields are able to penetrate the material, however, instead of uniformly penetrating the material, the magnetic fields form a lattice of flux vortices. The superconducting state in these magnetic flux regions is destroyed, however, superconducting currents may still be carried in the regions surrounding the vortices. This condition is known as Type II superconductivity and is typically exhibited in alloys, while superconducting materials that completely expel magnetic fields are known as Type I superconductors, which are usually highly purified metals. [18]

Complementary to the thermodynamic approach of the Ginzburg-Landau theory, a microscopic theory of superconductivity, based on quantum mechanical concepts, was developed by Bardeen, Cooper, and Schrieffer. The BCS theory (named after the initials of the three creators) explained the drop in resistance as a quantum mechanical effect where conduction electrons of opposite spins are paired together

under a weak attractive force (resulting from low-amplitude oscillations in the bound-charge distribution) to form a 'quasi-particle' known as a Cooper Pair. [85] Cooper pairs have the property of having zero-spin, thus at low kinetic energies they exhibit the quantum mechanical properties of Bostons. [41] Unlike classical particles, the kinetic energies of bosons are quantized, and at low temperatures the forbidden energy regions are sufficiently spaced that random scattering rarely provides sufficient energy change to enable a transition from one allowed kinetic energy state to another. [21] Thus loss of kinetic energy to lattice scattering is forbidden, and without scattering to impede motion of the Cooper Pair, the material exhibits a dramatic drop in resistance.

The microscopic picture provided by the BCS theory provided a starting point for investigating material properties hospitable to superconductivity. Ginzburg proposed a mechanism for superconductivity in anisotropic, 2-dimensional sandwich media composed of alternating conducting and dielectric layers. [41] In this mechanism, excited bound electrons in the crystal lattice provide the polarizability needed to bind electrons into Cooper Pairs and creating a superfluid current. Although Ginzburg did not specifically prescribe cuprate oxides in his mechanism, it did anticipate by a few years the discovery of high temperature superconductivity. [41]

The first breakthrough towards high temperature superconductivity, commonly defined as a superconducting state at liquid nitrogen temperatures, came with Bednorz and Muller's discovery of superconductivity in LBCO at 28 K. [12] This was not much higher than the previous record of 23 K in Nb_3Ge, [35] but significance of the discovery was profound because it occurred in an oxide instead of a metal, which opened up a new category of materials for study. This discovery was soon followed by the discovery of superconducting $YBa_2Cu_3O_{7-x}$ (YBCO) with critical temperatures above 77 K, as well as other cuprate oxide-based superconductors. [18]

2.2 YBCO

YBCO is a Type II oxide superconductor that has been extensively studied for practical applications due to its ability to carry large supercurrents in the presence of a magnetic field at temperatures above that of liquid nitrogen. [78] The unit cell diagram for YBCO is presented in Figure 2.1. Examination of the diagram reveals a vertically stacked structure with an yttrium atom sandwiched between two barium atoms, with the heavy atoms separated by copper oxide planes. This anisotropic structure appears to be correlated with observed anisotropic supercurrent in the material. [53] The commonly held view in the literature is that copper oxide planes are responsible for the supercurrent [18,20], however, an alternate explanation has been offered, which credits charge reservoir layers for carrying supercurrent. [16,24] Finally, oxygen stoichiometry has been shown to be important in the superconducting behavior of $YBa_2Cu_3O_{7-\delta}$, with an optimum value of δ=0.12. [30]

Practical application of YBCO as a superconducting wire poses significant manufacturing problems. Because YBCO is a ceramic, it cannot be drawn into wire like a metal. In addition, the anisotropic direction of supercurrents requires establishing and maintaining a preferred grain orientation with the copper oxide planes aligned along the desired current direction. This grain orientation has been successfully achieved by depositing YBCO on a metal tape substrate coated with a buffer layer selected to favor crystal formation with the c-axis (Ba-Y-Ba axis) perpendicular to the substrate surface. [32] With the buffer layer in place, gas phase deposition techniques, such as metal organic chemical vapor deposition (MOCVD), and pulsed laser deposition (PLD), are used to deposit YBCO on the buffer layer.

2.3 Laser Ablation and Plume Evolution

The pulsed laser deposition process is performed in a vacuum chamber fitted with optical windows for admitting a UV laser beam and providing access to diagnostic instruments. A typical research PLD setup is shown in Figure 2.2. The bulk material

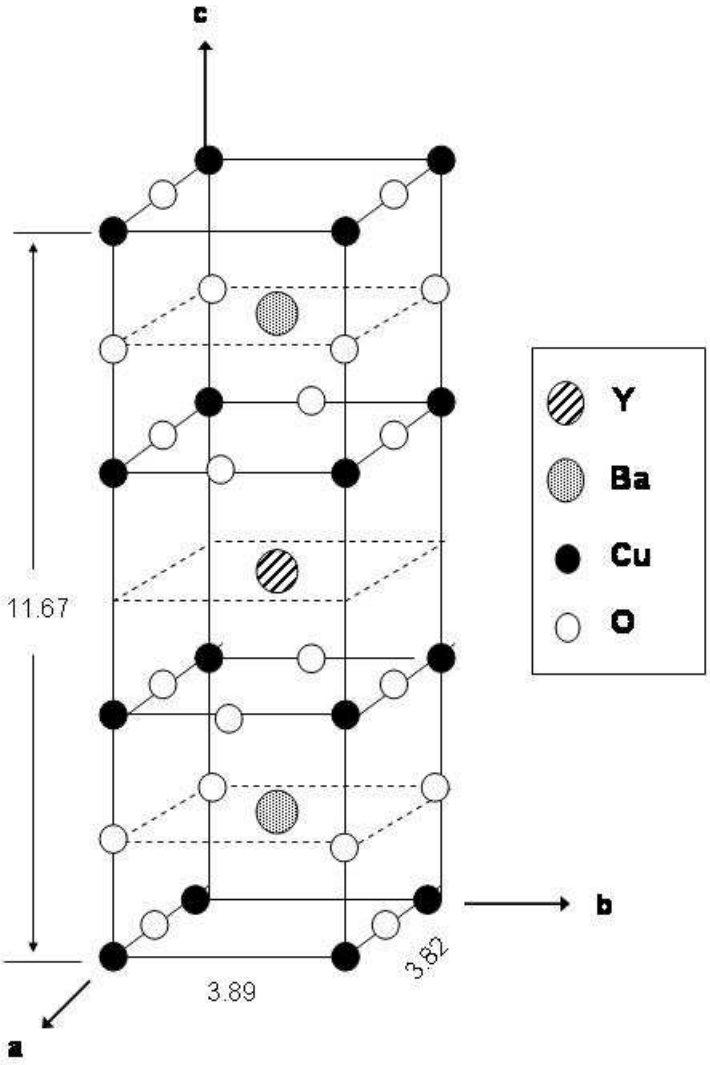

Figure 2.1: YBCO cell structure. Dimensions in Å.

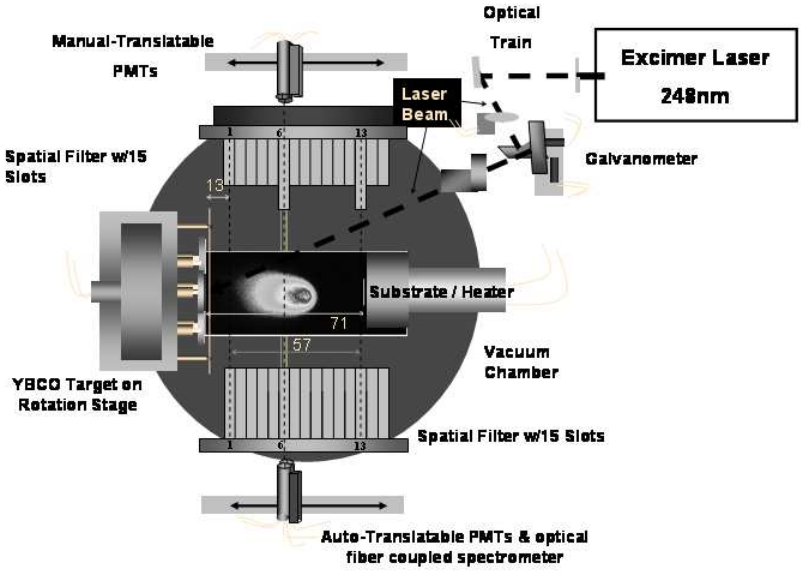

Figure 2.2: PLD apparatus. Dimensions in mm. Figure courtesy of AFRL/MLPS. Used with permission. [15]

ablation target is mounted at one end of the chamber, while the deposition substrate is mounted on the opposite end of the chamber. Ablation typically takes place in the presence of a background gas at pressures on the order of one-tenth of a torr. Background gases are important to the deposition process because of their role in shaping and confining the ablated plume, thermalizing and moderating the plume's kinetic energy for optimum surface mobility and nucleation, and for reactive gases, promoting chemical reactions in the plume. [78] The energy for ablating the surface of the target is typically provided by a pulsed excimer laser operating in the infrared (such as KrF at $\lambda = 248$nm or ArF at $\lambda = 193$ nm). The incident laser beam arrives at an angle away from normal, so a Gaussian laser beam will project an elliptical footprint on the ablation target.

The ablation of materiel from a target surface by a laser has been attributed to an electronic process. [50] The intense, time-varying fields cause the region at and near the surface of the target to change from a bonded to a non-bonded state resulting in the irradiated region changing from a solid to a gas. The gas is free to expand

at the surface of the ablation target and flows out of the ablation cavity. Because this occurs while the laser beam is still irradiating the target, there is significant interaction between the laser photons and the expanding gas. Laser photons are absorbed as their electric field accelerates charged particles in the expanding gas, resulting in significant heating because of collisions between the charged particles and neutrals. This inverse-Brehmsstrahlung process results in attenuation of the laser beam, decreasing the coupling efficiency between the laser and the target surface. [79]

After the termination of the laser pulse, the ablated material is free to expand into the vacuum chamber. In the absence of a background gas, the ablated material would leave the surface in a free-expansion, and the kinetic energy distribution would be dependent on the mechanism which caused the ablation. [50] However, YBCO deposition typically occurs in a background gas. Collisions occur between the ablated material and the background gas. This interaction results in an exchange of kinetic energy that changes the kinetic energy distribution of the plume. The leading, fast-moving particles in the ejecta are the first to collide with the background gas, and this typically occurs within a few mean free paths ($\lambda_{m.f.p.} \sim 1$ mm at 200 mTorr). The collisions not only slow down the leading edge of the ejecta, but also start to compress the background gas in front of the ejecta. The region where this occurs is referred to as the Knudsen Layer (KL). [50] It is in this region where the free streaming ejecta are compressed and shaped into a propagating plume. The effect of the random collisions on the plume is to obscure information on the ejection mechanism, [50] and move the plume's velocity distribution towards a form referred to as a modified Maxwellian, where the time-averaged velocity, v, is shifted by a streaming speed, u, which may be considered to be akin to a center-of-mass velocity: [49]

$$f(v)dv = Av^n exp\left(-\frac{m(v-u)^2}{kT}\right)dv \tag{2.6}$$

where the velocity, v = $\frac{x}{t}$ is the ratio of the distance from target x, t is time since ablation, and m is the mass of the emitting particle. Also, kT is a fitted parameter

that indicates the spread of the velocity distribution, while n = 3 or 4 depending on whether the observing instrument is an intensity or flux detector. [49] It should be emphasized here that equation 2.6 is an empirical velocity distribution, and should not be confused with the Maxwellian speed distribution:

$$f(v)dv = Av^2 exp\left(-\frac{m(v)^2}{kT}\right)dv \tag{2.7}$$

Instead the modified Maxwellian should be compared to the one-dimensional Maxwellian velocity distribution: [61]

$$f(v)dv = A\ exp\left(-\frac{m(v)^2}{kT}\right)dv \tag{2.8}$$

where the modified Maxwellian differs from the Maxwellian by the empirical factor of v^n and the streaming speed, u. The difference arises because the modified Maxwellian models directional motion in one dimension, while the Maxwellian velocity distribution models symmetric motion along an axis.

To fit the modified Maxwellian expression to time-of-flight data, the transformation v = x/t and dv = -(x/t^2) dt results in the following time-of-flight distribution curve:

$$f(t)dt = A\left(\frac{x}{t}\right)^n exp\left(-\frac{m(x/t-u)^2}{kT}\right)\left(\frac{-x}{t^2}\right)dt \tag{2.9}$$

where f(t) dt is the number of counts on the detector during the time interval dt.

Since the plume typically travels at high Mach numbers (M on the order of 10) compared to the background gas, [68] the boundary between the plume and background gas (referred to as the 'contact front' [50]) becomes a shock front. In addition, the compression of the background gas by the moving plume leads to creation of a shock wave in the background gas. The relationship between the velocities of the contact front and the background shock has been estimated by Kelly as: [50]

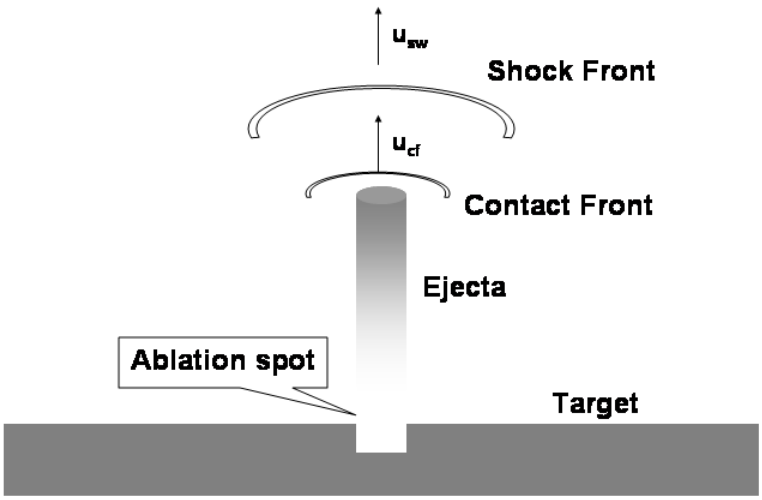

Figure 2.3: The plume is formed by the laser ablation of material from a bulk target. The interface between the plume and the background gas is referred to as the contact front, and moves at speed u_{cf}. There is a shocked region of background gas ahead of the contact front, and the shock wave moves through the background gas at a speed of u_{sw}.

$$u_{cf} \approx \frac{2u_{sw}}{\gamma + 1} \approx 0.83u_{sw} \geq 0.75u_{sw} \tag{2.10}$$

where the specific heat ratio (constant pressure to constant volume) is that of a diatomic, γ=1.4. This result implies that the background gas shock will recede from the contact front (see Figure 2.3). This phenomenon has been confirmed using high-speed photography. [50]

Insight into the structure and characteristics of the plume may be gained by considering several limiting cases and combining the results to create a composite picture. First, consider the case where the ablation occurs in the absence of a background gas. In this situation, the gas propagates in a free-expansion where the velocity, v, and plume kinetic temperature, T, are related by:

$$v = \frac{2}{\gamma - 1}\sqrt{\frac{\gamma kT}{M}} \tag{2.11}$$

where γ is the ratio of specific heats (≈ 1.2 or 1.3, depending on temperature as the electronic excitation and ionization degrees of freedom become significant), M is the species mass, and k is Boltzmann's constant. [70] Prior time-of-flight measurements of YBCO plumes in vacuum resulted in plume kinetic temperatures ~ 0.55 eV, which agree with electronic temperature measurements of the same plumes determined from yttrium intensity line ratios. [27]

The other case of interest is the contact front between the expanding plume and the background gas. The first step is to determine the velocity of the contact front as a function of time, as this will be used to compute temperatures and number densities immediately behind the contact front. Two approaches have been used to model the kinematic motion of the plume through the chamber: Sedov-Taylor (blast wave) and the drag model. The blast wave theory models the position of the plume front, r, as a function of time, t, with the equation:

$$r(t) = \xi_n \left(\frac{E_o}{\rho_b}\right)^{\frac{1}{n+2}} t^{\frac{2}{n+2}} \tag{2.12}$$

where E_o is the initial kinetic energy of the expansion, ρ_b is the mass density of the background gas, n = 1, 2, or 3 respectively for a planar, cylindrical, or spherical expansion, and $\xi_n \cong 1$ depending on the value of n and γ. [84] This model has been very successful at modelling YBCO plumes at pressures in the hundreds of mTorr, using the value of n=3 for a 3-D spherical shock, however the best value of n for modeling plume expansion is pressure dependent, with the value of n approaching the 3-D ideal at higher pressures, and dropping to n=0, (essentially a free expansion) at pressures at 25 mTorr. [68]

One deficiency of the blast wave model is that it predicts the plume will expand indefinitely. At higher pressures and propagation distances, a drag model may be

used to account for the eventual stopping of the plume. The drag model may be derived from a simple, first-order differential equation of motion:

$$\frac{dv}{dt} = -\beta v \tag{2.13}$$

where v is the velocity of the plume, t is the propagation time, and β is a linear drag coefficient. Separating variables and integrating yields:

$$v = c_1 exp(-\beta t) \tag{2.14}$$

where c_1 is the constant of integration. Rewriting the velocity term as v = dr/dt, and integrating over time results in:

$$r(t) = c_2 - \frac{c_1}{\beta} exp(-\beta t) \tag{2.15}$$

where c_2 is another constant of integration. Applying the boundary condition, r(t=0) = 0, results in the relation $c_2 = c_1/\beta$. This simplifies the above equation to:

$$r(t) = \frac{c_1}{\beta}(1 - exp(-\beta t)) \tag{2.16}$$

The other boundary condition comes from recognizing that r comes to a finite value in the limit t $\rightarrow \infty$. In this limit we recognize the maximum value of r, $r_{max} = c_1/\beta$. Now the drag model of the plume propagation can be written as:

$$r(t) = r_{max}(1 - exp(-\beta t)) \tag{2.17}$$

Work by Geohegan [36] and Phelps [68] has shown the drag model to be superior for modeling plume motion at higher pressures and propagation distances. Unlike the blast wave theory, it provides an estimate for the initial plume velocity. And while

blast wave theory in most cases is a better model of plume front motion, drag theory is superior at modeling motion of the position of peak intensity. [68]

Using the wavefront velocities derived from position vs time data, the gas temperature and pressure in the shocked region may be determined using relations derived from the conservation laws for mass and momentum as well as the ideal gas law: [58]

$$\rho_S = \rho_g \left(1 + 1/\gamma_S\right) \tag{2.18}$$

$$P_S = \frac{2\rho_g v^2}{1+\gamma_S} \tag{2.19}$$

$$T_S = \frac{P_S}{\rho_S}\frac{M_g}{R} \tag{2.20}$$

where ρ_S and ρ_g are respectively the mass density in the shocked and unshocked regions, γ_S is the ratio of specific heats for constant pressure and constant volume (~ 1.3), P_S and T_S are the pressure and temperature in the shocked region, R is the universal gas constant, and M_g is the molecular weight of the background gas. Using a shock front velocity of $v = 5 * 10^5$ cm/sec, a gas temperature of 1000 K, and an oxygen gas pressure of 150 mTorr results in a shock temperature of T = 4 eV and a shock pressure of 12.6 torr.

Combining the results from the limits of the free-expansion and the shock front enables construction of a temperature profile of the plume (see Figure 2.4). The characteristic features of this profile are a sharp rise from the background gas temperature to a peak value behind the shock front, followed by a decay to a lower temperature in the bulk of the plume.

If the shock front is assumed to be in LTE, the ionization fraction, α, can be determined from the Saha equation:

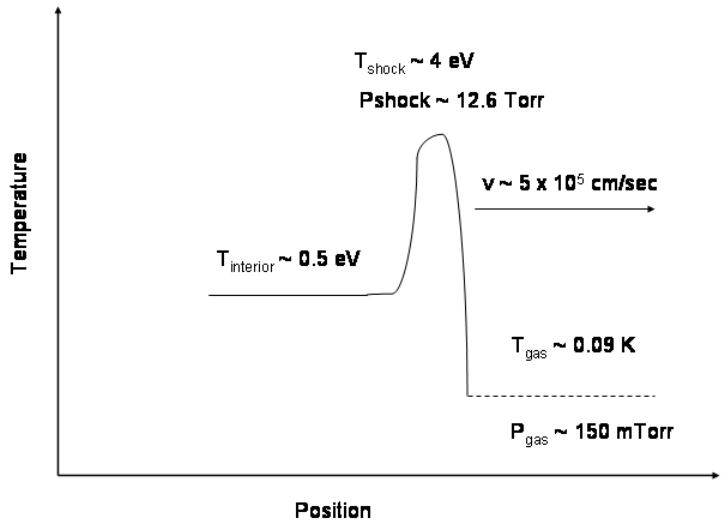

Figure 2.4: The temperature structure for the ablation plume consists of a shocked region at the contact front with the background gas and a bulk region. The temperature of the shocked region is estimated from the shock front velocity, [58] while the temperature of the bulk region is assumed to be similar to that for a free-expansion. [27]

$$\frac{\alpha^2}{1-\alpha} = \frac{2.4 * 10^{-4}}{p} T^{\frac{3}{2}} exp\left(-\frac{W_i}{kT}\right) \tag{2.21}$$

where T is the temperature in Kelvin, W_i is the ionization energy, and p is the pressure in torr. [61] At the shock front conditions given above, the right hand side of equation 2.21 is far greater than one–implying that the ionization fraction, α is very close to one. This result is due to the high temperatures ($\sim$ 4 eV) compared to the ionization energies ($\sim$ 5 - 10 eV), and the low pressures ($\sim$ 10 torr) in the shock front.

2.4 Pulsed Laser Deposition Diagnostics

The desire to characterize optimum deposition conditions for commercial production of YBCO has led to development of several plume diagnostic techniques. The importance of these *in situ* diagnostic techniques is underscored by the discovery that YBCO test samples grown at identical machine settings in different deposition events may have significantly different results for critical temperature and current. [83] Thus, establishing effective process control requires developing *in situ* diagnostics to monitor plume and surface deposition conditions associated with optimum crystal growth. Factors of interest include plume composition, especially as related to the stoichiometry of the deposited film (known to affect superconducting properties). In addition, plume energy, including the partitioning into kinetic, electronic, and ionization channels, is of interest as it relates to setting up ideal conditions at the deposition surface.

A variety of diagnostic techniques have been tried to monitor the evolution of laser ablated plumes, including optical and ion-probe time-of-flight measurements, as well as absorption and emission spectroscopy. Time-of-flight measurements provide information on the spatial and temporal evolution of the kinetic energy distributions, and if this measurement is performed using spectrally-filtered video, it may also yield insight on species' spatial distribution. Complementary to the time-of-flight measurements, absorption and emission spectroscopy enables identification of plume components and measurements of electronic state distributions and stoichiometry.

Time-of-flight measurements of YBCO plumes have been performed to measure plume front velocities as a function of time and distance to determine which of the plume propagation models (free expansion, blast wave, or drag) best explained plume behavior. [36] As mentioned in the previous section, plume front motion is almost always best modeled using a blast (or shock) wave model, except at high pressures and propagation distances where a drag model appears to work best. [68] In the blast wave regime, plumes move at very high Mach numbers (M in the range 10-50). [68] At negligible pressures and shorter distances, the plume motion is best modeled as the free expansion of a supersonic jet. [36] In the absence of drag, plume components are free to separate, with electrons streaming in front because of their low mass. And the ions, being pulled by the electrostatic attraction of the free electron stream, move slightly faster than the atoms. [27]

In addition to modeling plume front velocities, kinetic energy distributions derived from time-of-flight measurements have been fit to the modified Maxwell-Boltzmann distribution (see equation 2.9) to determine streaming speeds and kinetic temperatures. [26, 68, 92] These measurements typically resulted in values of u $\approx 10^5$ to 10^6 cm/sec, with corresponding kinetic energies on the order of tens of eV. This streaming kinetic energy is far in excess of typically reported electronic temperatures ($\sim$ 0.2 to 3 eV) derived from plume emission spectra, [28, 91] clearly indicating non-equilibrium between kinetic and electronic energies.

Emission spectroscopy has also been used as a diagnostic of plume evolution, initially to identify components of the plume, and also to measure the partitioning of energy into electronic excitation. Collected spectra has consistently identified yttrium and barium neutrals and ions, and copper neutrals. [10, 19, 27, 39, 88, 90, 91] However, there is disagreement with detection of copper ion emission, with some authors reporting ion emission is not present [27, 39, 91], while at least one group reported copper ion emission. [10]

Also of significant interest is the formation and detection of oxides in the plume. Emission measurements have reported a very strong YO molecular band, as well as weaker BaO and CuO bands. [27, 90, 91] The source of the oxide bands has been studied to resolve whether they originate at ablation or are formed in the plume. The YO band intensity appears to vary inversely with laser fluence. [74, 75] Plume stoichiometry has also been studied with the goal of determining whether deposited films are formed directly from ablated particles or from condensation of atoms and molecules on the deposition surface. There is disagreement in the literature with some authors asserting that oxides are a nascent ablation product, [39] while others suggest oxides are formed by a more complex mechanism by the reaction of Y + O_2 → YO* + O, with the subsequent YO* → YO explaining the strong YO emission band. [29, 34] The latter is most likely, as Chen notes, Y and O are not on the same plane in the YBCO crystal structure, so it is unlikely that YO is a nascent product of ablation. [19]

Spectral measurements have also provided information on the electronic state distributions for species in the plume. The population ratio, R_{pop} between two states, $|i\rangle$ and $|o\rangle$ can be determined from the measured fluence, Φ, of an emission line and the transition probability A for the corresponding transition. First, we define R_{pop} as:

$$R_{pop} = \frac{N_i/g_i}{N_o/g_o} \tag{2.22}$$

where N_i and N_o are the upper and ground state population levels, and g_i and g_o are the upper and lower state degeneracies. The population of the upper state N_i can be related to the emission fluence, Φ_{ij} from the upper state $|i\rangle$ to some lower state $|j\rangle$ by the relation

$$\Phi_{ij} = f_{rad} A_{ij} N_i \tag{2.23}$$

where A_{ij} is the transition probability, and f_{rad} is the ratio between the effective solid angle $d\Omega$ subtended by the sensor and the solid angle, 4 π steradians into which the light is emitted. This now yields the expression

$$R_{pop}(E_i) = \frac{\Phi_{ij}}{f_{rad} A_{ij} g_i (N_o/g_o)} = \frac{\Phi_{ij}/(A_{ij} g_i)}{\alpha} = f(E_i) \tag{2.24}$$

where $\alpha = f_{rad} N_o/g_o$, and E_i is the energy of the emitting state $|i\rangle$. The value of α may be empirically determined from the boundary condition that $R_{pop} = 1$ in the limit that $E_i = 0$. It is often observed that the population ratio drops dramatically with increasing energy, in this case a suitable choice of $f\left(E_i\right)$ would be $f\left(E_i\right) = exp\left(-\beta E_i\right)$. This, of course, is equivalent to modeling the population data with a Boltzmann distribution, where $\beta = 1/\mathrm{kT}$.

Various explanations have been offered for the apparent consistency of the Boltzmann distribution fit to observed electronic state distributions. One common approach is to assume the presence of local thermodynamic equilibrium (LTE) in the plume. LTE is a relaxation of the strict requirements of thermodynamic equilibrium (where the the kinetic energies are given by a Maxwellian distribution, the electronic states by a Boltzmann distribution, the photons by a Planckian distribution, the ionization ratio by the Saha equation, and the characteristic temperatures of all energy distributions must agree). [48] LTE relaxes the requirements for full thermodynamic equilibrium by removing the requirement for a Planckian photon distribution (thus assuming an optically-thin plasma as photons escape the plume before being absorbed and reradiated on the path to equilibrium). Excited state populations are assumed to be dominated by collisional excitation, with minimal effect from photon absorption. Because of this, the photon energy distribution is expected to be a result of the collisional excitation process, and not a Planckian distribution. [43, 66] The prevailing view in the literature is that electron collisions are responsible for electronic excitation, and the temperature extracted from a fit of a (typically sparse) measured electronic state distribution to the Boltzmann distribution is a useful estimate of the

electron (or plasma) temperature. [28, 91] A variety of results have been reported, ranging from 0.2 to 3 eV, yet a common theme is that different elements often have different temperatures, with copper having the highest temperature. [91]

The applicability of the LTE approximation to laser ablated plumes is not universally accepted. Some authors accept the LTE approximation without question, [27, 46] some use the LTE approximation with reservations, using the Boltzmann representation merely as a compact method of describing the electronic state distribution, [28, 91] while others flat out reject the validity of assuming LTE. [9]

Early papers in the literature on the topic of electronic state distributions tended to take simple approaches using sparse data sets, and presented limited detail. An example of this approach is seen in Dyer [27], which reported an electronic temperature for the plume based upon the intensity ratio of two yttrium ion lines in a narrow (350-400 nm) wavelength band. Dyer's paper sought to demonstrate that under low pressure conditions ($\sim 10^{-6}$ torr) that the velocity of the plume was consistent with the model for free-expansion of a gas into a vacuum (see equation 2.11). Dyer used this equation to calculate T using the terminal velocity, V of the plume, and obtained values ranging from 6400 - 13000 K (0.55 - 1.1 eV). In comparison, the electronic temperature derived from the pair of yttrium ion lines was approximately 6500 K, consistent with the free-expansion calculation. Dyer performed his line ratio calculation assuming the presence of LTE without ever stating why the assumption was valid.

A similar approach to Dyer was taken by Auciello [10], where spectra was collected over the 320 - 830 nm wavelength range. Thirty unambiguous emission lines were assigned to specific transitions. However, electronic temperature values (which were assumed to be equivalent to the plasma temperature), were determined from intensity ratios of only two emission lines instead of a fit to all available data, and yielded values in the range 7000-9000 K (0.60 - 0.78 eV). The species used to compute the temperature was not stated, suggesting an unspoken assumption that all species

were at a common temperature. Also notable is that Auciello reported the presence of a Cu ion emission line, which has not been reported elsewhere in the literature.

The method of electronic temperature measurements by line intensity ratios was extended by El-Astal, [28,29] who measured yttrium and copper neutral temperatures as a function of distance from the ablation target. At conditions of 180 mTorr O_2 background pressure and 4 J/cm^2 laser fluence, the copper temperature (determined from the 515.3 to 510.6 nm line ratio) was observed to decrease from 1.1 $\pm$ 0.2 eV at 0.5 μsec after ablation to $\sim$ 0.55 $\pm$ 0.1 eV at 10 μsec, at which point the temperature leveled off. At these same conditions, the yttrium temperature (determined from the 464.4 to 619.2 nm line ratio) decreased from 1.05 $\pm$ 0.2 eV at 1 μsec to $\sim$ 0.35 $\pm$ 0.15 eV at 10 μsec.

A similar effort to El-Astal's work was conducted by Al-Wazzan, [8] also at 180mTorr, but at lower laser fluence (2.6 J/cm^2). Studies of the electronic temperatures derived from Ba ion absorption line ratios yielded the important result that temperature decreased in time at a slower rate than that expected by adiabatic cooling, and at 1 μsec and 1 cm downstream from the ablation target, actually rose to a peak value before decreasing. This nonadiabatic behavior was attributed to redistribution of the forward directed velocities of fast ions in the leading edge into randomly directed motion inside the plume. [8]

The line-ratio approach was used by Apostol to measure plume temperatures near the ablation site. [9] Measurements were taken 200 nsec after ablation, and 1 mm above the target surface, yielding temperatures ranging from 0.6 to 1 eV. No information was offered regarding which lines were used for the temperature estimate, other than spectra were collected from 400 to 600 nm wavelength. Apostol asserts without supporting his argument that LTE is applicable at early plume evolution, but not applicable at later times, and temperatures cannot then be determined from emission lines in different ionization stages. [9]

Another line-ratio measurement was conducted by Harilal, who measured plume temperatures as a function of distance from target, time since ablation, and laser fluence. [45] Line ratio measurements were conducted using the 614 and 649.8 nm barium ion lines and the 577.7 and 553.5 nm barium neutral emission lines. This resulted in an estimation of initial electron temperatures (assuming LTE) of 2.35 eV–decaying to a constant value of 0.18 eV at distances greater than 5 mm from the ablation target. However, there are some issues with the technique used in this paper– the 553.5 nm line is the fundamental transition for the Ba neutral, and thus susceptible to self-absorption. In addition to the temperature measurements, Harilal measured the Stark broadening of the 553.5nm Ba emission line to determine electron density as a function of experimental conditions. Stark broadening is the dominant broadening mechanism under conditions of high charge density and low kinetic temperature. [44] A simplified, empirical expression for the Stark broadened linewidth is given by:

$$\Delta\lambda_{1/2} = 2 * 10^{-16} W n_e \tag{2.25}$$

where the linewidth, $\Delta\lambda_{1/2}$ is in angstroms, the number density, n_e is in cm^{-3}, and the electron impact parameter, W, is estimated as $1.6*10^{-2}$, based on extrapolation for data in the same group on the periodic table. [45] Using this technique, the initial electron density was estimated as 2.5 x 10^{17} cm^{-3}.

An early, yet detailed and extensive study of electronic emission was presented in an article by Ying. [91] In contrast to the simple two-line ratio estimate performed by Dyer, Ying conducted a detailed spectral analysis, identifying 299 emission lines (64 Ba neutral, 10 Ba ion, 150 Y neutral, 63 Y ion, 11 Cu neutral, and 1 O neutral) in the 388 - 900 nm wavelength region. Electronic temperatures were extracted from intensity data using a Boltzmann fit. However, despite collecting a wealth of data, the reporting of temperature results was minimal. Ying only reported Cu neutral temperatures at three locations, with values ranging from 8800 K (0.76 eV) near the ablation target, to 6300 K (0.54 eV) midstream, and 6800 K (0.59 eV) near the

deposition substrate. With respect to Ba and Y results, Ying reported Y temperatures as being "usually 1000 K lower than that of Cu and Ba", and the apparent temperature difference between the different elements was ascribed to "*...the approximate nature of LTE.*" [91]

With the exception of Ying's paper, [91] most of the published electronic temperature measurements have been obtained using line-ratio measurements. [8, 10, 27–29, 45] There is a risk to performing a calculation based on a ratio of two data points, in that a perturbation to one of the data points may skew the results more than if the calculation was performed by fitting a line through a greater number of data points. Several mechanisms may cause a significant error in a data point, resulting in a skewed result. These are self-absorption, temporal effects, and accuracy of the transition probabilities.

The first of these possible sources of error, self-absorption, occurs when a photon of light emitted as a result of a transition from state $|i\rangle$ to state $|j\rangle$ interacts with another atom in state $|j\rangle$. When this occurs, the photon may absorbed, exciting the atom to state $|i\rangle$. The atom can then reradiate the photon to any accessible lower state, and most likely in a different direction than its original path. The result is that the intensity of light detected at the wavelength for the i $\rightarrow$ j transition is decreased. If the absorption behaves linearly, that is the change in flux, ϕ per path length x, is linearly proportional to the flux:

$$\frac{d\phi}{dx} = -\beta x \tag{2.26}$$

where β is a proportionality constant. Integration yields the Beer-Lambert Law:

$$\phi = \phi_o exp(-N_j \sigma_{ji} x) \tag{2.27}$$

where β is the product of the number density of absorbers, N_j, and the absorption cross-section, σ_{ji}. [61,86] Because the typical lifetime of an excited state is on the order

of nanoseconds, for self-absorption to occur, the absorbing state $|j\rangle$ must either be the ground state or a metastable state. In prior work by Saengar, self-absorption was identified as the mechanism causing narrowing of the modified Maxwell-Boltzmann kinetic energy distribution obtained from time-of-flight data using the Cu 325nm emission line, which terminates on the Cu ground state. This distortion did not occur when monitoring the time-of-flight data where the emission originated on the same upper state, but terminated on an excited state. [73] With respect to self-absorption in barium, Riley used a laser-induced fluorescence measurement to measure strong self-absorption on the Ba 553nm fundamental line. [72]

In addition to self-absorption from transitions to the ground state, it is worth noting potential self-absorption for transitions to metastable states. Referring to Figure 2.5 the barium neutral has the ^{3}D metastable state at $\sim$ 1.1 eV. [60] This state is metastable because the transitions from here to the ground state violate both the orbital (Δ L = 0, $\pm$ 1) and spin (Δ S = 0) dipole selection rules (although heavier elements like barium may at times violate the Russell-Saunders selection rules). [13] There are many transitions in the visible band which terminate on this state, and the potential for self-absorption needs to be addressed when calculating electronic upper state populations using emission data. Yttrium is similar to barium in that it also has an energy state (^{4}F at $\sim$ 1.35 eV) on which many visible band transitions terminate (see Figure 2.6), which may be metastable because transition to the ground state would be forbidden by dipole selection rules.

Temporal effects also may affect estimated electronic state distributions, as plume emission measurements require a finite time to integrate the signal. During this time, it is possible for plume conditions (such as plasma temperature) to change dramatically such that a time-averaged measurement is not a useful representation of the conditions in a dynamically evolving plume. Mao illustrated this challenge by studying emissions from copper laser ablated plumes, noting that estimated Boltzmann temperatures were sensitive to integration times. [56] He determined that the maximum time a signal could be integrated without distortion as:

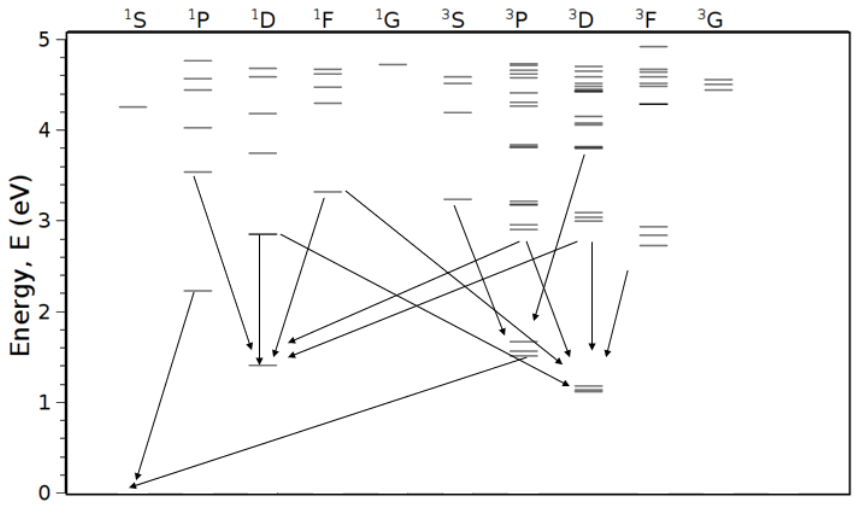

Figure 2.5: Ba I Grotrian Diagram. Arrows indicate observed transitions. The lowest group of ^3D states are known to be metastable, with lifetimes estimated on the order of minutes. [57] Note that a transition from ^3D to the ^1S ground state is forbidden by the electric dipole selection rules, Δ l $= 0, \pm 1$ and Δ s $= 0$.

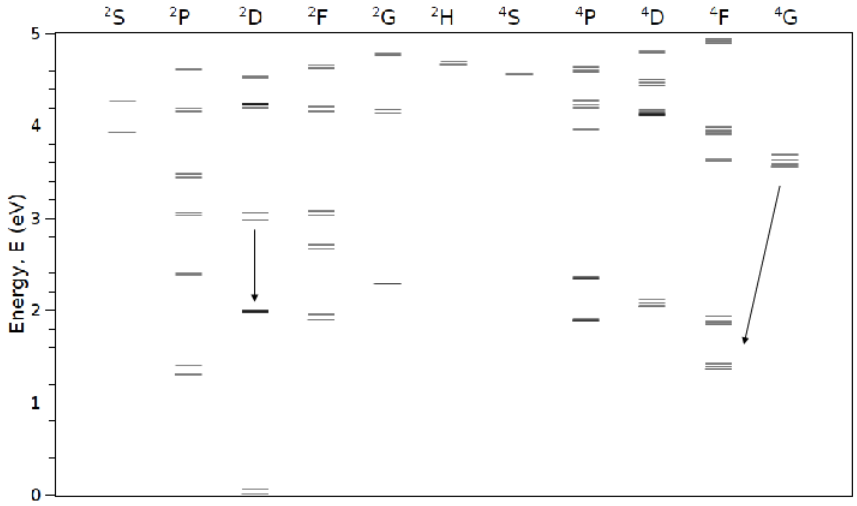

Figure 2.6: Y I Grotrian Diagram. Arrows indicate observed transitions. Note that a transition from the lowest ^4F state to the ^2D ground state is forbidden by the electric dipole spin-conservation selection rule, Δ s $= \pm\ 0$. This is similar to the case of the known Ba I ^3D metastable, suggesting the lowest ^4F state is metastable.

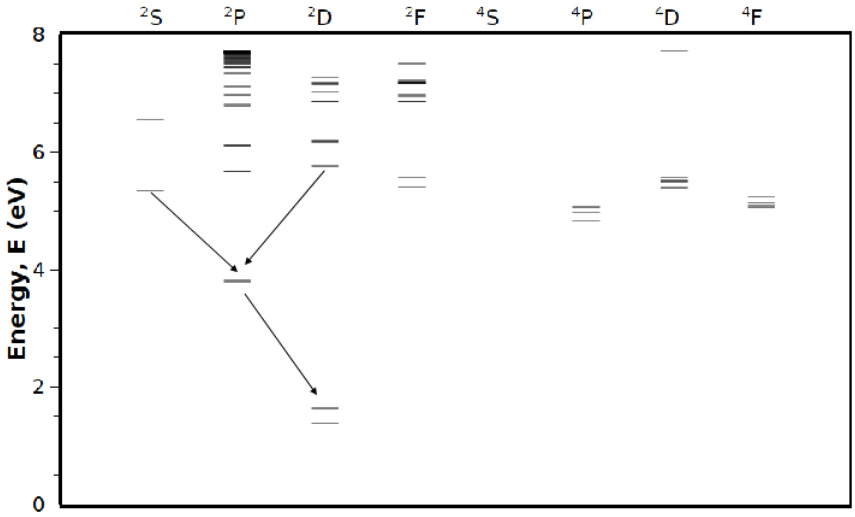

Figure 2.7: Cu I Grotrian Diagram. Arrows indicate observed transitions. Note that a transition from the lowest ^2D state to the ^2S ground state is forbidden by the electric dipole selection rule, Δ l = $\pm$ 1. This is similar to the case of the known Ba I ^3D metastable, suggesting the lowest ^2D state is metastable.

$$t_{int} = \frac{4x^{3/2}}{\xi^2(E_l/\rho_o)^{2/5}} \left(x - \frac{\xi^2(E_l/\rho_o)^{2/5}}{2v} \right)^{1/2} \tag{2.28}$$

where ξ is the coefficient from the Sedov-Taylor blast wave model discussed previously, E_l is the energy of the explosion that formed the plume, ρ_o is the the density of the background gas, and x is the propagation distance. [56] This result implies that the desired width of the detector integration gates is inversely related to the plume velocity. This paper influenced later analysis of PLD plumes, with subsequent work referencing this paper to explain their decision to either forgo calculating electronic temperatures [42] or account for potential transient effects on their results. [45]

The final source of error affecting prior measurements of electronic state distributions is the accuracy of atomic transition probabilities used in the calculations. These experiments predate a critical NIST review of the atomic transition probabilities for many Ba neutral and ion transitions which have taken into account more accurate measurements of Ba I and Ba II lifetimes and branching ratios. Because

both lifetime and branching ratios are involved, a large set of observed emission lines are affected, with values of the atomic transition probabilities changed as much as a factor of two. [51]

In retrospect, much work has been done to date to develop optical diagnostics for use in process control of YBCO PLD. However, the prior work in this field has been fragmented and isolated, addressing either time-of-flight or electronic state distributions, rather than developing an integrated interpretation of plume dynamics by synthesizing information available from both measurements. Narrow-band line emission time-of-flight measurements benefit from selection of an appropriate window that includes an emission line of interest and excludes interference lines. In return, time-of-flight measurements may yield information on kinetic energy and transient behavior that aid in interpreting electronic state distributions derived from emission spectroscopy. Finally, estimates of electronic state distributions are ripe for reexamination in light of awareness of temporal and self-absorption effects, as well as a revision of accepted values for atomic transition probabilities.

III. Experiment

This experiment consisted of collection of spectrally-resolved/time-integrated spectroscopy, and spectrally-filtered gated imagery of laser-ablated YBCO plumes. The data collection in this effort was performed by a team of researchers. The pulsed laser deposition apparatus was operated by personnel from the Air Force Research Laboratory's Materials Directorate, the imagery data was collected by a University of Dayton graduate student, while spectral data was collected by the author. The following sections will describe the apparatus and operation of the pulsed laser deposition system, the optical multichannel analyzer used for obtaining spectral data, and the camera used to collect imagery.

3.1 Pulsed Laser Deposition Apparatus

The key components of the pulsed laser deposition apparatus are the vacuum deposition chamber and the laser ablation source (see Figure 3.1). The deposition chamber has two stages on opposite ends: a rotatable stage for the bulk YBCO ablation target, and a heated stage for the deposition substrate. In addition, the deposition chamber had slotted viewports on either side of the chamber oriented perpendicular to the target-substrate axis. The 15 slots spatially restricted the lateral field-of-view to approximately 1 mm. Observations were made at these slots were for collecting plume spectra, as well as for monitoring plume time-of-flight. In addition to the slotted viewports, there was a large viewport at the top of the chamber, where a gated, intensified CCD-array fast framing camera was mounted. Finally, an additional optical port was mounted at an angle to the target-substrate axis for passing the ablation laser beam into the deposition chamber.

A Lambda-Physik LPX 305i KrF ($\lambda = 248$ nm) pulsed excimer laser incident on the target at 45 degrees was used to ablate the YBCO target. The laser was typically operated at a pulse repetition rate of 4-10 Hz with a pulse width (FWHM) of 17 ns. The laser spot size was estimated at 5.5 mm x 1.75 mm, and the delivered laser fluence varied between 4-10 J/cm^2 per pulse. Laser pulse energy was controlled by a

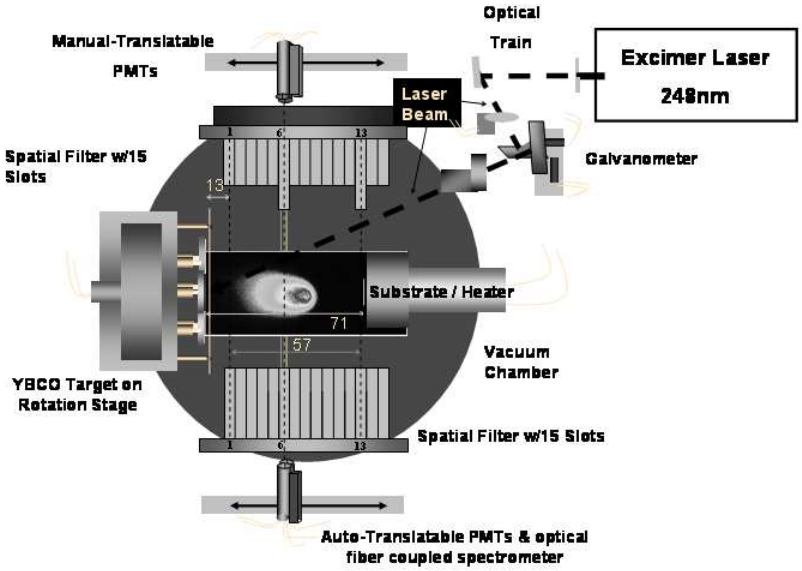

Figure 3.1: Pulsed laser deposition apparatus. All dimensions in mm. Figure courtesy of AFRL/MLPS and used with permission. [15]

fuzzy logic program to maintain a desired pulse time-of-arrival (ranging from 3.7 to 6.6 μsec, depending on oxygen background pressure) at a distance 35 mm downstream from the ablation target. The plume time-of-arrival was monitored with a spectrally filtered ($\lambda = 550 \pm 10$ nm) photomultiplier tube tuned to barium emission.

The ablation target for these measurements was a sintered pellet of $YBa_2Cu_3O_7$, alloyed with a 5% by weight concentration of Ag, which is added to improve mechanical properties of deposited films. [47] The ablation target was hand polished with sandpaper prior to each use and whenever chamber oxygen pressure was changed in order to minimize the effect of surface roughness on absorption of laser energy.

The PLD apparatus was software controlled using a LabView script written by AFRL personnel. This script controlled oxygen background pressure, substrate temperature, laser energy, ablation target rotation, slit position of the spectrometer fiberoptic, and the number of plumes that would be observed at each slit position. Oxygen pressure was selected and substrate temperature were set to a constant value

(760 °C) during each sample run. The feedback loop for controlling laser energy was driven by the signal of a spectrally-filtered ($\lambda = 550 \pm 10$ nm) PMT, monitoring a strong barium emission line, to keep the plume time-of-flight at a setpoint value at a fixed slot position. Although the Ba emission line at $\lambda = 553.54$ nm is known to be strongly self-absorbed, [72] this is not a concern as data from the PMT is only used keep the time-of-flight at a chosen setpoint. The ablation target was rotated between shots to minimize surface effects. The spectrometer optic was mounted on a software-controlled autotranslatable stage and set to look through viewing slits on the side of the PLD apparatus. A calibration was performed prior the experiment to determine what stage coordinates corresponded to desired slit viewing positions for the spectrometer optic. These positions were then included in the LabView script

3.2 Spectral Diagnostic

Emission spectra were collected by coupling a collection lens with an Oriel fused silica fiberoptic to an optical multichannel analyzer (OMA). The OMA apparatus consisted of an Acton SpectraPro model 275 spectrometer with a Princeton Instruments Pi-Max model 7361-0003 512 x 512 pixel focal plane array (FPA) intensified CCD camera mounted at the exit optic. The OMA was operated using Roper Scientific WinSpec/32 software provided with the camera. The spectrometer had selectable gratings, and this experiment used a grating blazed for maximum efficiency at 750 nm with a groove density of 1200/mm.

Significant care was taken to align and calibrate the spectrometer. Rotational alignment of the FPA to the entrance slit of the spectrometer was performed by monitoring the real-time signal from a spectral line from a calibration lamp, and rotating the camera until the lineshape was symmetric. This alignment enabled a significant increase in signal to noise, as all pixels in a column corresponded to light from approximately the same wavelength, allowing columns in the FPA to be summed. Additional signal-to-noise improvement was obtained by collecting only on those pixels which were illuminated by the entrance slit, eliminating detector noise contributed

by dark pixels. Wavelength calibration was performed by regression between known and observed positions of Cathodeon^{TM} Ne lamp spectral lines. The dispersion of the grating ranged from 0.054 nm/pixel at λ = 850nm to 0.066 nm/pixel at λ = 500nm. Spectral responsivity was measured using the two temperature blackbody technique, [87] and is described in Appendix A. This technique corrects for detector signal resulting from non-Planckian signal by computing the spectral responsivity as the ratio of differences of the detector signal and Planckian spectral distribution function at two different temperatures (here, T_1= 1250 K and T_2=1500 K). Non-Planckian terms, such as detector noise and ambient light, are assumed temperature independent and are cancelled out when differencing two signals taken at different temperatures. As is seen in Figure 3.2, the detector generates a signal response to spectral irradiance between 500 to 900 nm. The responsivity cutoff near 500 nm is consistent with the grating cutoff near 450 nm, [2] the responsivity cutoff at 900 nm is within the quantum efficiency cutoff for a Si detector at 1100 nm, [17] and the grating blaze wavelength at 750nm is in a region of high responsivity. Dark current measurements were taken immediately prior to each spectral measurement to minimize effect of detector drift. Spectrometer linewidth as a function of slit width was measured using a Ne (λ = 650.65 nm) standard lamp (see Appendix A). A constant slit width of 20 μm was used for measurements over the entire wavelength range.

The OMA was operated in a delayed gate mode, with the trigger provided by the laser. A delay of 0.5 μsec avoided collection of the intense transient signal from the ablation fireball, and gate widths (15 μsec at 150 mTorr and 35 μsec at 50 and 400 mTorr) were set to integrate the signal for the duration of the plume travel across the field of view of the collection slit. Gate delay and integration times were selected after observing trial runs with the imaging camera. Signal-to-noise of the collected spectra varied with oxygen pressure, slot distance, and wavelength (due to emission line strength, detector response, and molecular band interference), with the best conditions seen at 150 mTorr, slot 6 (36 mm), and λ = 650-800 nm. Using the

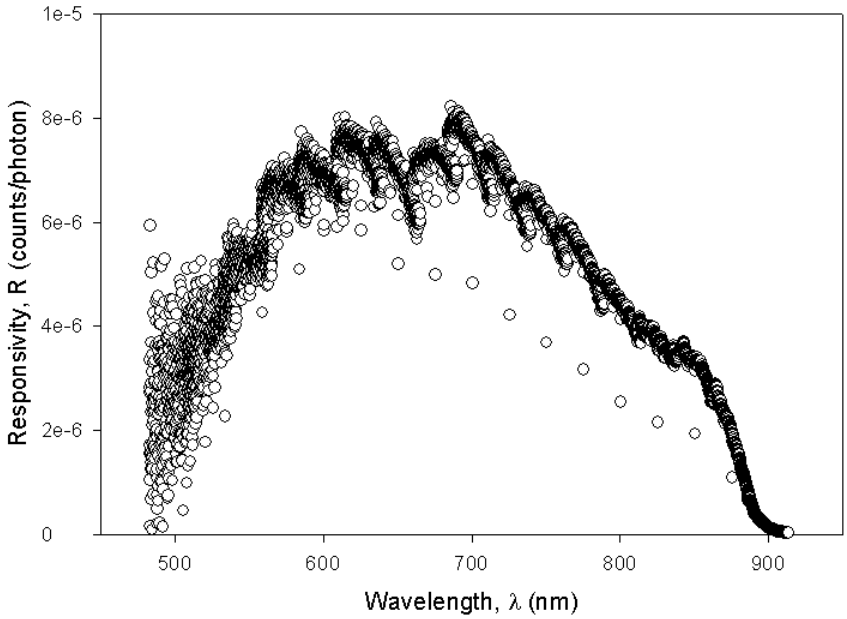

Figure 3.2: Relative spectral responsivity of optical multichannel analyzer. Responsivity of given data points indicate responsivity relative to one another, not in absolute terms.

$\lambda = 686.5687$ nm line, the signal-to-noise ratio (defined as the ratio of peak height to the standard deviation of the background) was estimated as 1.73.

The combination of grating dispersion and FPA size resulted in an OMA spectral bandpass of only 35 nm, far smaller than the 500-850 nm region of interest. This required collecting multiple, overlapping measurements of the region. Initial center wavelength was set at 500 nm, and proceeded at 25 nm intervals to the final center wavelength at 850 nm. Measurements always proceeded from shorter to longer wavelengths to ensure repeatable positioning by the grating stepper motor. At each bandpass, a background frame was collected by blocking the entrance slit, and a net spectrum was calculated by subtracting the background from the collected spectrum. The resulting net spectrum was output as an ASCII file for automated data reduction.

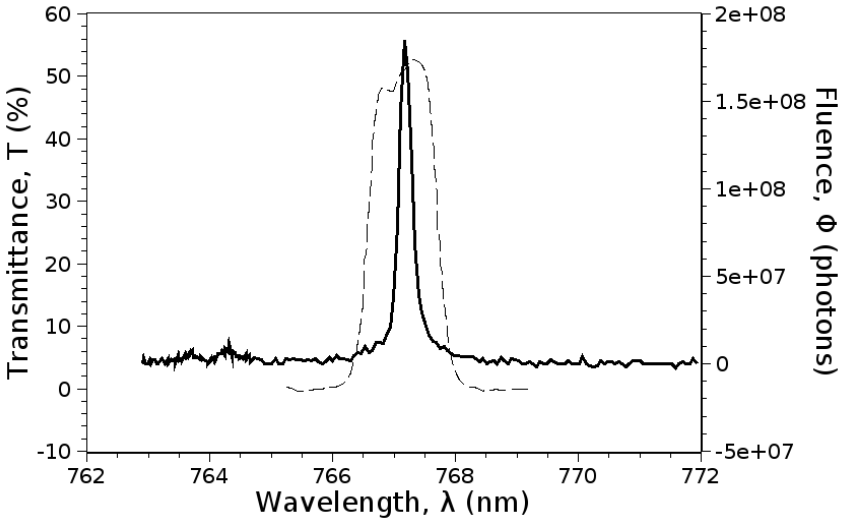

Figure 3.3: Transmittance of Barium filter. ($\cdots$ Transmittance, - Fluence)

3.3 Imagery Diagnostic

The imagery diagnostic has been previously described in the literature, [26] and the raw data that was obtained was previously reported by Phelps, [68] in the context of modeling plume shock behavior. The imagery instrument consisted of a Princeton Instruments Pi-Max model 7361-0003 intensified CCD camera with a 512 x 512 pixel focal plane array. The instrument was controlled using Roper Scientific WinView software. The camera was mounted at the top window of the vacuum chamber with the focus set at the expected plume path. After mounting, and prior to operation of PLD apparatus, the camera image was registered with a ruler to determine pixel dimensions in the field, yielding a pixel field dimension of 0.2 x 0.2 mm^2. Narrow-band spectral filters ($\Delta\lambda \sim 1$ nm) were used to isolate emissions of interest. These filters were mounted in a filter wheel placed in front of the camera lens. The two spectral filters used in this effort had band centers located at 767 nm and 809 nm. Figure 3.3 shows the transmittance band of the 767 nm filter, used to select and pass Ba neutral emissions, while the 809 nm filter in Figure 3.4 was used to pass only Cu neutral emissions. Both filters show excellent matching to the corresponding emission line.

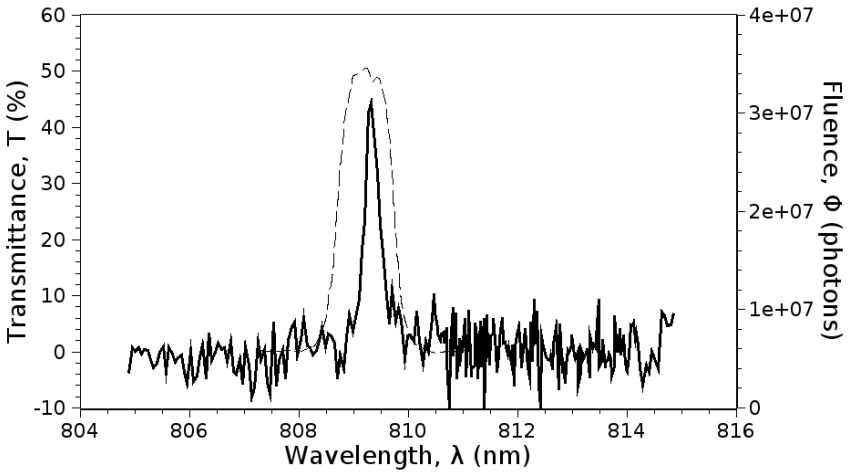

Figure 3.4: Transmittance of Copper filter. ($\cdots$ Transmittance, - Fluence)

The camera was operated in a triggered mode, with the trigger provided by the laser. Movies of the plume were created by collecting frames at variable delays, with the delay swept from 0 to 25 μsec at 0.1 μsec intervals. Each image frame was integrated for multiple shots (n $>$ 100) to improve signal to noise. Pulse-to-pulse variations in the plume were characterized, with intensity (flicker) varying by 20%, and plume center-of-mass (jitter) by up to 3 mm. [68]

Time-of-flight waveforms were constructed for each slot position, sampling pixels representative of light collected by the OMA. This differs from the work of Phelps, [68] who used waveforms based on a larger pixel sample. Phelps provided a customized Matlab^{TM} script for extracting pixel intensities as a function of time from the plume movies. [67] The pixel counts as a function of time were saved to an ASCII data file. The resulting waveforms were zero-baselined and normalized using Tablecurve. [4]

3.4 Experimental Conditions

Measurements were conducted at four oxygen pressures (50, 150, 400, and 1000 mTorr), with spectra collected at 5 slot positions (31.4, 36.0, 45.7, 55.0, and 64.7 mm). Spectra collected at pressure 1000 mTorr (all slot positions), and at position 64.7 mm (all pressures) were of poor quality, and not analyzed.

The run matrix was designed to minimize the effects of unanticipated process variation on results. Consider the situation where spectra are collected sequentially by distance from the target, and unknown to the observer, there was a corresponding change in a process variable (such as laser power, background pressure, or target roughness). In this situation, it would be difficult to isolate the effect of distance from target on the spectrally derived electronic temperature from the confounding effect of the background process variables. Instead, the order in which spectra were collected were randomized as much as practicable, to break the correlation between run conditions and unknown background variables. [59] The run matrix was blocked by pressure, with order of pressure blocks chosen at random, and the order of slots observed was randomized within each pressure block. The run matrix as executed is presented in Table 3.1.

Table 3.1: Experimental Conditions

Pressure (mTorr)	slot	distance from target (mm)
150	5	31.4
150	10	55.0
150	6	36.0
150	12	64.7
150	8	45.7
1000	5	31.4
1000	8	45.7
1000	10	55.0
400	6	36.0
400	12	64.7
400	10	55.0
400	5	31.4
400	8	45.7
50	12	64.7

Table 3.1: Experimental Conditions – Continued

Pressure (mTorr)	slot	distance from target (mm)
50	5	31.4
50	10	55.0
50	8	45.7
50	6	36.0

IV. Results and Discussion

4.1 Results

4.1.1 Plume Imagery. Spectrally-filtered imagery was collected to characterize the kinetic energy of the laser ablated plumes. Imagery data collected for this experiment has previously been reported by Phelps, [68] with a focus on characterizing the shock characteristics of the evolving plume. The same experimental results are revisited here to provide context for the analysis of electronic state distributions in the plume.

Spectrally-filtered imagery was collected for laser ablated plumes under the conditions specified in Chapter III. Narrowband filters of 1 nm width centered at 767 nm (for Ba I) and 809 nm (for Cu I) were used to isolate emission for a single emission. A sample still frame of a Ba I filtered image is shown in Figure 4.1 Time-of-flight curves were derived by monitoring pixel intensity as a function of time. In addition, velocities of the plume wavefronts, shock strength, and shock kinetic temperatures were derived from the plume imagery. The results of these measurements will now be presented.

Time-of-flight curves at each slot position were obtained by monitoring the intensity of a row of five pixels at the intersection with the propagation path of the plume center. Sample TOF curves for Ba I and Cu I are given in Figure 4.2. The TOF curves were normalized such that areas under the curves were equal to one:

$$\int_0^\tau \phi(t)dt = 1 \tag{4.1}$$

where $\phi(t)$ is the detector signal at time t, while τ is the duration of the time-of-flight curve. This integration was performed numerically using Tablecurve software. The normalization was performed so that the time-of-flight curve could be used as a weighting function, and this will be used later in the section on temporal effects on electronic state distributions.

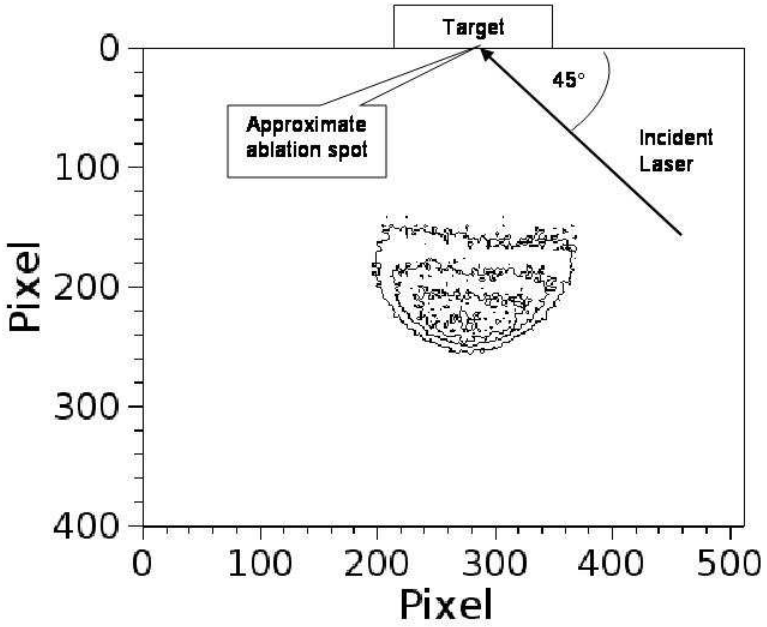

Figure 4.1: Contour plot of Ba I emission intensity from spectrally-filtered ($\lambda = 767 \pm 1$ nm) plume image. Frame taken at 7.3 μsecs at 150 mTorr O_2.

Modified Maxwell-Boltzmann velocity distributions (see equation 2.9) were fit to the time-of-flight curves using a user-defined function in Tablecurve. A sample plot of a fit of the modified Maxwell-Boltzmann distribution (n=4) to a time-of-flight curve is presented in Figure 4.3. Here, results are shown for a time-of-flight curve recorded at 150 mTorr O_2 and 36 mm downstream of the ablation target. The modified Maxwell-Boltzmann distribution provides a reasonable fit at the leading and trailing edges but does not adequately fit the peak of the distribution. Fit parameters for time-of-flight curves recorded at 50 and 150 mTorr O_2 are presented in Table 4.1. The quality of the fit at 400 mTorr O_2 was poor, as well as for Ba at 150 mTorr/55.0 cm, thus no results are presented for these conditions.

Table 4.1: Modified Maxwell-Boltzmann Fit Parameters

P (mTorr)	x (mm)	u_{Ba} (10^5 cm/s)	kT_{Ba} (eV)	u_{Cu} (10^5 cm/s)	kT_{Cu} (eV)
50	31.4	0.666 ± 0.522	53.1 ± 2.8	4.85 ± 0.118	16.6 ± 0.3
50	36.0	2.16 ± 0.234	40.9 ± 1.2	6.30 ± 0.110	11.2 ± 0.3

Table 4.1: Modified Maxwell-Boltzmann Fit Parameters – Continued

P (mTorr)	x (mm)	u_{Ba} (10^5 cm/s)	kT_{Ba} (eV)	u_{Cu} (10^5 cm/s)	kT_{Cu} (eV)
50	45.7	3.82 ± 0.095	24.8 ± 0.4	4.50 ± 0.077	10.3 ± 0.2
50	55.0	3.71 ± 0.062	19.8 ± 0.3	4.71 ± 0.083	8.0 ± 0.2
150	31.4	4.48 ± 0.226	24.2 ± 1.1	6.87 ± 0.123	7.2 ± 0.3
150	36.0	4.55 ± 0.153	18.2 ± 0.7	7.05 ± 0.086	4.5 ± 0.2
150	45.7	4.99 ± 0.061	6.9 ± 0.2	6.18 ± 0.0421	2.0 ± 0.07
150	55.0	***	***	5.27 ± 0.028	0.88 ± 0.04

The time-of-flight curves can also be expressed in velocity coordinates. A sample plot for the case of 150 mTorr and 36 mm from the target is given in Figure 4.4. This plot uses the same intensity values as the normalized time-of-flight plot in Figure 4.2, but the abscissa is expressed in velocity instead of elapsed time. Examination of this plot reveals that the copper velocity distribution is elevated compared to Ba at and forward of the point of maximum intensity. The forward bias of the copper velocity distribution compared to barium is likely a mass effect. Prior to plume formation in the Knudsen Layer, ejecta motion occurs as a free expansion with velocities varying as $M^{-1/2}$, where M is the mass of the ejected particle. [27] So it would be expected that the distribution of lighter materials in the plume would be preferentially weighted towards the leading edge compared to heavier materials.

The position of the wavefront as a function of time was also determined. The wavefront position was defined as the position along the leading edge of the plume where the intensity reached 50% of the maximum intensity of the plume. A sample plot of wavefront position is shown in Figure 4.5. The data in this plot was fit to the Sedov-Taylor model:

$$x(t) = x_o + \xi \left(\frac{E_o}{\rho_b} \right)^{1/5} t^{2/5} = x_o + at^{0.4} \tag{4.2}$$

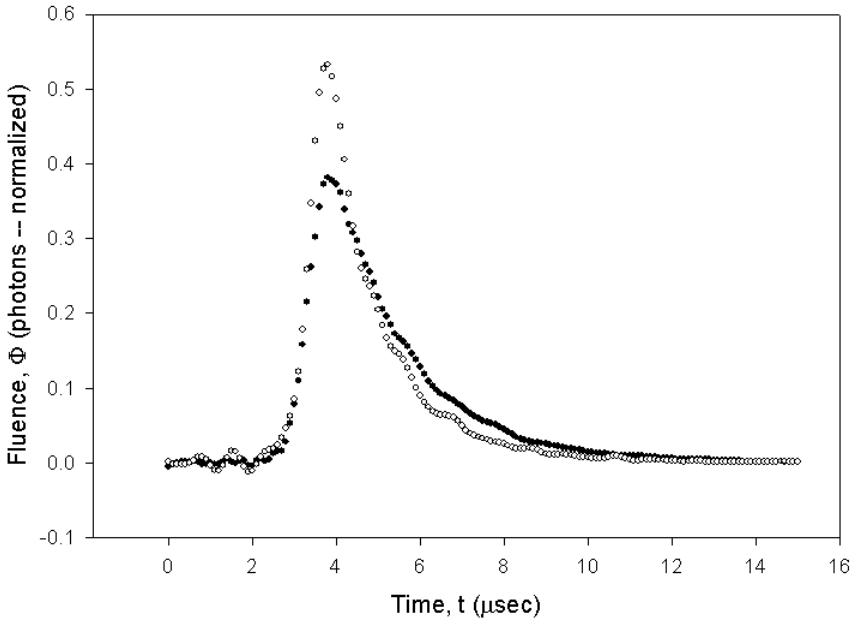

Figure 4.2: Sample normalized time-of-flight flux curves for Ba (•) and Cu (○) neutral emission. Ba I was collected with a narrowband spectral filter centered at 767 nm, while Cu I was collected with a similar filter at 809 nm. Cu peak flux is more narrowly peaked than Ba. Data collected at 150 mTorr and 36.00 mm downstream of target. Flux curves are normalized such that the area under the curve is equal to one.

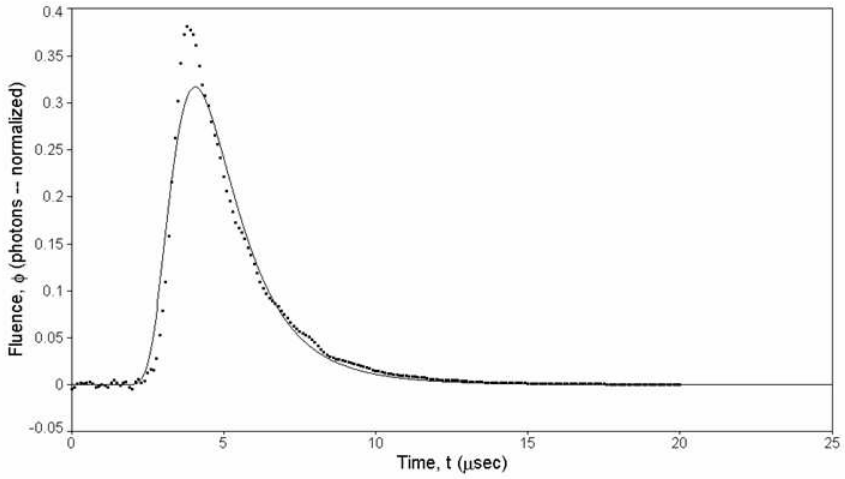

Figure 4.3: A modified Maxwell-Boltzmann velocity distribution (–) is fit to the barium (λ = 767 nm) time-of-flight curve (•) obtained at 150 mTorr pressure O_2 and 36 mm distance from ablation target. The model provides a good fit at the leading and trailing edge, but does not adequately model the peak in the distribution.

where the variables are as defined as in Equation 2.12 with the slight modification of adding an initial position x_o as a fitting parameter. The fitting parameters derived from fitting wavefront position and elapsed time data to the Sedov-Taylor model are presented in Table 4.2.

Table 4.2: Sedov-Taylor Fit Parameters

P (mTorr)	Ba x_o (mm)	Ba a $\frac{mm}{(\mu s)^{2/5}}$	Cu x_o (mm)	Cu a $\frac{mm}{(\mu s)^{2/5}}$
50	-19.0 ± 1.9	37.3 ± 1.8	-17.8 ± 2.8	36.4 ± 2.6
150	-6.7 ± 2.1	25.9 ± 1.8	-7.7 ± 2.2	26.5 ± 1.9
400	-2.2 ± 2.2	20.8 ± 1.9	-4.4 ± 2.6	21.8 ± 2.3

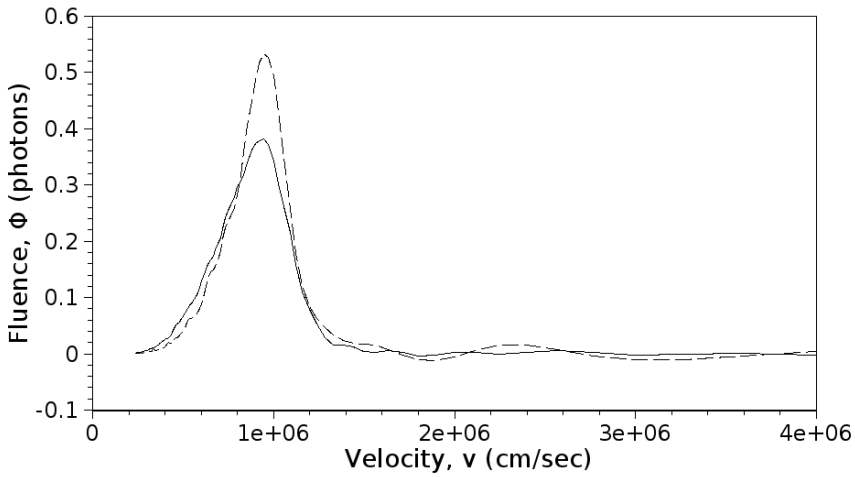

Figure 4.4: Fluence vs velocity curves for Ba (–) and Cu (--) neutral emission. Ba was collected with a narrowband spectral filter centered at 767 nm, while Cu was collected with a similar filter at 809 nm. By inspection, it appears the average and peak Cu velocities are slightly greater than for Ba. Data collected at 150 mTorr and 36.00 mm downstream of target. Flux curves have the same ordinate values as for Figure 4.2, except with abscissa values expressed in velocity instead of time.

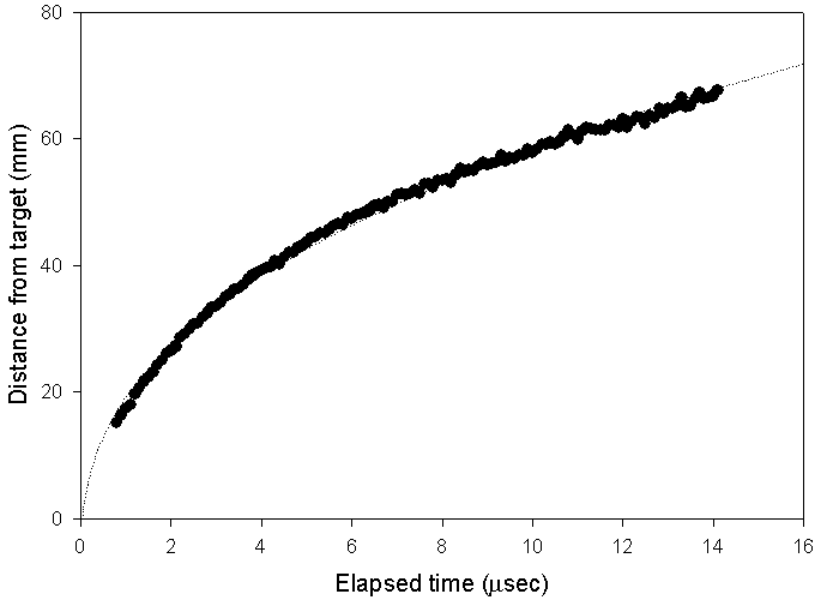

Figure 4.5: Ba wavefront position vs time at 150 mTorr O_2. When fit to the Sedov-Taylor blast wave equation, energy of initial explosion is ~ 0.87 J, consistent with laser pulse energy ~ 0.9 J.

The energy released, E_o, in the ablation was estimated from the Sedov-Taylor parametric fits. This energy may be calculated from the relation:

$$E_o = \xi a^5 \rho \tag{4.3}$$

where the Sedov-Taylor parameter, ξ, is assumed to be ~ 1. [84]

Calculating the mass density, ρ, of the background gas posed a challenge, as the background gas temperature was not measured during the experiment. However, the temperature of the substrate is known (T=760 Celsius) and provides an upper limit of the gas temperature. Using this value to calculate ρ and then E_o would provide a lower limit for E_o. At a gas pressure of 150 mTorr, this results in $\rho \sim 74.5$ ng/cm^3. Using the value of a = 25.9 mm/μs$^{2/5}$ from Table 4.2 results in $E_0 = 0.87$ J, consistent with the laser pulse energy of ~ 0.9 J previously reported for this experiment. [68]

The next plume characteristic determined from imagery data is the shock strength. The shock strength, S, is a measure of the steepness of the shock front, and is defined as the reciprocal of the shock width, where the shock width is defined as the distance between two points on the leading edge where the intensity is at 75% and 25% of the maximum value:

$$S = \frac{1}{x_{25} - x_{75}} \tag{4.4}$$

Here x_{25} and x_{75} are respectively the positions where photon flux is 25% and 75% of maximum value. The calculated values of shock velocity and shock strength are shown in Table 4.3. The shock velocity decreases with distance and pressure, while shock strength increases with pressure when distance is held constant.

Finally, wavefront velocities derived from the position vs time data were used to estimate the plume shock temperatures using Equations 2.18 - 2.20. The background gas density was calculated assuming a temperature of 760°C. The results of the calculations are presented in Table 4.4.

Table 4.3: Time-of-flight Metrics

P (mTorr) / d (mm)	Ba S (mm^{-1})	Cu S (mm^{-1})
50 / 31.4	0.30	0.28
50 / 36.0	0.31	0.23
50 / 45.7	0.22	0.20
50 / 55.0	0.15	0.13
150 / 31.4	0.46	0.57
150 / 36.0	0.44	0.51
150 / 45.7	0.51	0.58
150 / 55.0	0.46	0.54
400 / 31.4	1.27	1.40
400 / 36.0	1.27	1.70
400 / 45.7	1.02	1.27

Table 4.4: Shock Temperatures Calculated from Wavefront Speed

P (mTorr) / d (mm)	Ba T_{shock} (eV)	Cu Shock T_{shock} (eV)
50 / 31.4	14.5	13.7
50 / 36.0	11.3	10.6
50 / 45.7	7.1	6.8
50 / 55.0	4.7	4.3
150 / 31.4	5.4	5.7
150 / 36.0	4.1	4.1
150 / 45.7	2.3	2.3
150 / 55.0	1.3	1.4
400 / 31.4	2.6	2.8
400 / 36.0	1.9	2.1
400 / 45.7	1.0	1.1

4.1.2 Spectra. Emission spectra were collected for YBCO laser ablated plumes at multiple oxygen background pressures and distances from the ablation target. The spectra covered the region λ = 480-960 nm with the coverage limited by the spectral responsivity of the optical multichannel analyzer. The spectra were assembled from 14 overlapping bandpasses of 34 nm width, with the bandpass center wavelengths spaced at 25 nm intervals from 500 to 850 nm. As seen in Figure 4.6, the spectra are rich in atomic emission lines, and feature a prominent YO (A $\rightarrow$ X) molecular emission band centered near 613 nm.

The YO A $\rightarrow$ X transition band (see Figure 4.7 has previously been studied at high resolution by Weiner. [89] The cluster of lines from 597 - 612 nm originate from the A $^2\Pi_{\frac{3}{2}}$ upper states, while the cluster of lines from 612 - 630 nm originate from the A $^2\Pi_{\frac{3}{2}}$ upper states. Mixed in with the molecular spectra are atomic and ionic electronic emission lines, including the Ba neutral ^{3}P $\rightarrow$ ^{3}D manifold lines at 590.86, 597.37, 599.83, 602.11, 606.45, and 611.11 nm, and the Ba ion line at 614.18 nm.

The line assignment process commenced with comparison of the plume spectra with reference spectra from standard lamps. Of the 87 emission lines measured, 44 were correlated with an element of origin in this fashion. Specific transitions were identified by examination of electronic energy diagrams, proceeding up the ladder of states, and accounting for all allowed transitions to lower states. An example of how this was done is given in Figure 4.8. All dipole-allowed transitions in the 5d6p ^{3}F$^\circ$ $\rightarrow$ 6s5d ^{3}D manifold are shown on the right side of the figure. Examination of the measured spectra accounts for all but the missing ^{3}F$^\circ_2$ $\rightarrow$ ^{3}D$_3$ line expected at 801.826 nm. The absence of this line is consistent with the absence of a measured atomic transition probability for this transition. [3, 51] This method is repeated at progressively increasing energy levels until no emission lines are found that correspond with dipole allowed transitions.

A total of 66 lines were assigned to specific atomic transitions. In addition, what appeared at first look to be 10 unassigned atomic emission lines were later determined

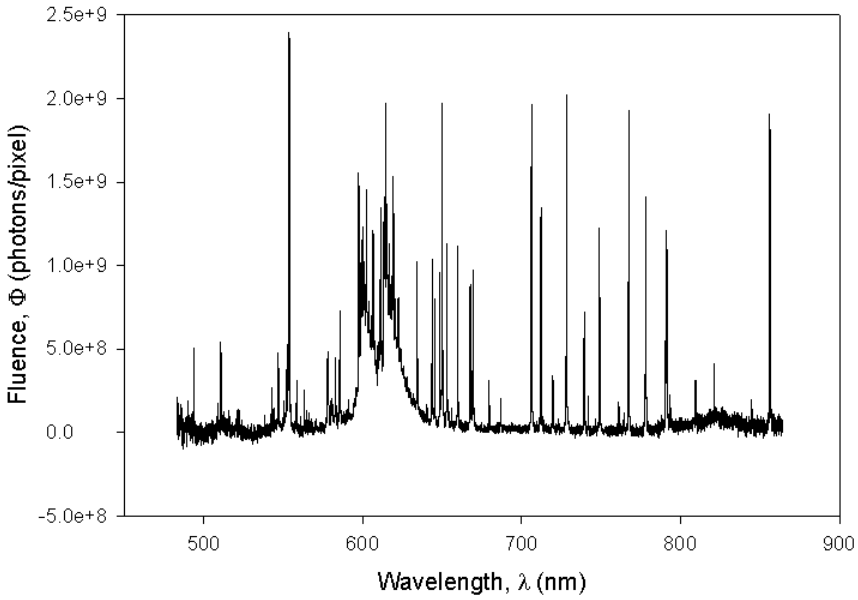

Figure 4.6: YBCO emission spectra (recorded at d=36.0 mm and 150 mTorr O_2 background pressure) is rich in Y, Ba, and Cu electronic lines. The strong molecular emission band centered near 613 nm is the YO A $\rightarrow$ X transition.

by comparison to Weiner's high resolution spectra [89] to be YO A$\rightarrow$X bandheads. A list of assigned lines by species is presented in Table 4.5, and a complete listing of line assignments is given in Appendix C. Eleven lines remain unassigned, 2 of which were in the complicated YO emission region, and the remaining nine lines were ambiguous. Eight of the nine ambiguous lines are possibly Ba or Y atom or ion emissions, however, there is either no measured transition coefficient (in which case no further population analysis can be conducted), or there are multiple transitions that could be responsible for the emission line. The ambiguous nine lines were also compared to Ag (used in the YBCO ablation target to improve mechanical properties in the deposited material), and to Hg (present in industrial lighting), but no match was found. A histogram of linecenter residuals is given in Figure 4.11. The residuals appear normally distributed and well within the instrument linewidth.

Emission line fluences were obtained using a two step process: first, by subtracting the background signal, and next, by fitting Gaussian lineshapes to the observed

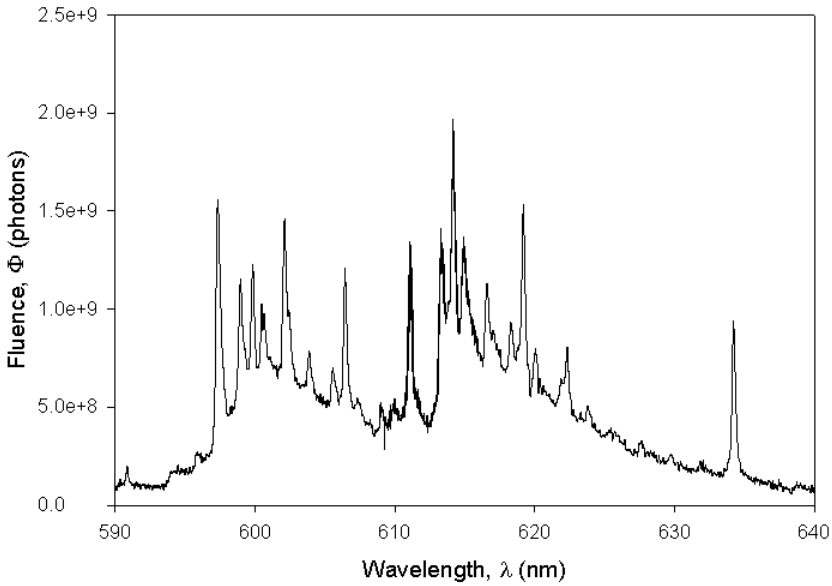

Figure 4.7: YO A $\rightarrow$ X emission band in YBCO emission spectra recorded at d=36.0 mm and 150 mTorr O_2 background pressure. The cluster of lines from 597 - 612 nm originate from the A $^2\Pi_{\frac{3}{2}}$ manifold, while the cluster of lines from 612 - 630 nm originate from the A $^2\Pi_{\frac{3}{2}}$ manifold. The presence of overlapping atomic electronic emission lines, including the Ba neutral ^{3}P - ^{3}D manifold, complicates interpretation of the spectra.

Table 4.5: Emission Line Assignment Summary

Species	Frequency
Y I	14
Y II	3
Ba I	36
Ba II	4
Cu I	8
Cu II	0
O I	1
YO bandhead	10
Unassigned	11
Total	87

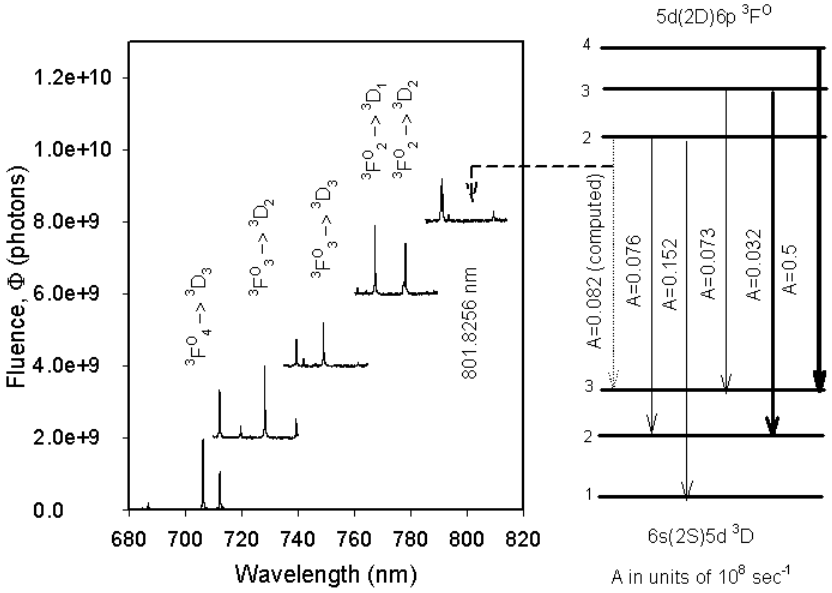

Figure 4.8: PLD emission spectra from five consecutive overlapping bandpasses are compared to energy level diagrams as part of the line assignment process. Spectra for each bandpass are vertically separated by adding a constant baseline to ease visual interpretation. All dipole-allowed transitions between the $^3F^\circ \rightarrow {}^3D$ manifold are accounted for before proceeding to higher energy manifolds. The one missing transition at 801.8 nm does not have an experimentally measured A_{ij} coefficient, thus one would not expect to see this line.

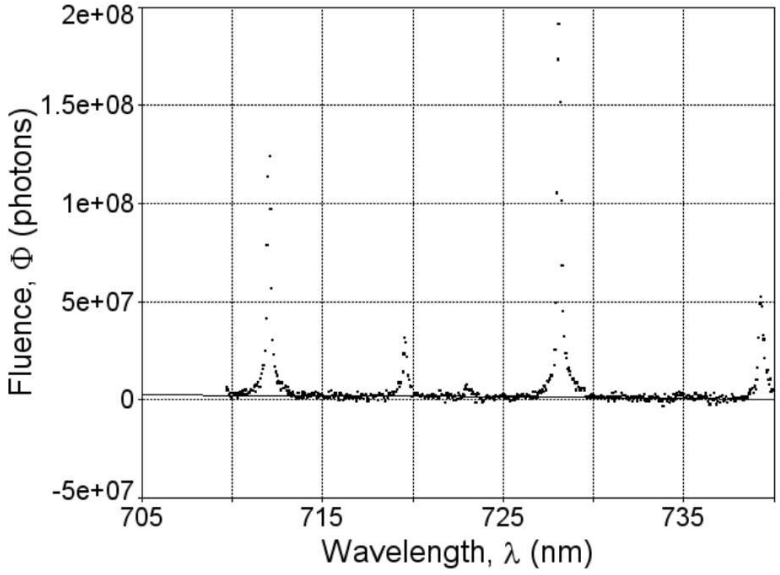

Figure 4.9: PLD emission spectra background was subtracted using Peakfit^{TM}software by fitting a linear or polynomial function to manually selected points in the baseline and subtracting the value of the function from each point in the spectra. This would result in spectra with a flat, zeroed baseline.

spectra. Background signal was subtracted in Peakfit^{TM} [5] by fitting a linear or polynomial function to manually selected points in the data (see Figure 4.9), and subtracting the function value from the y-axis value of the data. Gaussian lineshapes were also fit to the emission peaks using Peakfit^{TM}. Because the lineshapes are instrument broadened (see Appendix A), the linewidth parameter was fit as a common parameter for all emission lines, with values typically between 0.125 - 0.130 nm. The lineshape area was used as the metric of emission fluence. Tables of emission fluences for each condition are presented in Appendix D.

Because the spectrometer has a spectral bandwidth of $\sim$ 34 nm, yet collection windows are spaced 25 nm apart, there is a $\sim$ 5 nm region of overlap for neighboring bandpasses. Measuring line fluences in this region provides an indication of the variability of the source. As a baseline for comparison, consider the measured line fluences for a Cathodeon^{TM}barium lamp shown in Figure 4.12. With the exception of

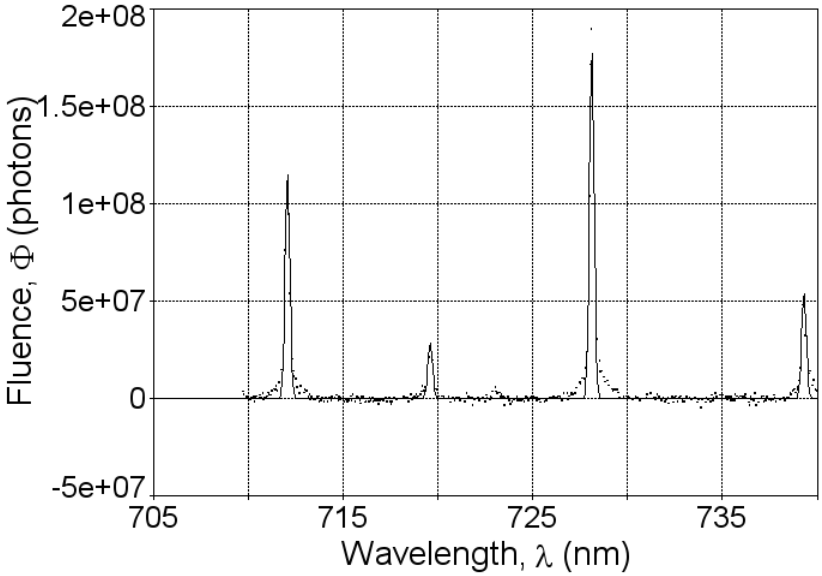

Figure 4.10: PLD emission line fluence was determined by fitting Gaussian lineshapes to the PLD emission spectra. Emission lines are instrument broadened.

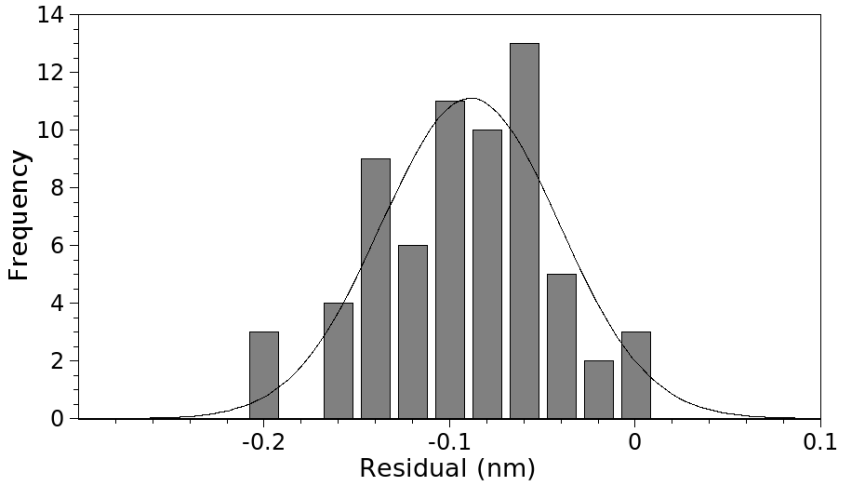

Figure 4.11: Residuals of emission linecenters vs values of assigned line positions compare favorably to a Gaussian distribution on a histogram. Deviations from the mean are well within the 0.3 nm instrument linewidth. Measured linecenters appear to be shifted by 0.1 nm from the reference values.

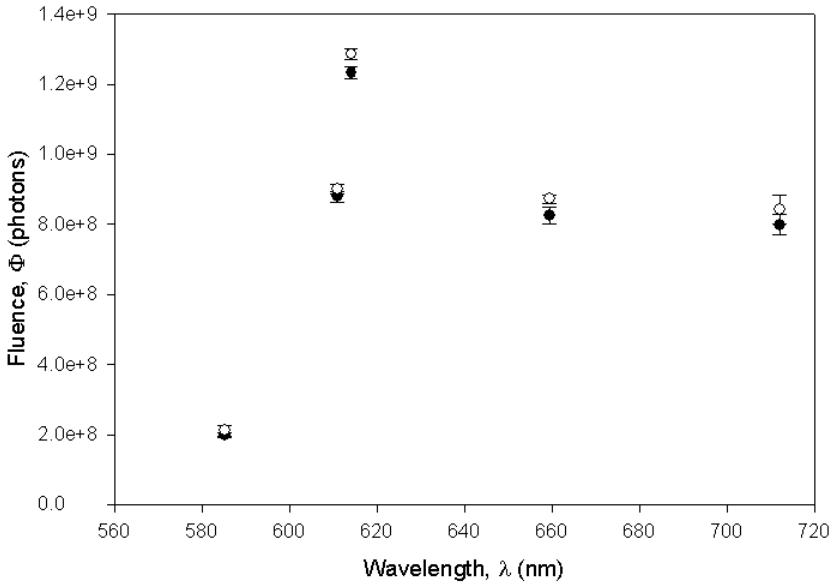

Figure 4.12: Comparison of Cathodeon^{TM} Ba lamp emission line fluences in overlapping segments of collection bands (•-low wavelength band ∘-high wavelength band). Except for one emission line (614 nm), emission fluences in overlapping bands agree within experimental limits.

one line at 614 nm, the fluences of emission lines observed in overlapping bandpasses agree within experimental error. This indicates the band-to-band calibration of the spectrometer is good. Next, the fluences for the same emission lines in the PLD spectra are shown in Figure 4.13. The results here are different: with the exception of the 659 nm line, the fluences of emission lines in overlapping bandpasses differ greater than experimental error. Since instrument variability has been measured and found to lie within experimental error, the variability seen in the PLD emission line fluences can be attributed to the variability of the plume.

Ba neutral emission line fluences were corrected for self-absorption using the Beer-Lambert absorption law to determine a correction factor. The Beer-Lambert law relates the incident and transmitted fluence by:

$$\Phi_{ij} = \Phi_{ijo} exp\left(-N_j \sigma_{ji} x\right) \tag{4.5}$$

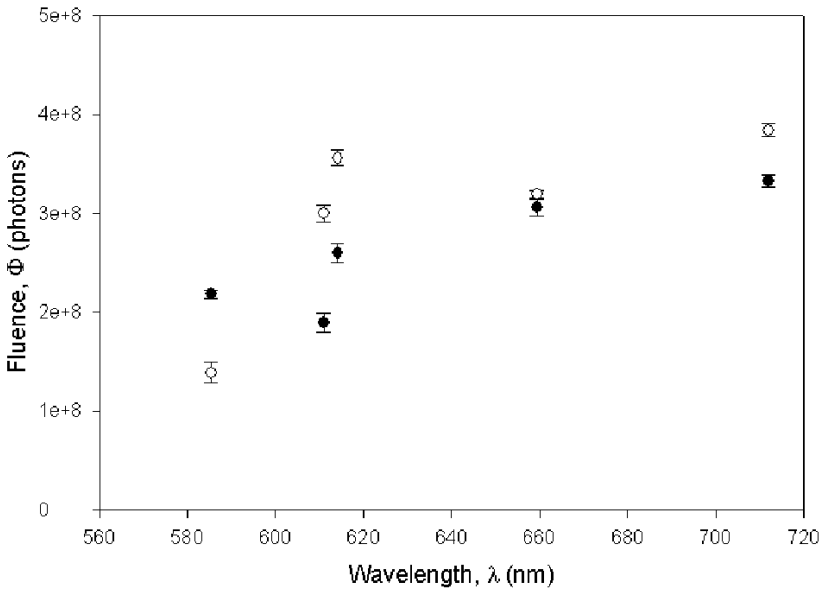

Figure 4.13: Comparison of YBCO PLD emission line fluences (at 150 mTorr, 36.0 mm downstream of ablation target) in overlapping segments of collection bands (•-low wavelength band ○-high wavelength band). Unlike lamp spectra, PLD spectra show significant differences for some emission lines in overlapping collection bands.

where Φ_{ij} and Φ_{ijo} are respectively the transmitted and incident fluence, N_j is the number density of the absorbers, σ_{ji} is the absorption cross-section for the j $\rightarrow$ i transition, and x is the absorption path length.

The incident fluence Φ_{ijo} is unknown, however, it can be expressed in terms of the emitter number density, N_i, by $\Phi_{ijo} = f_{rad}\ A_{ij}\ N_i$, where f_{rad} is a radiometric factor equal to the effective solid angle subtended by the detector, $d\Omega$, divided by 4π steradians. Then equation 4.5 may be rewritten as:

$$\frac{\Phi_{ij}}{f_{rad}A_{ij}N_i} = exp\left(-N_j\sigma_{ji}x\right) \tag{4.6}$$

of which the natural logarithm is:

$$Ln\left(\frac{\Phi_{ij}}{f_{rad}A_{ij}N_i}\right) = -N_j\sigma_{ji}x \tag{4.7}$$

The absorption cross section can be related to the transition probability, A_{ij}, and wavelength, λ, by:

$$\sigma_{ji} = A_{ij}\frac{\lambda^2}{8\pi n}\frac{g_i}{g_j}g(\nu) \tag{4.8}$$

where the index of refraction, n = 1, and $g(\nu)$ is the lineshape.

To apply this relation to a series of transitions originating from a common manifold and terminating on the metastable ^{3}D levels, some simplification is necessary. For the metastable ^{3}D levels, the spread between the highest and lowest energy state is $\sim$ 0.06 eV. This is small (about 6%) in comparison to the energy of the state ($\sim$ 1.15 eV). Thus it may be reasonable to assume the populations, N_j for the ^{3}D states are approximately equal. Likewise, a similar argument could be made for the upper state N_i populations. In addition, the assumption will be made that the radiometric constant, f_{rad}, the absorption path length, x, and the lineshape, $g(\nu)$are common for all wavelengths. Then equation 4.7 can be expressed as:

$$Ln\left(\frac{\Phi_{ij}}{\Phi_{ijo}}\right) = Ln\left(\frac{\Phi_{ij}}{aA_{ij}}\right) = -\left(\frac{N_j x}{8\pi} g(\nu)\right)\left(A_{ij}\lambda_{ij}^2 \frac{g_i}{g_j}\right) \tag{4.9}$$

where the parameter a = $f_{rad}N_i$.

The self-absorption correction factor, $\frac{N_j x}{8\pi} g(\nu)$, was determined from the slope of a plot of Ln(Φ_{ij}/(a A_{ij})) on the y-axis, and ($A_{ij}\lambda_{ij}^2 \frac{g_i}{g_j}$) on the x-axis. The value of the parameter a is determined by noting that there is no self absorption if the self-absorption cross-section is equal to zero. This provides the the boundary condition $\Phi_{ij} = \Phi_{ijo}$ in the limit $(A_{ij}\lambda_{ij}^2 \frac{g_i}{g_j}) = 0$. A sample Beer's Law plot is show in Figure 4.14. The correction factors for the ^{3}F°→^{3}D manifold were used to correct all transitions terminating on the ^{3}D state (including the ^{3}D°→^{3}D and ^{3}P°→^{3}D manifolds), as these plots had the best R^2 correlation coefficients. Fluences were corrected for each individual line by inverting the Beer-Lambert law, using the $\frac{N_j x}{8\pi}$ derived from the fit in the exponential term. Attenuation was significant for transitions to the ^{3}D states, with maximum attenuation values rising as high as 80%. Tables of self-absorption correction factors and corrected fluences for Barium neutral emission lines are presented in Appendix D. Yttrium also has a low energy (^{4}F) metastable state which may contribute to self-absorption. However, corrections were not attempted for yttrium because the dataset was too sparse to perform a Beer-Lambert correction.

With the emission line fluences corrected for self-absorption, excited state populations can now be calculated. The excited state populations will be represented by their ratio to the ground state. This ratio, R_{pop}, was previously defined in equation 2.22 as:

$$R_{pop} = \frac{N_i/g_i}{N_o/g_o} \tag{4.10}$$

where N_i and N_o are respectively the upper and lower state populations, and g_i and g_o are respectively the upper and lower state degeneracies. The upper state populations

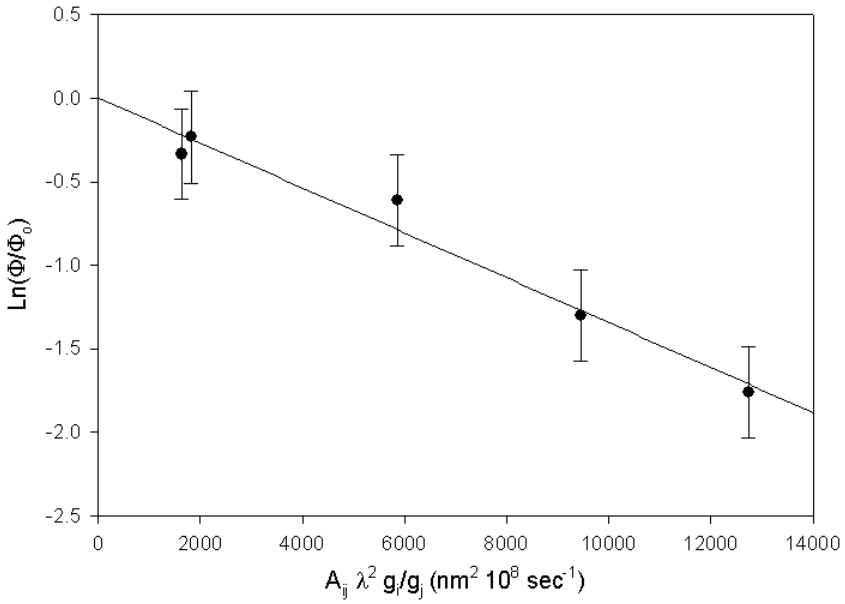

Figure 4.14: Observed intensities for Ba neutral electronic transitions terminating on the metastable 6s5d ^{3}D state are consistent with the Beer-Lambert absorption law. The slope of the fit for the 5d6p ^{3}F° $\rightarrow$ 6s5d ^{3}D manifold was used to compute fluence corrections for self-absorption.

are estimated from the spectral fluences by the relation $\Phi_{ij} = \frac{d\Omega}{4\pi} A_{ij} N_i$. Now the state population ratio can be expressed as:

$$R_{pop} = \frac{\Phi_{ij}}{A_{ij} g_i} \frac{4\pi}{d\Omega} \frac{g_o}{N_o} = \frac{\Phi_{ij}/(A_{ij} g_i)}{\alpha} \tag{4.11}$$

where $\alpha = (N_o/g_o)/(\mathrm{d}\Omega/4\pi)$. The unknown parameter, α, can be determined by invoking a boundary condition, requiring that $R_{pop} = 1$ in the limit where the upper state energy approaches zero. This is done by plotting the values of $\mathrm{Ln}(\Phi_{ij}/(A_{ij} g_i))$ as a function of upper state energy, fitting the data to a model (such as the Boltzmann LTE model), and assigning the value of the y-intercept to $\mathrm{Ln}(\alpha)$.

This technique may be further refined to indicate changes in the plume stoichiometry relative to the stoichiometry of the bulk material. Instead of separately determining the values of α for Y, Ba, and Cu by invoking the boundary condition of $R_{pop} = 1$ in the limit of upper state energy going to zero, only the value of α for Y is determined with this technique, while the values of α for Ba and Cu are determined as a function of α for Y, the stoichiometric ratios, and the ground state degeneracy ratios.

The first step is to recall the definition of α

$$\alpha = \frac{4\pi}{d\Omega} \frac{N_o}{g_o} \tag{4.12}$$

In bulk $YBa_2Cu_3O_{7-x}$, the stoichiometric ratio for Ba to Y is 2:1, while for Cu to Y, it is 3:1. So we can write $(N_o)_{Ba} = 2(N_o)_Y$ and $(N_o)_{Cu} = 3(N_o)_Y$. The degeneracy ratios are determined from the ground state terms for Y, Ba, and Cu. The ground state term for Y is ${}^2D_{\frac{3}{2}}$ [65] which corresponds to a degeneracy of $(g_o)_Y = 2(\frac{3}{2})+1 = 4$. Likewise, the ground state term for Ba is ${}^1S_0$ which results in a degeneracy of $(g_o)_{Ba} = 2(0) + 1 = 1 = \frac{1}{4}(g_o)_Y$. Finally, the ground state term for Cu, ${}^2S_{\frac{1}{2}}$, corresponds to a degeneracy of $(g_o)_{Cu} = 2(\frac{1}{2}) + 1 = 2 = \frac{1}{2}(g_o)_Y$.

Now calculating the value of α for Ba relative to Y results in:

$$(\alpha)_{Ba} = \frac{4\pi}{d\Omega}\frac{4 * 2(N_o)_Y}{(g_o)_Y} = 8(\alpha)_Y \tag{4.13}$$

while the value of α for Cu relative to Y is:

$$(\alpha)_{Cu} = \frac{4\pi}{d\Omega}\frac{2 * 3(N_o)_Y}{(g_o)_Y} = 6(\alpha)_Y \tag{4.14}$$

With the values of α for Ba and Cu determined relative to the α for Y, a composite semilog plot of population ratio, R_{pop}, versus upper state energy, E_i can be prepared. A sample plot is presented in Figure 4.15, derived from data collected 36 mm downstream from the ablation target at 150 mTorr oxygen pressure. There are two key pieces of information that can be derived from this plot. First, when $Ln(R_{pop})$ is plotted against E_i, and the data are in a linear distribution, the result is consistent with the Boltzmann population distribution. The Boltzmann population distribution is given by:

$$\frac{N_i}{N_o} = \frac{g_i}{g_o} exp\left(-\frac{E_i}{kT}\right) \tag{4.15}$$

where N_i and N_o are the upper and lower population levels, g_i and g_o are the upper and lower state degeneracies, and kT is the temperature. Rearranging terms results in:

$$R_{pop} = \frac{N_i/g_i}{N_o/g_o} = exp\left(-\frac{E_i}{kT}\right) \tag{4.16}$$

And taking the natural log of this equation yields:

$$Ln\left(R_{pop}\right) = -\frac{E_i}{kT} \tag{4.17}$$

So the slope m, of a linear distribution of points on a semilog plot of population versus upper state energy can be interpreted as the negative reciprocal of the temperature

of the population distribution, or kT = - 1/m. The error for the temperature, σ_{kT} is then given using standard error analysis formulas, [14] as:

$$\sigma_{kT} = \frac{\sigma_m}{m} \tag{4.18}$$

where σ_m is the error for the slope. For the data plotted in Figure 4.15 the distributions appear to be linear for each species, however, the slopes correspond to different electronic temperatures for Y (0.36 ± 0.02 eV), Ba (0.31 ± 0.02 eV), and Cu (0.44 ± 0.03 eV). It is also worth noting emission for Ba and Y are extinguished near 3.5 eV, while emission still occurs for Cu at much higher values of E_i. For example, a dipole allowed transition for Ba at E_i = 4.1 eV is not observed (λ = 752.8 nm), yet Cu transitions are observed as high as E_i = 5.8 eV. This result implies that in the laser-ablated plume, the electronic excitation process is somehow much more efficient for Cu than for Y and Ba.

The electronic state distributions and calculated electronic temperatures are presented in Appendix E. A panel plot of the results is shown in Figure 4.16, which shows electronic temperatures are relatively insensitive to pressure and position, and differ significantly mostly by type of emitter. Examination of the plot clearly shows that copper has a higher temperature than yttrium and barium. However, the difference between yttrium and barium in most cases appears to be within error bars. Even so, when error bars are neglected, estimated yttrium temperatures tend to be higher than barium.

The second feature to be analyzed in the population versus energy plot are deviations from nascent stoichiometry. Prior work in the literature has noted the presence of metal-oxide molecules in the plume. [27, 90, 91] The formation of the metal-oxide molecules by a reaction of metal atoms ablated from the bulk target with the oxygen gas may perturb the stoichiometric ratio of Y:Ba:Cu if the metal atoms combine with oxygen at different reaction rates. Since the above definitions of α for Ba and Cu include the ground state populations, N_o, which were defined as the product

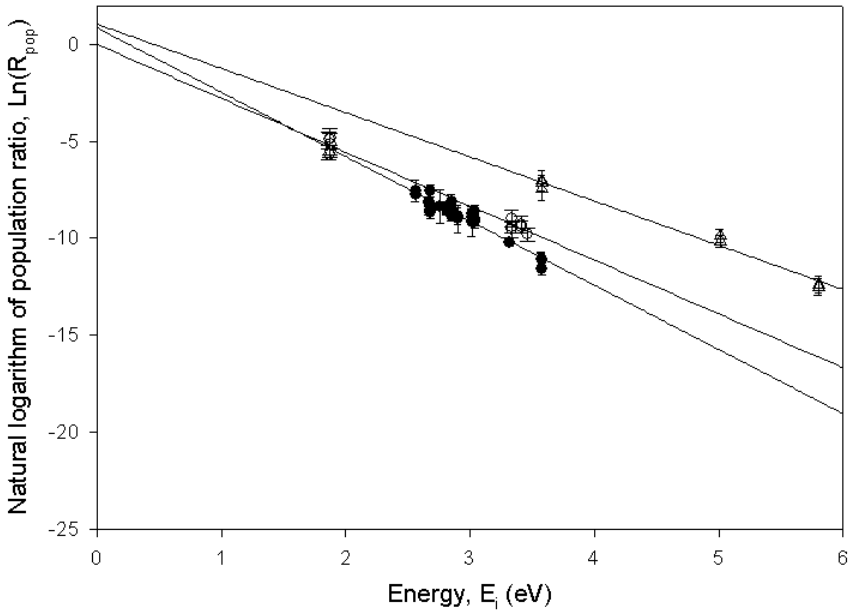

Figure 4.15: Time-integrated electronic state distributions, normalized for initial stoichiometric ratios, for yttrium, barium, and copper neutrals at 150 mTorr O_2, 36 mm downstream from ablation target. The slopes correspond to different electronic temperatures for Y (0.36 $\pm$ 0.02 eV), Ba (0.31 $\pm$ 0.02 eV), and Cu (0.44 $\pm$ 0.04 eV). In addition, Cu emission is occurring at much higher values of E_i than for Y and Ba. E.g., a dipole allowed transition for Ba at E_i = 4.1 eV is not observed (λ = 752.8 nm), but Cu transitions are observed as high as E_i = 5.8 eV. ($\circ$ Y I, $\bullet$ Ba I, $\triangle$ Cu I)

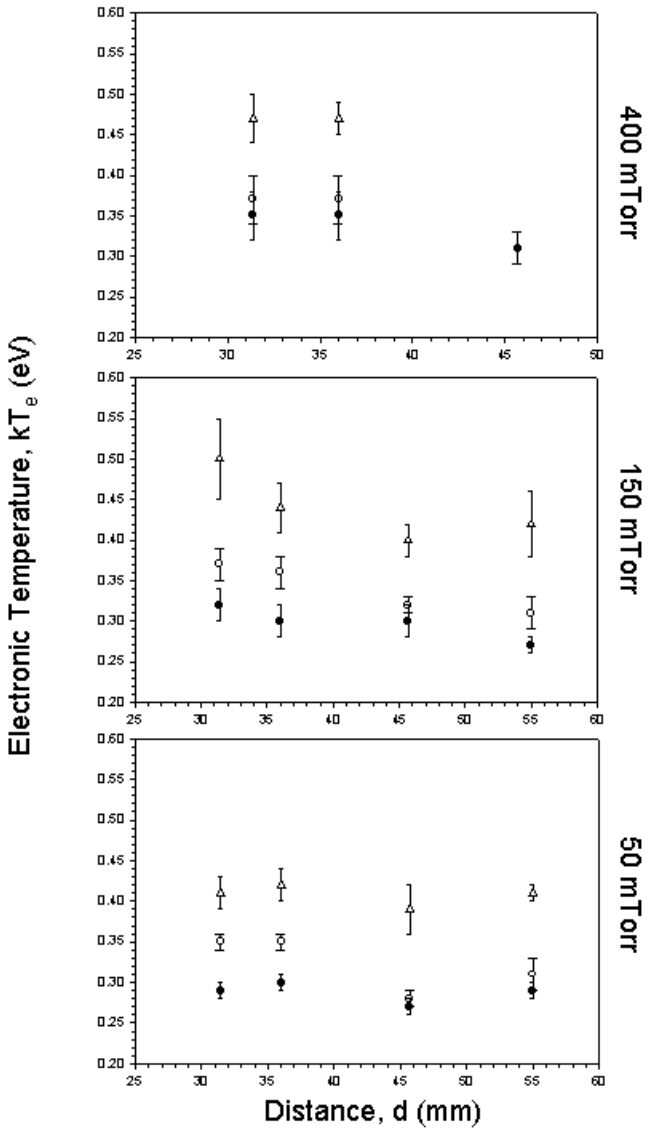

Figure 4.16: Electronic temperatures for Y, Ba, and Cu at multiple pressures and positions. Temperatures are relatively insensitive to position and temperature, and differ mostly by type of emitter. ($\circ$ Y I, $\bullet$ Ba I, $\triangle$ Cu I)

of the Y ground state population and the bulk stoichiometric ratio, deviations from the stoichiometric ratio will be seen as a shift away from zero on the vertical axis of the semilog population plot. Yttrium, as the baseline, will keep an y-intercept of zero (within rounding error). A positive intercept for barium or copper indicates yttrium is depleted relative to the initial stoichiometric ratio for that species. Likewise, a negative intercept for barium or copper indicates that species is depleted relative to yttrium.

The y-intercepts of the population plots are shown in Figure 4.17 and tabulated in Table E.35. In general, the error bars are comparable in value to the magnitude of the y-intercepts, making it questionable to draw inferences regarding changes in plume stoichiometry.

Finally, line-ratios are used to estimate the ionization fraction, $\alpha = N^i/N = N^i/(N^i + N^o)$ for the plume, where the total number density, N is the sum of N^i, the number density of ions in the ground state, and N^o the number density of neutrals in the ground state. First, the value of N^i/N^o is then determined from the Boltzmann population distribution (LTE is assumed), and given as:

$$\frac{N^i}{N^o} = \frac{\Phi^*}{\Phi}\frac{A}{A^*}\frac{\left(\frac{g_i}{g_o}\right)}{\left(\frac{g^i}{g^o}\right)^*}e^{-(E_i - E_i^*)/kT} \tag{4.19}$$

where quantities designated by the asterisk denote quantities associated with the ionized state, Φ is the line intensity, g_i and g_o are upper and lower state degeneracies, A is the transition probability, E_i is the upper state energy for the transition, and kT is the electronic temperature. Estimates were performed using the Ba I $\lambda = 728$ nm line and the Ba II $\lambda = 649.69$ nm line, and the Ba I electronic temperature.

With the ratio N^i/N^o determined, the ionization fraction α is determined from:

$$\alpha = \frac{N^i}{N} = \frac{N^i}{N^i + N^o} = \frac{1}{1 + \left(\frac{N^i}{N^o}\right)^{-1}} \tag{4.20}$$

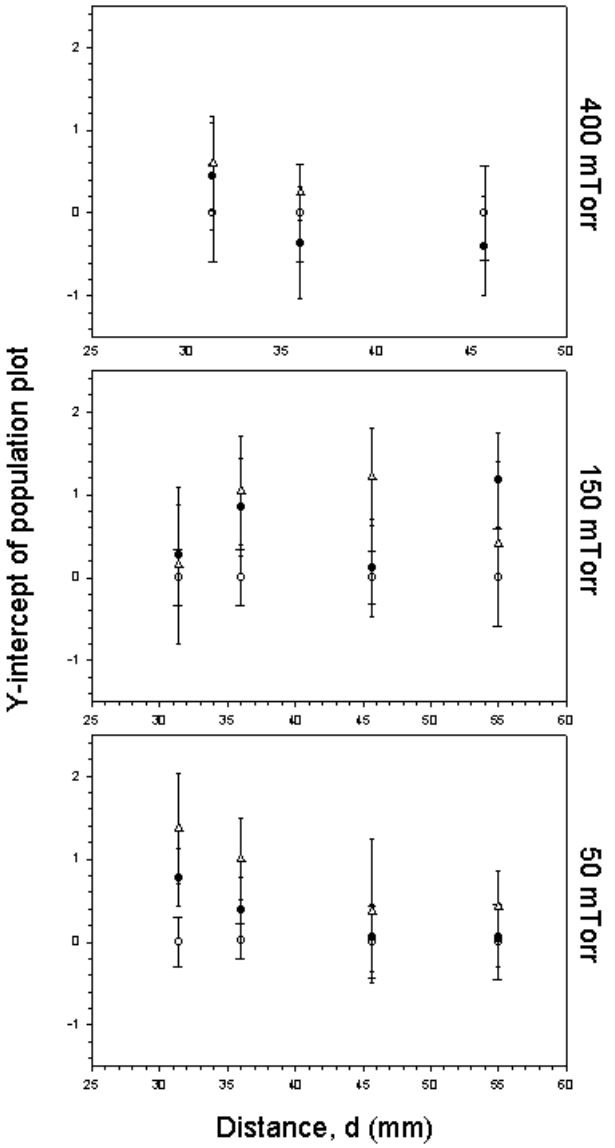

Figure 4.17: Y-intercepts for population plots for Y, Ba, and Cu at multiple pressure and slot positions. Intercepts have relatively large error bars. (○ Y I, • Ba I, △ Cu I)

with the results presented in Table 4.6. These results, in the range $\alpha = 0.25$ to 0.45 are very high. These results should be interpreted carefully as they result from a spectra integrated over the duration of the plume's passage in front of the sensor. As discussed in the background chapter, the ionization fraction approaches one in the shocked region, while in the bulk of the plume, the gas temperature is expected to be lower, so the value of α should be lower in this region. The estimates given here result from signal averaging over both the shock and bulk regions of the plume. In addition, this calculation assumed a common temperature for both the ion and neutral transition, which may be incorrect. This assumption was driven by a lack of sufficient data to compute the Ba II electronic temperature. Significant errors in the estimate of α may have resulted from inaccurate estimates of the ground state populations for both ions and neutrals, since their values depend strongly on the electronic temperature. The values presented here in Table 4.6 may be significantly inaccurate if ion and neutral temperatures are not equal.

Table 4.6: Shock Front Ionization Ratios from Emission Line Ratios

Background Pressure (mTorr)	Distance from target (mm)	Ionization Ratio (α)
50	31.4	0.38
50	36.0	0.32
50	45.7	0.33
50	55.0	0.32
150	31.4	0.32
150	36.0	0.28
150	45.7	0.29
150	55.0	0.25
400	31.4	0.38
400	36.0	0.42
400	45.7	0.35

4.2 Discussion

4.2.1 Preliminary calculations. As was mentioned in the background section, emission spectroscopy has been used to determine electronic state distributions as a diagnostic of plume electron temperatures, where the linkage between electronic state distributions and electron temperatures is the mechanism of electron-impact excitation under the condition of LTE. [40]

For collisional (electron- and atom/molecule-impact) and radiative excitation and losses, the steady-state master equation for populating excited state $|i\rangle$ from the ground state $|o\rangle$ may be written as:

$$\begin{aligned}\frac{dn_i}{dt} = 0 = \quad & n_o n_e \langle \sigma_{eex} v_e \rangle - n_1 n_e \langle \sigma_{edex} v_e \rangle \\ & + n_o n_a \langle \sigma_{aex} v_a \rangle - n_i n_a \langle \sigma_{adex} v_a \rangle \\ & - A_{io} n_i\end{aligned}$$

where n_o and n_i are respectively the lower and upper state population densities, n_e and n_a are the number densities of the electron and atomic collision partners, σ_{eex} and σ_{edex} are the electron impact excitation and deexcitation cross-sections, σ_{aex} and σ_{adex} are the atomic impact excitation and deexcitation cross-sections, v_e and v_a are respectively the relative velocities of the electron and atom collision partners, and A_{io} is the Einstein transition probabilities for spontaneous emission. Here, it is assumed the plume is sufficiently optically thin that absorption and stimulated emission may be neglected.

If electron-impact is considered dominant, the atomic impact terms can be neglected. This simplifies equation 4.21 to:

$$\frac{dn_i}{dt} = 0 = n_o n_e \langle \sigma_{eex} v_e \rangle - n_i n_e \langle \sigma_{edex} v_e \rangle - A_{io} n_i \tag{4.21}$$

and solving for the ratio of upper to ground state population leads to:

$$\frac{n_i}{n_o} = \frac{n_e \langle \sigma_{eex} v_e \rangle}{n_e \langle \sigma_{edex} v_e \rangle + A_{io}} \tag{4.22}$$

The excitation and deexcitation cross-sections are related by the Klein-Rosseland equation:

$$\sigma_{edex}(E) = \frac{g_l}{g_u} \left(\frac{E + \Delta E}{E} \right) \sigma_{eex}(E + \Delta E) \tag{4.23}$$

where E is the lower state energy, $E + \Delta E$ is the upper state energy, and g_l and g_u are the lower and upper state degeneracies. [81]

By the principle of *detailed balance*, at equilibrium, the collisional excitation and deexcitation rate constants must be related by:

$$\frac{\langle \sigma_{eex} v_e \rangle}{\langle \sigma_{edex} v_e \rangle} = \frac{g_i}{g_o} exp \left(-\frac{E_i}{kT} \right) \tag{4.24}$$

where g_i and g_o are the upper and lower state degeneracies. So if collisional processes dominate the population levels, (i.e. radiation losses are small), then the population ratio are given by the Boltzmann distribution:

$$\frac{n_i}{n_o} = \frac{g_i}{g_o} exp \left(-\frac{E_i}{kT} \right) \tag{4.25}$$

If radiation losses aren't negligible, then populations depart from the LTE approximation. Griem provides the rule of thumb that LTE requires collisional excitation rates to be 10 times greater than radiation rates. [43] If we require the collisional excitation rate to be 10 times greater than radiation losses, this leads to the requirement

$$n_o n_e \langle \sigma_{eex} v_e \rangle > 10 * n_i A_{io} \tag{4.26}$$

when solved for n_e results in

$$n_e > 10 \frac{A_{io}}{\langle \sigma_{eex} v_e \rangle} \frac{g_i}{g_o} exp\left(-\frac{E_i}{kT}\right) \tag{4.27}$$

It should immediately be noted that this condition varies line-by-line, depending on the A-coefficient and upper state energy. A transition with a strong A-coefficient requires a larger electron density to be in LTE than one with a weak A-coefficient. Likewise, transitions originating at higher energy levels require a lower electron density to be in LTE than transitions originating at lower energy levels. This may lead to deviations from LTE in the electronic state distributions of observed emitters.

With the above limitations kept in mind, a rough estimate is made here for the minimum value of n_e. For the 767 nm Ba I emission line, $A_{ij} = 1.5 * 10^7 s^{-1}$, $g_i = 5$, $g_j = 3$, and $E_i = 2.564$ eV. Since this is a rough estimate, an electron impact excitation cross-section of 5E-17 cm^2 and electron temperature of 1 eV will be used. This results in the estimate for the minimum number density:

$$n_e > 10 \frac{1.5 * 10^7}{5 * 10^{-17} cm^2 * \sqrt{\frac{8 * 1eV}{\pi 9.11 * 10^{-31} kg}}} \frac{5}{3} exp\left(-\frac{2.564eV}{1eV}\right) = 6.5 * 10^{15} cm^{-3} \tag{4.28}$$

As a comparison, this number is considerably less than the measured $n_e = 10^{17} cm^{-3}$ reported by Harilal for positions very close (d $\sim$ 3 mm) to the ablation surface. [45] However, data for the present study was collected at far greater distances (d $>$ 31.4 mm), so the electron densities given by reference [45] are not likely to be representative of the conditions observed far downstream. At best, one may consider it possible, but not certain, that electron densities are sufficiently high in the plume for LTE.

Another important consideration is knowing how well emission and excitation are spatially and temporally correlated, i.e, whether the observed photon was emitted

near where and when the excitation occurred. The critical distance scale for this experiment is the distance an atom in an excited state travels before emission, compared to the field-of-view of the instrument. Typical wavefront velocities recorded in this experiment are approximately $v = 10^6$ cm/sec. Again using $\tau_{1/2} = 10$ nsec as a typical radiative lifetime, the expected travel distance, d, before emission is:

$$d = v\tau_{1/2} = (10^6 cm/sec)(10nsec) = 0.1\ mm \tag{4.29}$$

which is within the 1 mm width of the field-of-view of the instrument. So it may be reasonably assumed that the spectrometer is observing photons within the same region where excitation occurred.

4.2.2 Electron-impact/LTE Model. With spectral data in hand, it is now possible to examine some key assumptions about the prevailing view that electron-impact under local thermodynamic equilibrium is responsible for excitation of and emission from electronic states of atoms in the plume. Recalling the definition of LTE by Griem, [43] LTE occurs if the plume is optically thin (loosens the requirement for a Planckian photon distribution), the kinetic energy distribution is Maxwellian, the electronic state distribution is Boltzmann, ionization is described by the Saha equation, and all temperatures are in agreement. The first of these criteria (optically thin plume) will now be examined.

If a plume is optically thick, it is likely that a photon will be absorbed and reemitted (possibly at a different wavelength), and if that happens enough times in a sufficiently dense plasma, the photon field will come into thermodynamic equilibrium with the matter, [43] and the spectral distribution of the radiation will be a Planckian:

$$M_p(\nu) = \frac{2\pi\nu^4}{c^3\left(exp\left(\frac{h\nu}{kT}\right) - 1\right)} \tag{4.30}$$

where $M_p(\nu)$ is the photon exitance, ν is the frequency of the emitted photon, h is Planck's constant, c is the speed of light, and kT is the temperature of the plasma. [77] This equation can be rearranged in terms of energy, E = hν as:

$$M_p(E) = \frac{2\pi E^4}{h^4 c^3 \left(exp\left(\frac{E}{kT}\right) - 1\right)} \tag{4.31}$$

If the above equation is now divided by E^4, and also approximated in the limit E >> kT, then the above equation can be rewritten as:

$$\frac{M_p(E)}{E^4} = Aexp\left(-\frac{E}{kT}\right) \tag{4.32}$$

where the miscellaneous constants have been collected into the constant A. Taking the natural log of both sides yields:

$$Ln\left(\frac{M_p(E)}{E^4}\right) = Ln(A) - \frac{E}{kT} \tag{4.33}$$

So if the photon distribution is Planckian, the ratio $M_p(E)/E^4$ determined from spectral data should be linear with respect to the photon energy, E. Since the fluence on the detector is the time integral of $M_p(E)$ multiplied by the constant radiometric factor d$\Omega/4\pi$, the emission line fluences, Φ_{ij} are substituted for $M_p(E)$. The result for Ba I data collected at 150 mTorr, 36.0 mm downstream from the ablation target are shown in Figure 4.18. The data is poorly correlated ($R^2 \sim 0.37$) which indicates the plume emission is not consistent with a Planckian distribution, so it can be concluded the plume is not optically thick. This is consistent with the assumption that the plume is in local (and not complete) thermodynamic equilibrium.

The next characteristic of LTE to be examined is the requirement for common temperatures among the available energy channels. Consider the case of a stationary atom of mass M that is excited by collisions with electrons of mass m. Conservation of mass and momentum restrict the amount of energy, W, available for internal excitation

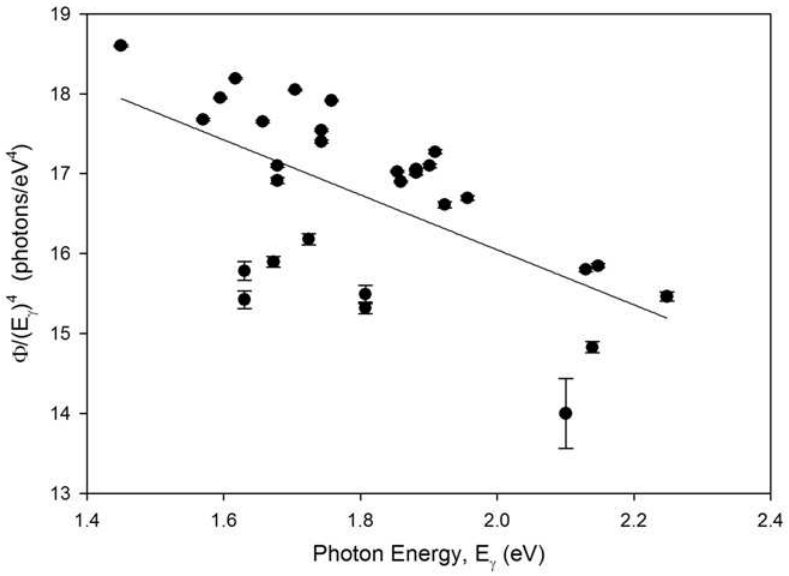

Figure 4.18: Ba I emission plotted in a Planckian plot. Poor correlation of fit ($R^2 \sim 0.37$) indicates the plume is not optically thick.

of the atom. The equations relating mass and momentum before and after collision are:

$$mv_{eo} = mv_{ef} + Mv_{af} \tag{4.34}$$

$$\frac{1}{2}mv_{eo}^2 = \frac{1}{2}mv_{ef}^2 + \frac{1}{2}Mv_{af}^2 + W \tag{4.35}$$

where v_{eo} and v_{ef} are the electron velocities before and after the collision, and v_{af} is the atom velocity after the collision. Assuming the masses and initial electron velocity are known, this leaves two equations and three unknowns (v_{ef}, v_{af}, and W). Nasser has shown that by differentiating equation 4.35, and substituting equation 4.35, the maximum fraction of initial kinetic energy converted into W can be determined, [61] which is:

$$f_{T\rightarrow E} = \frac{M}{m+M} \tag{4.36}$$

The kinetic energy of the electron is $\frac{1}{2}\mathrm{mv}^2$, so the maximum kinetic energy converted to electronic energy is:

$$\Delta E = \frac{mM}{m+M}\frac{v^2}{2} \approx \frac{1}{2}mv^2 \tag{4.37}$$

Here we have the result that for electronic excitation, the maximum energy transfer is independent of the mass of the atom, and equal to the kinetic energy of the colliding electron. This implies efficient transfer of energy from electron kinetic energy to the electronic states of the atoms. In the case of an electron gas that is in LTE, where the electronic states of the atom are in thermal contact, the population statistics of the electronic states may be described by the canonical ensemble:

$$P_i = \frac{g_i exp\left(-\frac{E_i}{kT}\right)}{\sum_r g_r exp\left(-\frac{E_r}{kT}\right)} \tag{4.38}$$

where P_i is the probability of occupation of state with energy E_i and degeneracy g_i, and the denominator is the sum over all energy levels E_r with degeneracy g_r. [64]

Here it should be noted the above result implies an electronic state distribution described essentially by one parameter–the temperature, kT. This implies that different atoms in equilibrium with the same electron gas should exhibit a common electronic temperature. It is clear in Figure 4.15, as well as similar charts in Appendix E that this is not the case – Cu temperatures are significantly elevated compared to Ba and Y. These results are consistent with prior observations of non-equilibrium behavior among quantum state distributions. Ying noted a similar temperature discrepancy among the three neutral species, but dismissed his results as an effect of the approximate nature of LTE. [91] In addition, prior measurements of YO emission spectra by Wiener revealed significant non-equilibrium among the vibrational and rotational excitation channels. [89] At this point, it is apparent the electron-impact/LTE model

is insufficient to explain the time-integrated electronic state distributions of Y, Ba, and Cu neutrals. However, temporal effects have not yet been taken into account, which is the next topic of discussion.

4.2.3 Temporal corrections to electron-impact/LTE model. To complete the analysis of the electron-impact/LTE model for electronic excitation, it is important to take into account time-variation of key factors important to emission. In prior work, Mao noted electronic temperatures are sensitive to signal integration time if the plume temperature changes significantly as the plume passes in front of the spectrometer. [56] In addition, Druffner noted the spatial distribution of Ba and Cu differed significantly, with the Cu angular distribution being more sharply peaked than Ba, i.e., Cu had a greater concentration in the interior of the plume, at the point of peak intensity than Ba. [25] Because the electronic temperature may change during observation, and the concentration of emitters may also change during data collection, a careless analysis of the emission spectra could lead to a wrong conclusion.

Consider the situation given in Figure 4.19. The curves are the normalized fluence (area under the curve = 1) for Ba ($\lambda = 767$ nm) and Cu ($\lambda = 809$ nm) neutral emission. Because both curves are normalized to the same area, this plot provides a weighting (or relative distribution) for the spatial distribution of emission. Looking at the position of highest flux, Cu has greater flux than Ba, while at later times, Ba has greater flux than Cu. This difference in distribution for Cu and Ba emission could result in a sampling bias between the two emitters. Still assuming electron-impact/LTE as the excitation mechanism, if the temperature profile rose rapidly to a maximum at the point of maximum Cu density, then quickly decayed, and the time integrated spectra was used to calculate the electronic temperature, the result would be a higher electronic temperature for Cu than for Ba, because Cu is spatially weighted in the hottest part of the plume compared to Ba. A model will now be presented to show the effect of temporal integration of plume radiation on measured electronic temperatures.

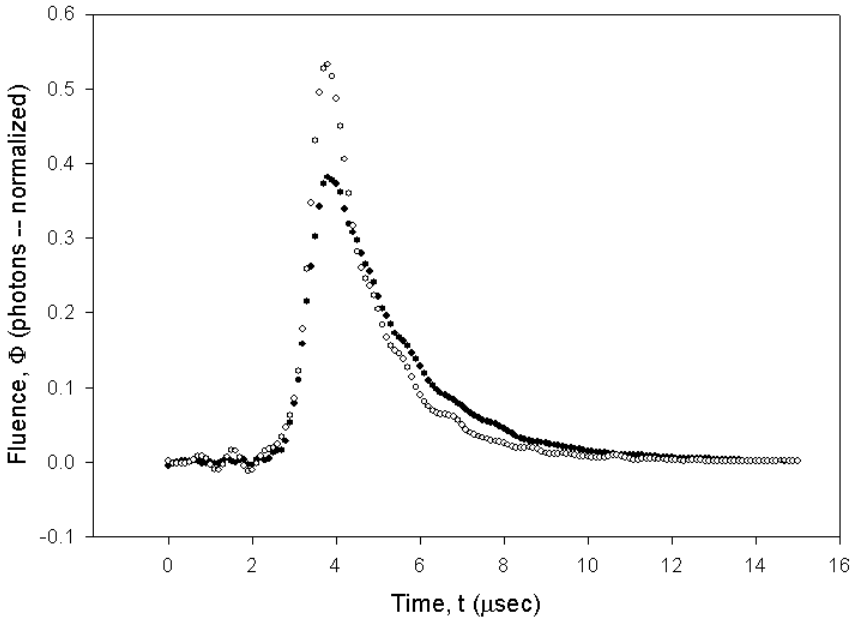

Figure 4.19: Normalized TOF curves for Ba and Cu recorded at 150 mTorr and 36 mm downstream from ablation target. Cu has a significantly higher photon flux than Ba at the point of maximum intensity. (○ – Cu, ● – Ba)

The spectral fluence, Φ_{ij}, recorded on a detector of an OMA is the integration of spectral flux from the plume, ϕ_{ij}(t), over an integration time, τ:

$$\Phi_{ij} = \int_0^\tau \phi_{ij}(t)dt = \int_0^\tau \frac{d\Omega_{OMA}}{4\pi} A_{ij} N_i(t)dt \tag{4.39}$$

where $d\Omega$ is the solid angle subtended by the OMA detector, and A_{ij} and N_i are as defined before. Using the Boltzmann population relation to express $N_i(t)$ leads to

$$\Phi_{ij} = \frac{d\Omega_{OMA}}{4\pi} A_{ij} \int_0^\tau N_o(t) \frac{g_i}{g_o} exp\left(-\frac{E_i}{kT(t)}\right) dt \tag{4.40}$$

Evaluating this expression requires knowing the ground state population as a function of time. The Mao model for plume dynamics assumes LTE with the electronic temperatures changing continuously with time. Consistent with this assumption, the ground state population may be calculated by using a spectrally-filtered time-of-flight

camera to monitor emission from an excited state, r, to a lower state s, and relating the excited and ground state populations using the Boltzmann distribution. Then Equation 4.40 may be rewritten as:

$$\frac{\Phi_{ij}}{A_{ij}g_i} = \frac{d\Omega_{OMA}}{4\pi}\int_0^\tau \frac{N_r(t)}{g_r} exp\left(-\frac{E_i - E_r}{kT(t)}\right) dt \tag{4.41}$$

The population of the upper state, $N_r(t)$ monitored by the time-of-flight camera can be determined from the time-of-flight flux, $\phi_r(t)$ by:

$$\phi_{rs}(t) = \frac{d\Omega_{CCD}}{4\pi} A_{rs} N_r(t) \tag{4.42}$$

where $d\Omega_{CCD}$ is the solid angle subtended by the CCD imagery detector, and A_{rs} is the transition probability for the emission line recorded by the time-of-flight instrument. Now Equation 4.41 may be expressed as

$$\frac{\Phi_{ij}}{A_{ij}g_i} = \frac{d\Omega_{OMA}}{d\Omega_{CCD}} \frac{1}{A_{rs}g_r} \int_0^\tau \phi_{rs}(t) exp\left(-\frac{E_i - E_r}{kT(t)}\right) dt \tag{4.43}$$

The left-hand side of equation 4.43 is obtained using spectral measurement, while the more complicated expression on the right-hand side involves a time-of-flight curve, $\phi_{rs}(t)$, an unknown temperature as a function of time, kT(t), and a few coefficients in front of the integral. This expression will soon be simplified by invoking a boundary condition, but first let's rewrite the time-of-flight curve as the product of its integrated intensity Φ_{rs}, and a normalized time-of-flight curve, $\phi_{rs}^{norm}(t)$:

$$\int_0^\tau \phi_{rs}(t)dt = \Phi_{rs} \int_0^\tau \phi_{rs}^{norm}(t)dt \tag{4.44}$$

where $\int_0^\tau \phi_{rs}^{norm}(t)dt = 1$. Now also consider the situation where the spectral line, i $\rightarrow$ j, on the left-hand side of equation 4.43 is the same line as the one monitored by the time-of-flight camera. This results in the boundary condition:

$$\left(\frac{\Phi_{ij}}{A_{ij}g_i}\right)_{ij=rs} = \frac{d\Omega_{OMA}}{d\Omega_{CCD}}\frac{\Phi_{rs}}{A_{rs}g_r} \tag{4.45}$$

This now allows equation 4.41 to be rewritten as:

$$\frac{\left(\frac{\Phi_{ij}}{A_{ij}g_i}\right)}{\left(\frac{\Phi_{ij}}{A_{ij}g_i}\right)_{ij=rs}} = \int_0^\tau \phi_{rs}^{norm}(t) exp\left(-\frac{E_i - E_r}{kT(t)}\right) dt \tag{4.46}$$

Here, equation 4.46 shows the emission fluence ratio for two lines (where one is the TOF line) can be calculated from the time-of-flight signal, provided the temperature as a function of time is known. What is desired is to invert the equation, i.e., to determine kT(t). The approach taken here is to use a parametric representation of kT(t) and determine what parameters result in a best fit for equation 4.46. Then with kT(t) determined using Ba I spectral data, Equation 4.39 can be used with Cu I energy levels to determine Cu I population levels, and subsequently, the Cu electronic temperature.

A nonlinear least-squares fit was the technique used to determine the optimum parameters for kT(t). The least squares fit determines the optimum fit by minimizing the objective function, χ^2, which is defined as:

$$\chi^2 = \Sigma\left[\frac{1}{\sigma_i}\left(y_i - F\left(x_i\right)\right)\right]^2 \tag{4.47}$$

where y_i is the dependent variable for the experimental data, σ_i is the error associated with y_i, $F((x_i)$ is the value of the fitting function F at the independent variable, x_i for the experimental data, and the summation is taken over i = 1 to n total data points to be fit. [14] Applied to the problem at hand, y_i was defined as:

$$y_i = \frac{\left(\frac{\Phi_{ij}}{A_{ij}g_i}\right)}{\left(\frac{\Phi_{ij}}{A_{ij}g_i}\right)_{ij=rs}} \tag{4.48}$$

while $F(x_i)$ was defined as:

$$\int_0^{\tau} \phi_{rs}^{norm}(t) exp\left(-\frac{E_i - E_r}{kT(t)}\right) dt \tag{4.49}$$

The Levenberg-Marquardt algorithm, implemented using the *lsqcurvefit* subroutine in the Matlab™ Optimization Toolbox, was used to fit the parametric expression for kT(t) to the experimental data.

The choice of a parametric function for kT(t) was driven primarily by the intent to investigate whether a suitable form of kT(t) would be consistent with the observed temperature differences between Ba and Cu. Thus, the forms of kT(t) are empirical, not physical. The physical constraints applied to kT(t) simply required the temperature to be equal to the background gas temperature prior to arrival of the plume, rise quickly to a maximum value, and decay to lower temperature (see Figure 2.4). The time corresponding to maximum temperature was chosen to occur at the point of maximum intensity, because this is where the weighting of Cu intensity compared to Ba intensity is at its greatest, and would result in a greater shift in calculated Cu electronic temperatures. (In reality, temperatures would be higher forward of this point because of shock heating in the contact front).

Several representations for kT(t) were tried, all having the characteristics of a rising leading edge, peaking at the point of maximum intensity, and with a decaying trailing edge. The two functions that consistently provided the best results were the ramp-Gaussian (equation 4.50) and ramp-decay (equation 4.51). The ramp-Gaussian has a constant background gas temperature, kT_o prior to the arrival of the shock front. At the time the shock front arrives, t_a, the temperature rises linearly to a maximum value, kT_{max} at time t_b. After time t_b the temperature function is a Gaussian centered at $t = t_b$, with the dispersion parameter σ. The ramp-decay function is similar to the ramp-Gaussian, except for the function decaying exponentially with time constant τ after reaching a maximum value, kT_{max} at $t = t_b$. The ramp-Gaussian and ramp-decay functions are given below. A sample plot of kT(t) derived from a ramp-Gaussian fit

Table 4.7: Ramp-Gaussian Parameters

P (mTorr) / d (mm)	kT_o (eV)	t_a (μsec)	t_b (μsec)	kT_{max} (eV)	σ (μsec)
50 / 31.4	0.026	1.7	2.7	0.33	2.72
50 / 36.0	0.030	2.0	3.2	0.35	2.57
50 / 45.7	0.038	2.8	4.7	0.28	20.27
50 / 55.0	0.045	3.6	6.4	0.36	2.37
150 / 31.4	0.026	2.2	3.0	0.34	20.16
150 / 36.0	0.030	2.6	3.8	0.30	24.18
150 / 45.7	0.038	4.5	6.3	0.32	21.66
150 / 55.0	0.045	7.0	9.3	0.42	16.52
400 / 31.4	0.026	3.0	3.5	0.36	39.99
400 / 36.0	0.030	3.4	4.1	0.36	29.82
400 / 45.7	0.038	6.4	8.3	0.32	24.44

is shown in Figure 4.20, and the resulting fit parameters are tabulated in Figures 4.7 and 4.8.

Ramp-Gaussian Fitting Function

$$kT(t) = \begin{cases} kT_o & (t < t_a) \\ \frac{kT_{max}-kT_o}{t_b-t_a}t + (kT_{max} - t_a\frac{kT_{max}-kT_o}{t_b-t_a}) & (t_a < t < t_b) \\ (kT_{max} - kT_o)exp(-\frac{(t-b)^2}{2\sigma^2}) + kT_o & (t_b < t) \end{cases} \tag{4.50}$$

Ramp-Decay Fitting Function

$$kT(t) = \begin{cases} kT_o & (t < t_a) \\ \frac{kT_{max}-kT_o}{t_b-t_a}t + (kT_{max} - t_a\frac{kT_{max}-kT_o}{t_b-t_a}) & (t_a < t < t_b) \\ (kT_{max} - kT_o)exp(-\frac{t}{\tau}) + kT_o & (t_b < t) \end{cases} \tag{4.51}$$

With the kT(t) determined from Ba spectral data, the next step is to use equation 4.46 to calculate the Cu electronic state distribution using the Cu normalized time-of-flight signal for ϕ_{rs}^{norm}, and where E_i refers to Cu electronic energy levels. The model electronic temperatures for Cu are then determined from the negative recipro-

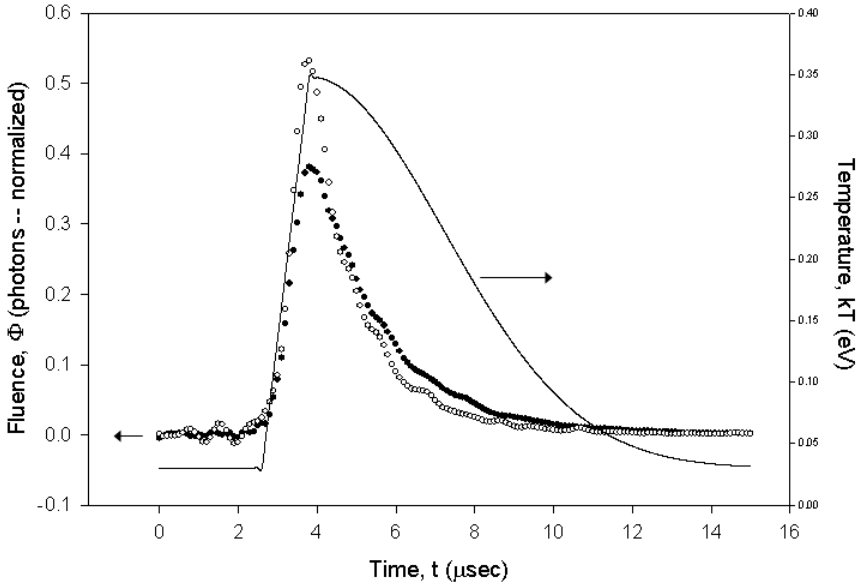

Figure 4.20: Electronic temperature (at 150 mTorr, 36 mm from background target) calculated using time-of-flight data, Ba emission data, and a ramp-Gaussian parametric fit. (∘ – Cu, • – Ba, solid line – kT)

Table 4.8: Ramp-decay Parameters

P (mTorr) / d (mm)	kT_o (eV)	t_a (μsec)	t_b (μsec)	kT_{max} (eV)	τ (μsec)
50 / 31.4	0.026	1.7	2.7	0.27	22221.1
50 / 36.0	0.030	2.0	3.2	0.34	5.17
50 / 45.7	0.038	2.8	4.7	0.25	60.10
50 / 55.0	0.045	3.6	6.4	0.35	2.92
150 / 31.4	0.026	2.2	3.0	0.28	81.03
150 / 36.0	0.030	2.6	3.8	0.27	33.61
150 / 45.7	0.038	4.5	6.3	0.29	56.90
150 / 55.0	0.045	7.0	9.3	0.39	37.91
400 / 31.4	0.026	3.0	3.5	0.34	179.24
400 / 36.0	0.030	3.4	4.1	0.34	90.34
400 / 45.7	0.038	6.4	8.3	0.29	76.87

Table 4.9: Temporal Model Results

P (mTorr) / d (mm)	observed kT_{Ba} (eV)	observed kT_{Cu} (eV)	model kT_{Cu}
50 / 31.4	0.29 ± 0.01	0.41 ± 0.02	0.31
50 / 36.0	0.30 ± 0.01	0.42 ± 0.02	0.33
50 / 45.7	0.27 ± 0.01	0.39 ± 0.03	0.28
50 / 55.0	0.29 ± 0.01	0.41 ± 0.01	0.32
150 / 31.4	0.32 ± 0.02	0.50 ± 0.05	0.34
150 / 36.0	0.30 ± 0.02	0.44 ± 0.03	0.30
150 / 45.7	0.30 ± 0.02	0.40 ± 0.02	0.31
150 / 55.0	0.27 ± 0.01	0.42 ± 0.04	0.40
400 / 31.4	0.35 ± 0.03	0.47 ± 0.03	0.36
400 / 36.0	0.35 ± 0.03	0.47 ± 0.02	0.36
400 / 45.7	0.31 ± 0.02	0.47 ± ***	0.31

*** Insufficient data points to estimate error

cal slope of a semilog plot of population vs upper state energy level. The calculated Cu temperatures are given in Table 4.9 and shown in Figure 4.21. Calculated Cu temperatures are slightly elevated compared to Ba, however, the ~ 0.02 eV difference appears inadequate to explain the 0.1 to 0.15 eV temperature difference observed between Ba and Cu. The failure of the temporal model to explain the temperature difference between Ba and Cu may result from the fitted kT(t) curve not being sharply peaked at the region of maximum intensity where the Cu time-of-flight curve has its greatest difference with the Ba time-of-flight curve. Because the kT(t) curve does not decay sharply, the sampling difference between Cu and Ba is unimportant.

Since the transient model fails to account for the different temperatures for Y, Ba, and Cu neutrals, it is reasonable to conclude that the electronic state distributions are in fact different, and are inconsistent with the electron-impact/LTE excitation mechanism widely reported and accepted in the literature. These results are consistent with prior reported work on atomic electronic state distributions by Ying [91] and El-Astal [28, 29]. It is also consistent with YO electronic state distributions measured by Weiner, [89] who noted nonequilibrium among YO spin-orbit, vibrational, and rotational temperatures, as well as non-equilibrium in the vibrational temperatures

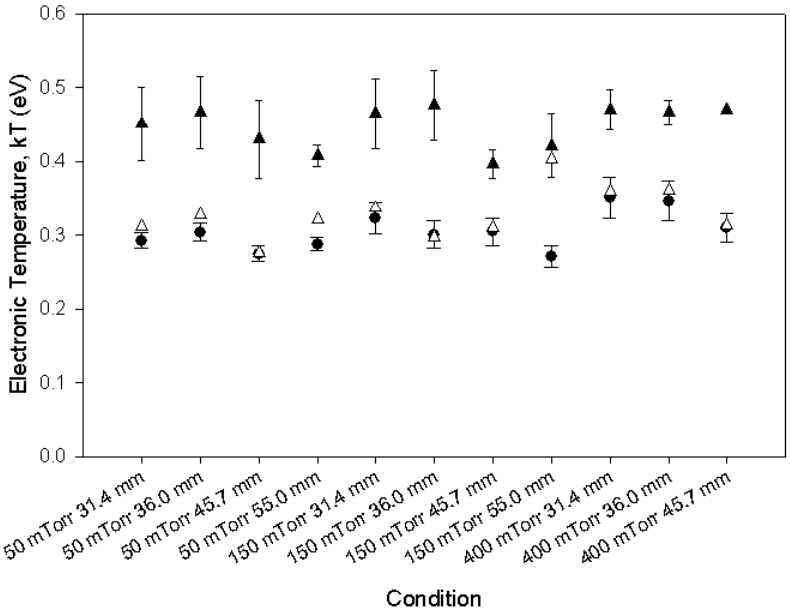

Figure 4.21: Copper neutral electronic temperatures calculated from the parametric time-dependent model compared against measured copper and barium electronic temperatures. The calculated Cu temperatures are slightly elevated compared to measured Ba temperatures, however the model appears insufficient to explain the discrepancy between Ba and Cu electronic temperatures. (• measured Ba I, △ calculated Cu I, ▲ measured Cu I)

for different spin states, and rotational temperatures for different spin states and vibrational levels.

There are significant consequences to concluding the plume is not in LTE. First, the disagreement in electronic temperatures for the three species is contradictory to what would be expected for a linkage between electronic temperatures and electron temperatures. The electron-impact excitation mechanism should result in a common temperature for the three species that were measured. Second, derivative conclusions that resulted from assuming LTE (such as using the Saha equation to determine ion and electron number densities) need to be reexamined. Finally, an alternative explanation is clearly needed to explain the origin of statistical electronic state distributions with different temperatures for each species. Attention now turns to heavier collision partners (atoms and molecules) as possible sources of excitation.

4.2.4 Atomic Impact Excitation. Although the observed electronic state distributions exhibit an energy dependence that is Boltzmann-like, the results of this experiment, specifically the different electronic temperatures for different emitter types, suggest the mechanism of electron-impact under LTE is deficient and other mechanisms should be considered. There are examples in the literature of Boltzmann-like distributions occurring in dynamic situations where LTE is not assumed, such as collisions between alkali dimers and halogens. [31,52] An information-theoretical approach using surprisal analysis was used to model the resulting product state distributions, resulting in exponential gap laws for electronic state distributions. [31,52] These prior results suggest looking at the atom-atom or atom-molecule collisions as a possible excitation mechanism. This approach will now be used to examine the mechanism of atomic impact excitation of electronic states.

The key concept in the information theoretical approach is the *maximal entropy postulate* which states that the most likely population distribution is the one with the greatest statistical entropy, [82] where the statistical entropy, S, is related to the probability of a state, $|i\rangle$, being occupied, X_i, is given by:

$$S = -\Sigma_i X_i ln\left(X_i\right) \tag{4.52}$$

To determine the maximum entropy, a functional, F, is defined which is the difference of the statistical entropy and the constraints on the problem

$$F = -\sum_i X_i ln\left(X_i\right) - \sum_g^r \lambda_g f_g \tag{4.53}$$

The summation on the right hand side of equation 4.53 are a set of Langrangian multipliers which constrain the solutions when the extremum of F is found by setting $\mathrm{dF}/\mathrm{d}X_i = 0$. Normalization as the sole constraint ($\sum_i^n X_i = 1$) leads to the conclusion that all states are equally probable (uniform distribution) [82]. This yields the same result as a microcanonical ensemble, which also predicts all energetically allowed states are equally probable. [71]. Constraints on F are needed to explain the Boltzmann-like distribution of excited state populations in YBCO emission spectra. Following the example of Faist, the constraint used is $\lambda_{exc} f_i$ where λ_{exc} is a parameter that will be fit from experimental data, and $f_i = E_i/E_{coll}$ is the ratio of the excited state energy, E_i to the collision energy, E_{coll}. [31] Using this as a constraint on equation 4.53 results in the maximum entropy distribution:

$$X_i = exp\left(-\lambda_o - \lambda_{exc} f_i\right) = exp\left(-\lambda_o\right) exp\left(-\frac{E_i}{\frac{E_{coll}}{\lambda_{exc}}}\right) \tag{4.54}$$

where λ_o is the normalization constraint. This function is very similar to the canonical distribution for a system brought into thermal contact with another system in equilibrium:

$$X_i = \frac{exp\left(-\frac{E_i}{kT}\right)}{\sum_k exp\left(-\frac{E_k}{kT}\right)} \tag{4.55}$$

where the factor E_{coll}/λ_{exc} corresponds to the canonical distribution temperature kT, while the normalization term $exp\,(-\lambda_o)$ corresponds to the denominator in the canonical distribution. Although the distribution functions appear similar, it should be remembered the origins are different: the canonical distribution arises from assuming the system under study is brought into thermal contact with a heat reservoir in thermal equilibrium, [71] while the information theoretical distribution does not require equilibrium, and is instead derived by finding the maximum entropy distribution consistent with conservation of collision energy. [82] Because the information theoretical approach does not assume the presence of an equilibriated heat reservoir, it may be suitable for modeling experimental data for a system not in LTE.

Returning to equation 4.54, this may be rewritten as the ratio of the observed probability a state is occupied, $P(i)$, to the the uniform probability, $P^o(i)$.

$$\frac{P(i)}{P^o(i)} = exp\,(-\lambda_{exc} f_i) = exp\left(-\lambda_{exc}\frac{E_i}{E_{coll}}\right) \tag{4.56}$$

The above result is similar to the Boltzmann population distribution, where kT has been replaced by E_{coll}/λ_{exc}. Further manipulation, by taking the the natural logarithm results in:

$$I(i) = -ln\left(\frac{P(i)}{P^o(i)}\right) = \lambda_{exc} f_i = \lambda_{exc}\frac{E_i}{E_{coll}} \tag{4.57}$$

The value of $I(i)$ in equation 4.57 is referred to as the *surprisal parameter* because it is the deviation from the prior expectation (uniform) distribution. Evaluation of equation 4.57 is straightforward. The calculation of $P^o(i)$ is found by dividing the degeneracy of the state $|i\rangle$ (obtained from energy level tables [65]) by the total number of electronic states in the atom:

$$P^o(i) = \frac{g_i}{\sum_i g_i} \tag{4.58}$$

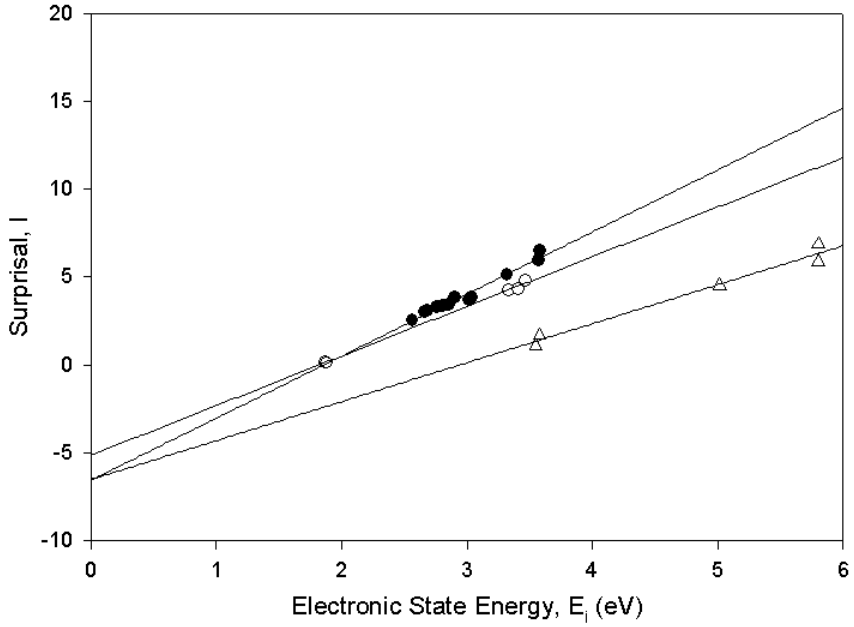

Figure 4.22: Surprisal plot for P=150 mTorr and d=36.0 mm. Each group appears to be explained by a separate linear constraint. (○ Y I, • Ba I, △ Cu I)

while $P(i)$ was obtained from spectral data using the relation

$$P(i) = \frac{\frac{\Phi_{ij}}{A_{ij}}}{\sum_i \frac{\Phi_{ij}}{A_{ij}}} \tag{4.59}$$

where it is noted that when multiple lines originate from the same upper state, the mean of the excited state populations is used in the calculation to avoid overcounting.

A sample surprisal plot is shown in Figure 4.22 for a background pressure of 150 mTorr and 36.0 mm downstream from the ablation target. Since the collision energy, E_{coll} is not known, the surprisal, I, is plotted against the excitation energy. The data appear to be linearly distributed, and the slope of the plot is interpreted as the ratio of the constraint, λ_{exc} to the collision energy, E_{coll}. The values of the ratio λ_{exc}/E_{coll} for Y, Ba, and Cu for all observed conditions are given in Table 4.10.

Table 4.10: Y/Ba/Cu Surprisal Analysis Parameters

P(mTorr)/d(mm)	$(\lambda/E_{coll})_Y$	$(\lambda/E_{coll})_{Ba}$	$(\lambda/E_{coll})_{Cu}$
50 / 31.4	2.88 ± 0.08	3.44 ± 0.18	2.55 ± 0.18
50 / 36.0	2.86 ± 0.09	3.41 ± 0.16	2.15 ± 0.18
50 / 45.7	3.55 ± 0.12	3.71 ± 0.13	2.29 ± 0.14
50 / 55.0	3.20 ± 0.22	3.47 ± 0.23	2.49 ± 0.08
150 / 31.4	2.73 ± 0.06	3.31 ± 0.23	2.22 ± 0.18
150 / 36.0	2.82 ± 0.08	3.53 ± 0.20	2.22 ± 0.21
150 / 45.7	3.12 ± 0.09	3.49 ± 0.21	2.63 ± 0.11
150 / 55.0	3.24 ± 0.18	3.84 ± 0.16	2.38 ± 0.02
400 / 31.4	2.79 ± 0.11	3.02 ± 0.26	2.24 ± 0.14
400 / 36.0	2.81 ± 0.13	3.08 ± 0.25	2.34 ± 0.21
400 / 45.7	3.23 ± 0.15	3.40 ± 0.24	2.13 ± ***
mean	3.02 ± 0.26	3.43 ± 0.24	2.33 ± 0.16

*** Insufficient data points to estimate error

The difficulty in interpreting the value of λ_{exc}/E_{coll} is that E_{coll} is not known, and λ_{exc} is signal-averaged over collisions with multiple types of collision partners (e.g. Y can collide with Y, Ba, Cu, O, YO, and O_2). The relative weighting of collision partners, determined from the hard-sphere collision frequencies for particle o colliding with particle a, ν_{oa}, was determined from:

$$\nu_{oa} = \frac{N_a \sigma_a v_a}{\sum_i N_a \sigma_a v_a} \tag{4.60}$$

where N_a is the number density of the collision partner, a, σ_a is the hard-sphere cross-section, v_a is the relative velocity, and the sum is over all collision partners. Assuming initial stoichiometry, the collision weighting fraction, ν_a can be expressed as:

$$\nu_a = \frac{R_a \left(d_o + d_a\right)^2 \left(\mu_{oa}\right)^{-1/2}}{\sum_i R_i \left(d_o + d_i\right)^2 \left(\mu_{oi}\right)^{-1/2}} \tag{4.61}$$

where d_o and d_i are the diameters of collision partners (taken from [80]), R_i is the stoichiometric number (1 for Y, 2 for Cu, 3 for Ba, and 7 for O), and μ_{oi} is the

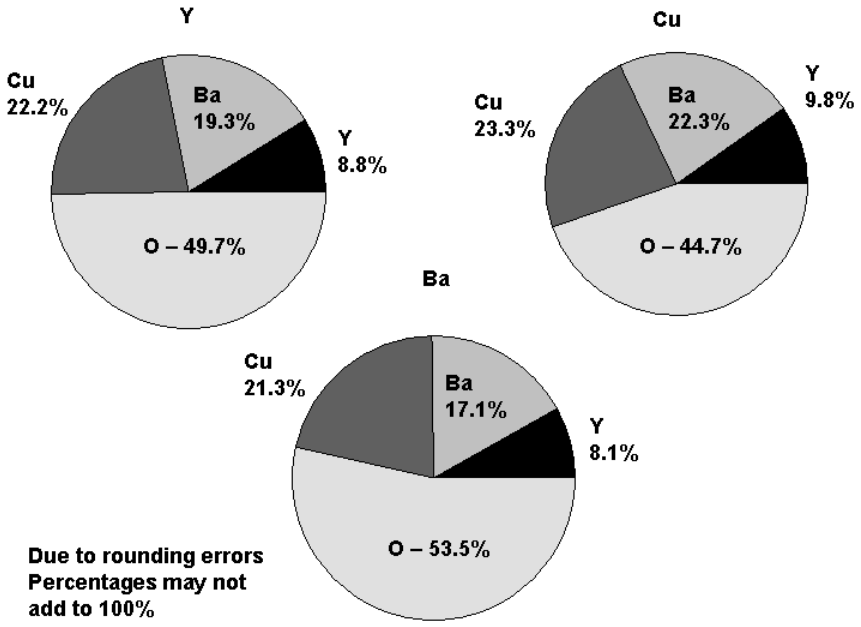

Figure 4.23: Pie charts for Y, Ba, and Cu show the collision weighting for their collision partners based on initial stoichiometry (neglecting collisions at the contact front). Oxygen is the most frequent collision partner for all three species)

reduced mass of the collision pair. The collision partner weighting is shown in Figure 4.23. The dominant collision partner for all three species is oxygen, accounting for approximately 50% of all collisions, followed by Cu, and Ba, with Y being the least frequent collision partner. There is some variation with respect to oxygen collision frequencies, with Ba having 54% of its collisions with O, while Cu only has about 45% of its collisions with O.

The collision partner weighting calculations so far only take into account in-plume collisions. Collisions at the contact front may distort the result, as the signal-averaging will include a greater amount of collisions with background oxygen as the collision partner, and the collision energy will depend on the velocity of the contact front relative to the shocked background gas. The effect is expected to be greatest with Ba since it has the greatest macroscopic cross section ($\Sigma = N\sigma$), and prior observations show reduction in number density along the line-of-observation for lighter elements at the contact front. [26]. If the collision energy is taken as the weighted

sum of the "in plume" component and a component resulting from collisions at the shock front, then the surprise parameter may be written as:

$$I(i) = \frac{\lambda_{exc}}{w_{plume}E_{plume} + w_{contact}E_{contact}}E_i \tag{4.62}$$

where w_{plume} and $w_{contact}$ are the weighting factors for collisions in the plume and at the contact front, and $w_{plume} + w_{contact} = 1$. Next, the contact front energy is rewritten as a function of shock strength, S, $E_{contact} = \alpha S$, where α is an unknown parameter. Then the surprisal parameter, I(i), may be rewritten as:

$$\begin{aligned} I(i) &= \frac{\lambda_{exc}}{w_{plume}E_{plume}(1 + \frac{w_{contact}\alpha}{w_{plume}E_{plume}}S)}E_i \\ &\simeq \frac{\lambda_{exc}}{w_{plume}E_{plume}}\left(1 - \frac{w_{contact}\alpha}{w_{plume}E_{plume}}S\right)E_i \end{aligned} \tag{4.63}$$

This would suggest a negative correlation between $\frac{\lambda_{exc}}{E_{coll}}$ and shock strength. Ba neutral $\frac{\lambda_{exc}}{E_{coll}}$ values are plotted against shock strength in Figure 4.24. The slope of the line suggests negative correlation, however, caution should be used in accepting this interpretation as the error bars are about the same magnitude as the variation in the data, and the Pearson R^2 coefficient of determination is only 0.57.

One modest use of Figure 4.24 will be used in comparing the values of $\frac{\lambda}{E_{coll}}$ for each species. The values of $\frac{\lambda}{E_{coll}}$ for Y and Cu do not significantly vary with S, but the values for Ba may vary with S. To do a comparison for $\frac{\lambda}{E_{coll}}$ for all three species, it's important to remove the effect of the contact front collisions. In making the comparisons, the value of $\frac{\lambda}{E_{coll}}$ for Ba I is taken in the limit where S $\rightarrow$ 0. Then it may be assumed that almost all of its excitation events occur inside the plume, and E_{coll} is common among Y, Ba, and Cu. The other key assumption is that the collision partner weighting is the same for Y, Ba, and Cu. As has already been discussed, there is a difference of about 10% between Ba and Cu for collisions with O, with smaller

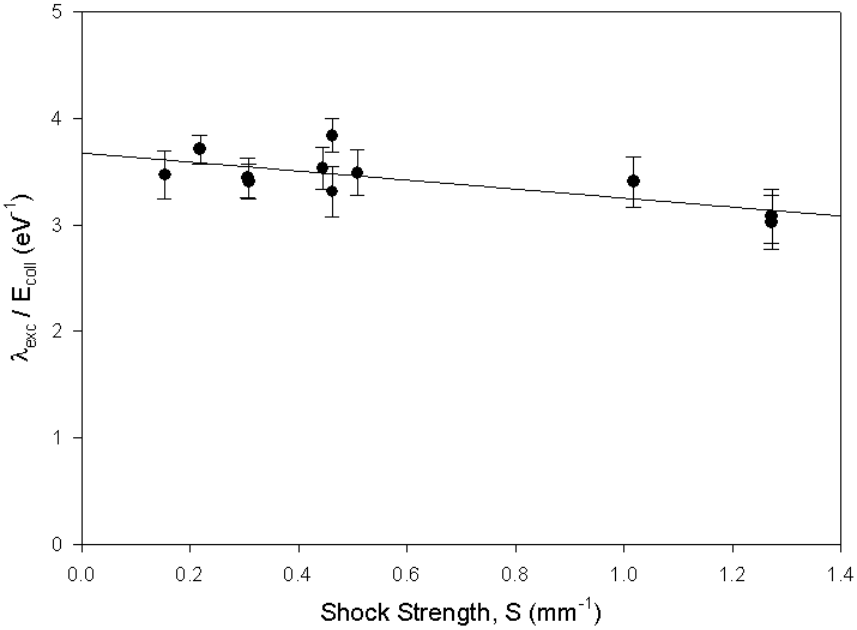

Figure 4.24: Ba I $\frac{\lambda}{E_{coll}}$ is plotted as a function of shock strength. Variation is on the same order as the error bars, while the R^2 coefficient of determination is a modest 0.57.

differences for the other collision partners. However, the pattern of distribution, with oxygen making up about half of all collision partners, with decreasing frequency of Cu, Ba, and Y is common among Y, Ba, and Cu. So it may be assumed that the signal-averaged value of λ_{exc} for Y, Ba, and Cu when divided by a common E_{coll} may be compared directly. The values of λ_{exc}/E_{coll} for Y, Ba, and Cu are plotted as a function of emitter mass in Figure 4.25. λ_{exc}/E_{coll} is trending upward with mass, suggesting that mass may be a factor in the dynamic constraint λ_{exc} on T $\rightarrow$ E energy transfer.

Using surprisal analysis to model the results of atomic impact excitation, it appears that a single linear parameter based on conservation of energy is sufficient to describe the product electronic state distributions. This parameter is different for each emitting species and may be related to the mass of the emitter. This parameter must be carefully interpreted. One may object that the surprisal analysis merely flipped Figure 4.15 to arrive at Figure 4.22. In fact, the values of $\frac{\lambda}{E+coll}$ given in

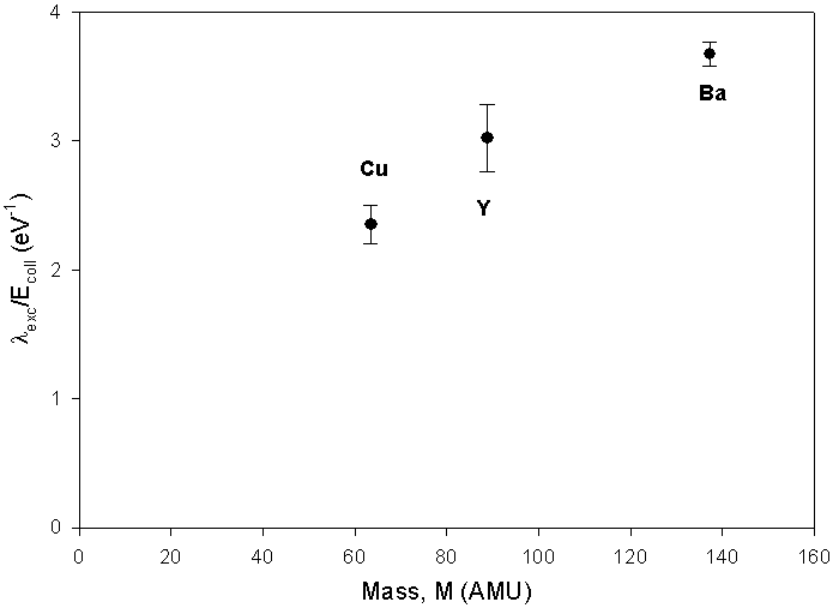

Figure 4.25: $\frac{\lambda}{E_{coll}}$ is plotted as a function of mass. Assuming E_{coll} is equal for all emitters, the dynamic constraint for each emitter is different. One possible factor in the constraint is the mass of the emitter.

Table 4.10 are in almost all cases numerically close to the reciprocal of the electronic temperatures given in Table E.34. However, the numbers represent two different physical pictures. Interpreting the electronic temperature in the context of LTE assumes the electronic state distribution is in equilibrium with the Maxwellian kinetic energy distribution of the electron collision partners, and that the electronic temperature is equal to the electron kinetic temperature. In contrast, the surprisal parameter, λ, should interpreted in the context of a maximum likelihood quantum state distribution constrained only by normalization and conservation of energy, and where a Boltzmann-like quantum state distribution does not imply a Maxwellian collision energy distribution. This provides a complementary and alternative interpretation of the electronic state distributions to the electron-impact/LTE excitation mechanism dominant in prior literature.

V. Summary and Conclusions

5.1 Summary

In this effort, a systematic study was conducted of electronic state distributions of Y, Ba, and Cu neutrals in plumes created by pulsed laser ablation of bulk YBCO. Spectral measurements were collected over the λ = 500 - 860nm wavelength band at various conditions of pressure (50, 150, and 400 mTorr), and position (31.4, 36.0, 45.7, and 55.0 mm from ablation target), using an optical multichannel analyzer calibrated for responsivity with a blackbody, and for wavelength using standard reference lamps. Emission lines were systematically assigned using standard reference lamps and tables of electronic energy levels. In this manner, 76 of 87 emission lines were assigned, the remainder are ambiguous or overlapped by the YO A $\rightarrow$ X emission band. Emission fluences were calculated by fitting Gaussian lineshapes to the spectral data. Electronic state distributions were calculated from the emission fluences and the latest NIST-reviewed transition probabilities. Boltzmann population distributions were fit to the data, which yielded electronic temperatures in the range 0.28-0.37 eV for yttrium neutrals, 0.28-0.35 eV for barium neutrals, and 0.40-0.48 eV for copper neutrals. The electronic temperatures were insensitive to position and oxygen background pressure.

Spectrally-filtered imagery was also collected using a fast-framing intensified-CCD camera with a narrowband ($\Delta\lambda \sim 1nm$) filter selected to pass Ba (767 nm) or Cu (809 nm) emission. Time-of-flight curves and shock strength curves were derived from the imagery for each spectral observation position. The time-of-flight data was used to model possible temporal signal-averaging effects on measured electronic state distributions. The results show a modest difference between measured Ba and calculated Cu temperatures which, however, are not on the same scale as the observed difference ($\sim$ 0.14 eV) between Ba and Cu temperatures. The different electronic temperatures for each observed specie of emitters, even accounting for temporal signal averaging effects, is consistent with prior reported results. [28, 29, 91] This leads to the conclusion that the laser-ablated YBCO plume is not in LTE.

Shock strength calculations, and their weak linear relationship to electronic temperatures provided a clue to atom-atom or atom-molecule collisions as possible mechanism for electronic excitation. An information theoretical approach was used to model electron state distributions, resulting in a linear dynamic constraint for the conversion of kinetic energy to electronic excitation energy, with excitation rates described by an exponential gap law.

5.2 Conclusions

The preceding analysis leads to the following conclusions:

1) Electronic temperatures are different by species. The emission spectra collected in this experiment, when fit to the Boltzmann population distribution, results in distinctly different temperatures for each species. The electronic temperatures follow the general pattern of Ba being the coolest (0.28-0.35 eV), Cu being the hottest (0.40-0.48 eV), and Y (0.28-0.37 eV) in between Ba and Cu for every observed condition. This type of temperature pattern has been observed before, [91] but not followed through to its logical consequence (discrepancy with LTE), and is restated here to support the following conclusions.

2) The plume under study is optically thin for most wavelengths. Ba I emissions terminating on the ^3D metastable state experienced self-absorption that was modeled (and corrected) using the Beer-Lambert model for absorption (see Figure 4.14. The plume was not optically thick, because the photon energies were not adequately described by a Planckian distribution as shown in Figure 4.18.

3) Temporal modeling does not explain observed electronic temperature differences. The argument by Mao that signal integration time may have a significant effect on the measured electronic temperatures if the plume's plasma temperature is rapidly varying [56] would provide a possible explanation for elevated Cu temperatures relative to Ba if the temperature were strongly peaked during the $\sim 1\mu$sec when the normalized Cu emission exceeds that of Ba. However, modeling temporal behavior

using time-of-flight curves and spectral data do not predict a this temperature behavior as a function of time, and the modeled time-averaged temperature differences for Ba and Cu are not on the same scale as was measured in this experiment.

4) Local Thermodynamic Equilibrium does not explain observed spectra. Although spectral data, when modeled to the Boltzmann population equation results in linear fits on a semilog plot, the temperatures derived from the fits do not agree among each other. This is inconsistent with LTE.

5) Emission spectroscopy is a poor process control diagnostic technique A good process control diagnostic technique is one that has a deep dynamic range with respect to a measurable plume variable that can be correlated with some desired end state (in this case, quality of deposited YBCO film). In this experiment, the most significant factor that correlated with electronic temperatures was the emitting species. In addition to this, Ba I electronic temperatures showed a weak dependence on shock strength. Otherwise, electronic temperatures appeared to be insensitive to plume position and oxygen background pressure.

5.3 Recommendations for Future Research

Several factors limited the outcome of this effort. First, the spectral coverage of the spectrometer limited collection of data to the 500-860 nm range. The lack of coverage in the 400-500 nm range prevented collection of enough Ba and Y ion emission lines to determine their electronic temperatures. Second, the spectra were temporally-integrated over the duration of the plume passage past the field of view of the sensor in order to improve spectral signal-to-noise. While this aided fitting and assignment of emission lines, this came at the expense of sacrificing temporal resolution. Finally, spatial coverage was limited to four $\sim$ 1 mm x 1 mm collection positions. This, in combination with the lack of temporal resolution, means the variation of electronic temperatures as a function of position in the plume is unknown. The spatial distribution of electronic temperatures would provide more insight into

the electronic excitation mechanism, especially the role played by collisions along the contact front between plume constituents and the background oxygen gas. The following recommendations are provided to address the limitations of the present study. Performing the following experiments would require acquisition of additional equipment and modest changes in ablation conditions.

The first recommendation would be to extend the lower wavelength limit on spectral coverage from 500 nm to at least 400 nm. This would enable collecting enough yttrium and barium ion emission lines to determine their electronic state distributions. In this work, ionization ratios presented in Table 4.6 were calculated assuming equal ion and neutral temperatures. This assumption may not be valid. Measurement of ion temperatures would indicate whether ion and neutrals are not in LTE, and allow a more accurate estimation of the ionization ratio.

The second recommendation would be to conduct a time- and spatially-resolved measurement of ESDs. The present approach integrated the signal for the duration of the plume to obtain good signal to noise to aid assignment of the emission spectra. To do this, the ability to make time-resolved measurements was discarded. A time-resolved measurement of ESDs could be made by restricting the gate, and sweeping the delay from the trigger. This would enable monitoring the plume from a dynamic situation at the shock front until it approaches equilibrium at some point in the plume tail. This effort would be a significant undertaking and would have its own limitations. This approach would generate a tremendous volume of spectral data requiring analysis. The most efficient technique for analyzing spectra would be to switch from the interactive Peakfit^{TM} software to a scripted peakfitting package. Alternatives could include Tablecurve, the open source package *fityk*, or a custom developed Matlab^{TM} script. Signal-to-noise from the reduced gate width would pose a challenge, requiring a large number of shots to overcome this limitation. Shot numbers are limited as well, as target erosion will eventually affect plume characteristics.

The third recommendation is to exploit the significant capabilities of the gated, intensified CCD imager to construct 2-dimensional maps of electronic state distributions. This could be done by passing the plume image through a beam splitter, and imaging each beam with a separate, intensified CCD imager. One imager would be filtered at a reference wavelength, and the other imager at several emission wavelengths for the same element. Comparison of the emission fluences would enable calculation of electronic state distributions as a function of position and time. An additional twist on this technique would be to vary the position of the object focal plane to create 3D reconstructions of the plume via computer tomography. Since it was established by Druffner that relative angular distributions of Ba and Cu are correlated with film critical currents, extension from 2D to 3D may add additional fidelity to this technique. [25]

Appendix A. Calibration

The spectra collected by the optical multichannel analyzer (OMA) were used to calculate the electronic state distributions of the emitting species. For accurate results, it was necessary to calibrate the OMA. Two different types of calibration were performed: wavelength calibration and spectral response calibration. Wavelength calibration determines the dispersion of the diffraction grating, in other words, the relationship between pixel channel and the wavelength of the collected light. This is a prerequisite for assigning quantum state transitions to the observed emission lines. The other calibration process, spectral response calibration, determines the efficiency with which the incident photon fluence results in signal counts read out from the detector. Spectral response varies with wavelength, and is a function of transmission losses, grating efficiency, and detector response, each of which is a wavelength dependent process. The techniques used to perform wavelength and spectral response calibrations are presented below.

A.1 Wavelength Calibration

Interpretation of the spectral output of an OMA is aided by converting the pixel coordinates into units of wavelength. This conversion is performed by recording the line spectra of a standard lamp and fitting a 2nd degree polynomial to the measured line positions and wavelengths of known emission line from a standard lamp.

Initial wavelength calibration was performed using an Oriel^{TM} Hg/Ar standard emission lamp which was driven by a power supply operating at a fixed current and voltage. Three Hg emission lines (546.07, 576.97 and 579.07 nm) were used as reference lines for the polynomial fit. The OMA manufacturer's WinSpec^{TM} data acquisition software was used to calculate the polynomial fit. The polynomial coefficients were recorded in the data acquisition software settings and used during subsequent data collections, and pixel coordinates were recorded in wavelength units in data recorded by the OMA.

The wavelength calibration of recorded PLD spectra was refined further by comparison to Cathodeon^{TM} Ba/Ar, Y/Ne, and Cu/Ne standard emission lamps. PLD spectra lines were compared to the standard lamps to perform initial line assignment. A linear regression was performed between reference and measured emission line center wavelengths to determine a wavelength correction for PLD emission lines that were not matched to a standard lamp. This correction ensured estimated line positions were reasonably close to correct line positions, and eliminated a possible source of systematic error in the line assignment process.

A.2 Instrument Spectral Responsivity

Prior to calculation of the electronic state distribution of a species, it is first necessary to calculate the photon spectra from the detector counts collected by an OMA. To do this conversion, it is necessary to calculate the OMA's spectral responsivity curve. The spectral responsivity, R(λ), of an OMA is defined as the signal output, s, divided by the photon irradiance, E, on the entrance slit.

$$R(\lambda) = \frac{s(\lambda)_{out}}{E_{ph}(\lambda)_{in}} \tag{A.1}$$

Calculating the spectral response is then a matter of measuring the signal output resulting from a known spectral irradiance. For this experiment, the OMA was calibrated using a blackbody source using the two temperature technique described by Wadsworth, [87] which corrects for signal originating from partially non-Planckian sources. First we write the output signal as being the product of the spectral responsivity and the sum of blackbody and nonblackbody photon sources:

$$s(\lambda) = R(\lambda)(E_{BB}(\lambda, T) + E_{nonBB}(\lambda)) \tag{A.2}$$

If two signal measurements are taken at different temperatures, T_1 and T_2, the responsivity can then be calculated as a difference of the above equation with itself at the two different temperatures. This results in:

$$R_{rel}(\lambda) = \frac{s(\lambda, T_2) - s(\lambda, T_1)}{E(\lambda, T_2) - E(\lambda, T_1)} \tag{A.3}$$

The relationship between the irradiance, $E(\lambda)$, and the radiant exitance of the source, $M(\lambda)$ is linear, with the proportionality constant determined by the geometry of the source:

$$E(\lambda)dA = \frac{d\Omega}{4\pi}M(\lambda) \tag{A.4}$$

where $d\Omega$ is the solid angle subtended by a differential area on the detector, dA. Because the grating in an OMA disperses the light onto the grating, the wavelength changes continuously from one end of the pixel to another. The total signal out of the detector is the sum of all wavelengths collected on the detector. So the irradiance averaged over the pixel area, A, can be written as:

$$E(\lambda) = \frac{d\Omega}{4\pi A}\int_{\lambda_0}^{\lambda_1} M(\lambda)\, d\lambda \simeq \frac{d\Omega}{4\pi A}M(\lambda)\Delta\lambda \tag{A.5}$$

where $\Delta\lambda$ is the width of the pixel in units of wavelength. If the blackbody is thermally stable, the count rate s is constant, and then the total count on the detector S, is a product of s and the accumulation time, Δt. Then the spectral responsivity may be expressed as:

$$R_{rel}(\lambda) = k\frac{S(\lambda, T_2) - S(\lambda, T_1)}{M_p(\lambda, T_2) - M_p(\lambda, T_1)} \tag{A.6}$$

where the proportionality constant $k = 1 \,/\, (\frac{d\Omega}{4\pi}\, \Delta t \Delta\lambda)$ and the photon radiant exitance $M_p(\lambda, T)$, is given by the Planck radiation law [77]:

$$M_p(\lambda, T) = \frac{2\pi c}{\lambda^4} \frac{1}{exp(\frac{hc}{\lambda kT}) - 1} \tag{A.7}$$

Since measurement of electronic state distributions depends on the relative intensities, instead of absolute intensities of spectral lines, a relative responsivity calibration is sufficient, as long as the calibration is conducted under consistent conditions across the entire wavelength bandpass of the OMA. Thus the proportionality constant k can be arbitrarily set to any value, provided it has units of dimensions $1/(\text{sec m}^3)$. This will enable conversion of counts on a detector strip into a spectrum with units of photons.

The instrument was calibrated with an Electro-optical Industries Model LS1250-100 blackbody at 1250 K and 1500 K. The results are shown in Figure A.1. $R_{rel}(\lambda)$ is well defined in the red, but becomes noisy in the blue. This is expected due to the decreasing difference in the spectral radiances at these wavelengths (see Figure A.2). Additional structure includes multiple local maxima and regions where the responsivity is multivalued. This structure is a result of the dependency of grating reflectivity on incident and reflective angle [23], and from assembling the responsivity curve from multiple wavelength bandpasses. The band center wavelength is changed by rotating the diffraction grating, which changes the incident angle, regions of overlapped coverage on two neighboring bandpasses will be measured with two different incident angles of the diffraction grating, resulting in different values on the responsivity curve.

The measured spectral responsivity compares favorably with the manufacturer's data for the ICCD detector [1]. The Pi-Max ICCD detector response has known cutoffs near 500 nm and 900 nm with a positive response between these endpoints.

Since alignment of the spectrometer may shift between blackbody calibration and recording of the PLD spectra, a polynomial expression was fit to the spectral responsivity:

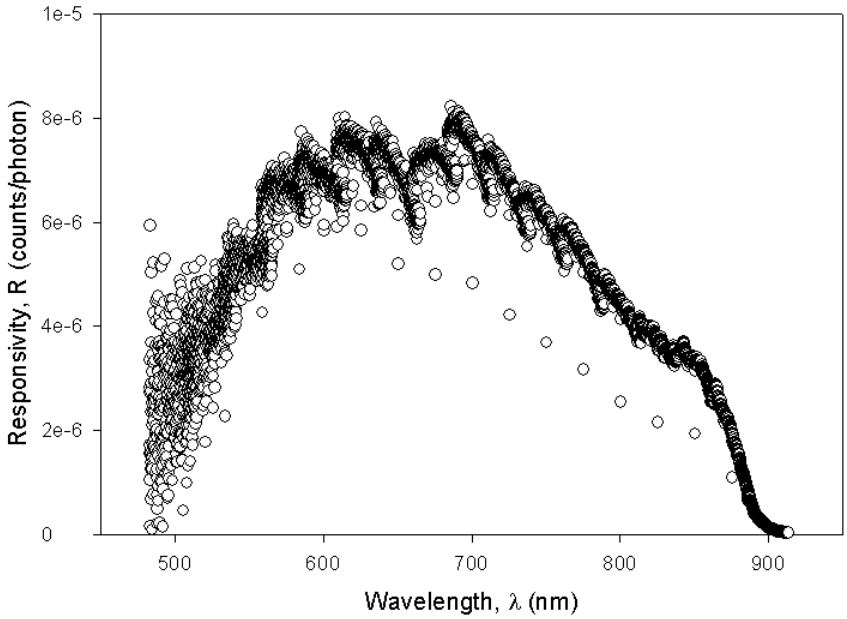

Figure A.1: Relative spectral responsivity of optical multichannel analyzer. Responsivity of given data points indicate responsivity relative to one another, not in absolute terms.

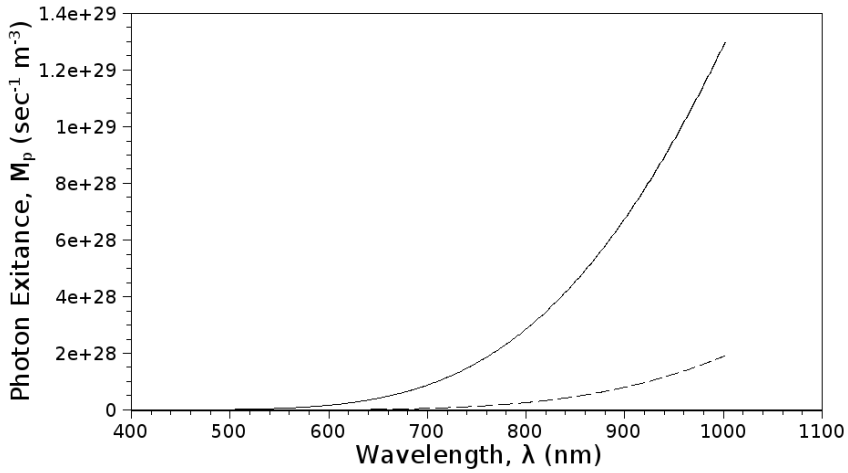

Figure A.2: Blackbody photon exitance predicted by Planck radiation law. (–, 1500 K, --, 1250 K)

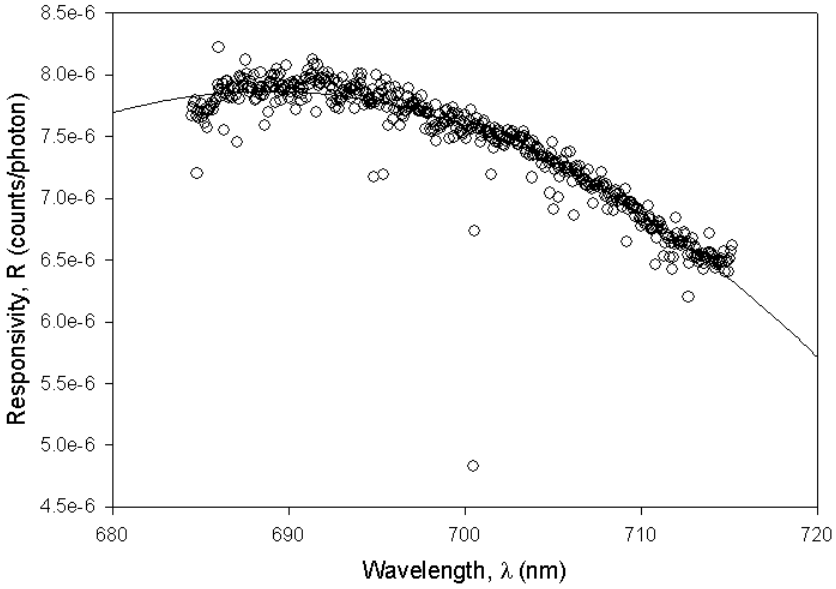

Figure A.3: Polynomial fit of the spectral response curve.

$$R_{rel}(\lambda) = \sum_i a_i \lambda^i \tag{A.8}$$

The average deviation between the polynomial fit and the measured responsivity was used as the error in the responsivity. This is expressed as:

$$\sigma_R = \frac{\sum_{i=1}^{n} (R_{calc}(\lambda_i) - R_{measured}(\lambda_i))}{n} \tag{A.9}$$

Table A.1: Spectral Responsivity Polynomial Coefficients

window (nm)	a_0 $\frac{counts}{photon}$	a_1 $\frac{counts}{photonnm}$	a_2 $\frac{counts}{photonnm^2}$	a_3 $\frac{counts}{photonnm^3}$	σ_R $\frac{counts}{photon}$
500	-1.61E-05	3.73E-8	0	0	7.38E-7
525	-1.70E-05	4.00E-08	0	0	4.03E-07
550	-3.37E-04	1.23E-6	-1.10E-09	0	2.85E-06
575	-6.05E-04	2.13E-06	-1.85E-09	0	1.70E-07
600	-3.12E-04	1.08E-06	-9.21E-10	0	1.46E-07

Table A.1: Spectral Responsivity Polynomial Coefficients – Continued

window (nm)	a_0 $\frac{counts}{photon}$	a_1 $\frac{counts}{photonnm}$	a_2 $\frac{counts}{photonnm^2}$	a_3 $\frac{counts}{photonnm^3}$	σ_R $\frac{counts}{photon}$
625	-7.82E-04	2.55E-06	-2.06E-09	0	1.19E-07
650	-7.44E-04	2.36E-06	-1.86E-09	0	1.04E-07
675	-9.20E-04	2.75E-06	-2.03E-09	0	9.52E-08
700	-1.04E-03	3.05E-06	-2.21E-09	0	8.36E-08
725	-6.58E-04	1.89E-06	-1.34E-09	0	7.22E-08
750	-6.98E-04	1.92E-06	-1.31E-09	0	5.76E-08
775	-8.74E-04	2.32E-06	-1.53E-09	0	6.18E-08
800	-4.91E-04	1.28E-06	-8.27E-10	0	4.90E-08
825	-2.54E-04	6.51E-07	-4.11E-10	0	6.22E-08
850	-1.36E-03	3.23E-06	-1.92E-09	0	7.41E-08

A.3 Instrument Linewidth Characterization

Instrument linewidth was measured as a function of the input slit width. Ne (λ = 650.65 nm) spectra were recorded at slit input widths ranging from 10 to 200 μm. Gaussian lineshapes were fit to the observed emission lines, with the standard deviation used as the linewidth. The results are presented in (see Figure A.4), and indicate an optimum value for a slit width near 50-60 μm. One interesting feature in the plot is the increase in linewidth at slitwidths less than the optimal value. It is noted that for dispersion from a diffraction grating, the linewidth of the central maximum is proportional to 1/N, where N is the number of illuminated grooves on the grating. [23] Thus, one possible explanation for the increased linewidth at decreasing slitwidth is that below an optimum value, the grating is no longer fully illuminated, and as the slitwidth decreases further, more of the grating falls into shadow, decreasing the groove count, N, resulting in increased instrument linewidth.

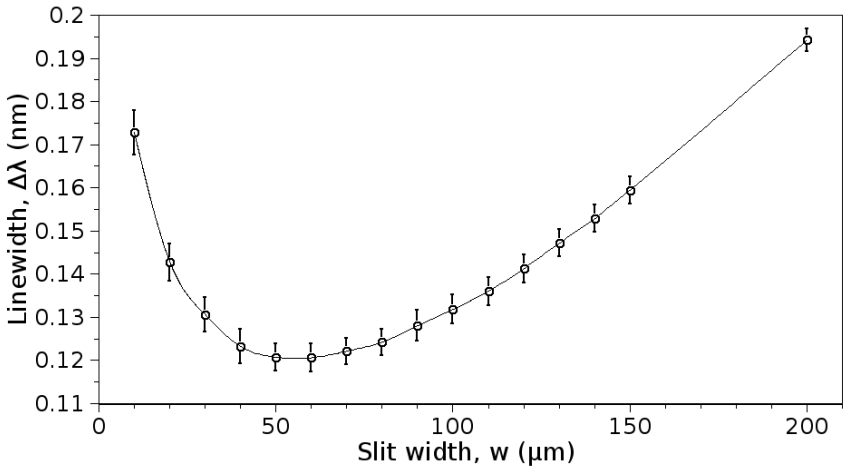

Figure A.4: OMA linewidth measured as a function of slit width.

Appendix B. Transition Probabilities

The tables below present the transition probabilities, A_{ij}'s used for computing electronic state distributions from line spectra. In all cases shown here, transition probabilities originate from experimental data. Sources used include the NIST online database [6], the CRC Handbook of Chemistry and Physics [3] and Optical Emission Lines of the Elements [65]. The given relative errors are taken from the references, and are defined as:

$$\sigma_{rel} = \frac{\sigma_{A_{ij}}}{A_{ij}} \tag{B.1}$$

where $\sigma_{A_{ij}}$ is the absolute error of the transition probability

B.1 Yttrium

Table B.1: Y I transition probabilities

λ (nm)	lower state	upper state	$A_{ik}(10^8 sec^{-1})$	σ_{rel}	source
546.646	4d2(3F)5s $^4F_{4.5}$	4d5s(a3D)5pz $^4G^o_{5.5}$	0.63	0.25	[6]
552.754	4d2(3F)5s $^4F_{3.5}$	4d5s(a3D)5pz $^4G^o_{4.5}$	0.54	0.25	[6]
560.633	4d2(3F)5s $^4F_{4.5}$	4d5s(a3D)5pz $^4G^o_{5.5}$	0.0584	0.25	[6]
563.013	4d2(3F)5s $^4F_{1.5}$	4d5s(a3D)5pz $^4G^o_{2.5}$	0.49	0.25	[6]
567.527	4d2(3F)5s $^4F_{2.5}$	4d5s(a3D)5pz $^4G^o_{2.5}$	0.093	0.25	[6]
619.173	4d5s2 $^2D_{1.5}$	4d5s(a3D)5pz $^2D^o_{1.5}$	0.047	0.25	[6]
622.259	4d5s2 $^2D_{1.5}$	4d5s(a3D)5pz $^2D^o_{2.5}$	0.0059	0.25	[6]
640.201	4d5s2 $^2D_{2.5}$	4d5s(a3D)5pz $^2D^o_{1.5}$	0.0027	0.25	[6]
643.500	4d5s2 $^2D_{2.5}$	4d5s(a3D)5pz $^2D^o_{2.5}$	0.040	0.25	[6]

B.2 Barium

Table B.2: Ba I transition probabilities

λ (nm)	lower state	upper state	$A_{ik}(10^8 sec^{-1})$	σ_{rel}	source
551.9044	6s6p $^3P^o_1$	6s6d $^3D_2$	0.57	0.25	[6]
553.548	6s2 $^1S_0$	6s6p $^1P^o_0$	1.19	0.03	[6]
577.7618	6s6p $^3P^o_2$	6s6d $^3D_3$	0.8	0.25	[6]
580.023	6s6p $^3P^o_1$	6s6d $^3D_2$	0.24	0.25	[6]
580.5681	6s5d $^3D_3$	5d6p $^1F^o_3$	0.011	0.25	[3]
582.6274	6s5d $^1D_2$	5d6p $^1P^o_1$	0.45	0.1	[6]
590.7636	6s5d $^3D_1$	5d6p $^3P^o_2$	0.015	0.25	[6]
597.1698	6s5d $^3D_2$	5d6p $^3P^o_2$	0.16	0.25	[6]
599.7087	6s5d $^3D_1$	5d6p $^3P^o_1$	0.28	0.25	[6]
601.947	6s5d $^3D_1$	5d6p $^3P^o_0$	0.81	0.25	[6]
606.3114	6s5d $^3D_2$	5d6p $^3P^o_1$	0.56	0.25	[6]
611.08	6s5d $^3D_3$	5d6p $^3P^o_2$	0.55	0.25	[6]
634.168	6s5d $^3D_2$	5d6p $^3D^o_3$	0.12	0.25	[6]
645.0851	6s5d $^3D_1$	5d6p $^3D^o_2$	0.11	0.1	[6]
648.2908	6s5d $^1D_2$	5d6p $^1F^o_3$	0.44	0.25	[3]
649.876	6s5d $^3D_3$	5d6p $^3D^o_3$	0.54	0.25	[6]
652.7311	6s5d $^3D_2$	5d6p $^3D^o_2$	0.33	0.1	[6]
659.5325	6s5d $^3D_1$	5d6p $^3D^o_1$	0.38	0.1	[6]
667.527	6s5d $^3D_2$	5d6p $^3D^o_1$	0.189	0.1	[6]
669.3842	6s5d $^3D_3$	5d6p $^3D^o_2$	0.146	0.1	[6]
686.5686	6s5d $^1D_2$	5d6p $^3P^o_2$	0.023	0.25	[3]
705.9943	6s5d $^3D_3$	5d6p $^3F^o_4$	0.5	0.25	[6]
712.0331	6s5d $^3D_1$	5d6p $^1D^o_2$	0.11	0.25	[6]
719.523	6s6p $^3P^o_0$	6s7s $^3S_1$	0.056	0.25	[6]
728.0296	6s5d $^3D_2$	5d6p $^3F^o_3$	0.32	0.25	[6]
739.2405	6s6p $^3P^o_1$	6s7s $^3S_1$	0.18	0.25	[6]
741.7536	6s5d $^3D_3$	5d6p $^1D^o_2$	0.0077	0.25	[6]
748.8075	6s5d $^3D_3$	5d6p $^3F^o_3$	0.073	0.25	[6]
761.0477	6s5d $^1D_2$	5d6p $^3D^o_2$	0.011	0.25	[6]
767.2085	6s5d $^3D_1$	5d6p $^3F^o_2$	0.15	0.25	[6]
778.0478	6s5d $^3D_2$	5d6p $^3F^o_2$	0.076	0.25	[6]
790.5747	6s6p $^3P^o_2$	6s7s $^3S_1$	0.27	0.25	[6]
791.1329	6s2 $^1S_0$	6s6p $^3P^o_0$	0.00298	0.25	[3]
856.000	6s5d $^1D_2$	5d6p $^1D^o_2$	0.2	0.25	[6]

B.3 Copper

Table B.3: Cu I transition probabilities

λ (nm)	lower state	upper state	$A_{ik}(10^8 sec^{-1})$	σ_{rel}	source
510.554	3d9 4s2 $^2D_{2.5}$	3d10(1S)4p $^2P^o{}_{1.5}$	0.02	0.25	[6]
515.324	3d10(1S)4p $^2P^o{}_{0.5}$	3d10(1S)4d $^2D_{1.5}$	0.60	0.25	[6]
521.82	3d10(1S)4p $^2P^o{}_{1.5}$	3d10(1S)4d $^2D_{2.5}$	0.75	0.25	[3]
522.01	3d10(1S)4p $^2P^o{}_{1.5}$	3d10(1S)4d $^2D_{1.5}$	0.15	0.25	[3]
570.02	3d9 4s2 $^2D_{1.5}$	3d10(1S)4p $^2P^o{}_{1.5}$	0.0024	0.25	[3]
578.213	3d9 4s2 $^2D_{1.5}$	3d10(1S)4p $^2P^o{}_{0.5}$	0.0165	0.25	[6]
793.313	3d10(1S)4p $^2P^o{}_{0.5}$	3d10(1S)5s $^2S_{0.5}$	0.22	0.25	[65]
809.2631	3d10(1S)4p $^2P^o{}_{1.5}$	3d10(1S)5s $^2S_{0.5}$	0.46	0.25	[65]

Appendix C. Emission Line Assignments

Correct assignment of emission lines to specific electronic transitions is key to determining electronic excited state distributions. Assignments were made by comparing emission line spectra to strong emission spectra seen in Cathodeon^{TM} Y/Ne, Ba/Ar, and Cu/Ne reference lamps, where buffer gas interference lines were identified by comparison to emission spectra from Oriel^{TM} Ne and Ar lamps. Assignments were performed sequentially in ascending order of upper state energy level, accounting for transitions to all lower states. Initial assignments were performed at oxygen background pressure of 150 mTorr at 36.0 mm from the target. This condition provided excellent signal to noise compared to other conditions. The table of assignments, given below, was used as an aid to assign transitions at other conditions. In this table, λ_{ctr} refers to the measured line center, Source, lower and upper state refer to the assigned emission source (element and ionization stage) and the upper and lower transition states, λ_{ref} refers to the reference wavelength of the assigned transition, and lamp indicates whether the emission line was visible in the calibration lamp spectra.

Table C.1: Table of Representative Line Assignments

λ_{ctr} (nm)	Source	lower state	upper state	λ_{ref} (nm)	lamp
490.100	unk	-	-	-	-
493.498	Ba II	5p6(1S)6s $^2S_{0.5}$	5p6(1S)6p $^2P^o_{0.5}$	493.408	$\surd$
508.800	Y II	4d2 $^3F_4$	4d(2D)5p z $^3F^o_4$	508.742	-
510.611	Cu I	3d9 4s2 $^2D_{2.5}$	3d10(1S)4p $^2P^o_{1.5}$	510.554	$\surd$
515.391	Cu I	3d10(1S)4p $^2P^o_{0.5}$	3d10(1S)4d $^2D_{1.5}$	515.324	-
520.129	Y II	4d2 $^3F_2$	4d(2D)5p z $^3F^o_2$	520.042	-
520.655	Y II	4d2 $^3F_2$	4d(2D)5p z $^3F^o_3$	520.572	-
521.834	Cu I	3d10(1S)4p $^2P^o_{1.5}$	3d10(1S)4d $^2D_{2.5}$	521.820	-
522.160	Cu I	3d10(1S)4p $^2P^o_{1.5}$	3d10(1S)4d $^2D_{1.5}$	522.007	-
542.499	Ba I	6s(2S)6p $^3P^o_0$	6s(2S)6d $^3D_1$	542.455	$\surd$
543.894	unk	-	-	-	-
546.738	Y I	4d2(3F)5s $^4F_{4.5}$	4d5s(a3D)5pz $^2D^o_{5.5}$	546.646	-

Table C.1 Table of Representative Line Assignments – Continued

λ_{ctr} (nm)	Source	lower state	upper state	λ_{ref} (nm)	lamp
550.467	unk	-	-	-	-
552.051	Ba I	6s6p $^3P^o_1$	6s6d $^3D_2$	551.904	√
552.867	Y I	4d2(3F)5s $^4F_{3.5}$	4d5s(a3D)5pz $^2D^o_{4.5}$	552.754	-
553.615	Ba I	6s2 $^1S_0$	6s6p $^1P^o_0$	553.548	√
557.887	unk	-	-	-	-
558.319	Y I	4d2(3F)5s $^4F_{2.5}$	4d2(a 3F)5p z $^4G^o_{3.5}$	558.183	-
560.710	Y I	4d2(3F)5s $^4F_{4.5}$	4d5s(a3D)5pz $^2D^o_{4.5}$	560.632	-
563.082	Y I	4d2(3F)5s $^4F_{1.5}$	4d5s(a3D)5pz $^2D^o_{2.5}$	563.013	-
564.540	Y I	4d2(3F)5s $^4F_{3.5}$	4d2(a 3F)5p z $^4G^o_{3.5}$	564.466	-
564.947	unk	-	-	-	-
566.359	unk	-	-	-	-
567.617	Y I	4d2(3F)5s $^4F_{2.5}$	4d5s(a3D)5pz $^2D^o_{2.5}$	567.527	-
570.133	Cu I	3d9 4s2 $^2D_{1.5}$	3d10(1S)4p $^2P^o_{1.5}$	570.02	-
570.742	unk	-	-	-	-
577.854	Ba I	6s6p $^3P^o_2$	6s6d $^3D_3$	577.762	√
578.322	Cu I	3d9 4s2 $^2D_{1.5}$	3d10(1S)4p $^2P^o_{0.5}$	578.213	-
580.166	Ba I	6s6p $^3P^o_1$	6s6d $^3D_2$	580.023	√
580.716	Ba I	6s5d $^3D_3$	5d6p $^1F^o_3$	580.568	√
582.733	Ba I	6s5d $^1D_2$	5d6p $^1P^o_1$	582.627	√
585.436	Ba II	5p6(1S)5d $^2D_{1.5}$	5p6(1S)6p $^2P^o_{1.5}$	585.367	√
590.862	Ba I	6s5d $^3D_1$	5d6p $^3P^o_2$	590.764	√
597.374	Ba I	6s5d $^3D_2$	5d6p $^3P^o_2$	597.170	√
598.983	YO	-	-	-	-
599.832	Ba I	6s5d $^3D_1$	5d6p $^3P^o_1$	599.709	√
600.561	YO	-	-	-	-
600.993	unk	-	-	-	-

Table C.1 Table of Representative Line Assignments – Continued

λ_{ctr} (nm)	Source	lower state	upper state	λ_{ref} (nm)	lamp
602.114	Ba I	6s5d $^3D_1$	5d6p $^3P^o_0$	601.947	√
602.494	unk	-	-	-	-
603.885	YO	-	-	-	-
605.616	YO	-	-	-	-
606.453	Ba I	6s5d $^3D_2$	5d6p $^3P^o_1$	606.311	√
607.341	YO	-	-	-	-
611.107	Ba I	6s5d $^3D_3$	5d6p $^3P^o_2$	611.08	√
613.326	YO	-	-	-	-
614.177	Ba I	5p6(1S)5d $^2D_{2.5}$	5p6(1S)6p $^2P^o_{1.5}$	614.171	√
614.966	YO	-	-	-	-
616.616	YO	-	-	-	-
618.335	YO	-	-	-	-
619.180	Y I	4d5s2 $^2D_{1.5}$	4d5s(a3D)5pz	619.173	√
620.044	unk	-	-	-	-
622.281	Y I	4d5s2 $^2D_{1.5}$	4d5s(a3D)5pz $^2D^o_{2.5}$	622.259	-
634.217	Ba I	6s5d $^3D_2$	5d6p $^3D^o_3$	634.168	√
640.276	Y I	4d5s2 $^2D_{2.5}$	4d5s(a3D)5pz $^2D^o_{1.5}$	640.201	-
643.604	Y I	4d5s2 $^2D_{2.5}$	4d5s(a3D)5pz $^2D^o_{2.5}$	643.500	√
645.202	Ba I	6s5d $^3D_1$	5d6p $^3D^o_2$	645.085	√
648.434	Ba I	6s5d $^1D_2$	5d6p $^1F^o_3$	648.291	√
649.803	Ba II	5p6(1S)5d $^2D_{1.5}$	5p6(1S)6p $^2P^o_{0.5}$	649.690	√
649.990	Ba I	6s5d $^3D_3$	5d6p $^3D^o_3$	649.876	√
652.874	Ba I	6s5d $^3D_2$	5d6p $^3D^o_2$	652.731	√
659.612	Ba I	6s5d $^3D_1$	5d6p $^3D^o_1$	659.533	√
667.592	Ba I	6s5d $^3D_2$	5d6p $^3D^o_1$	667.527	√
668.845	Y I	4d 5s2 $^2D_{1.5}$	4d 5s2(a 3D)5p z $^4F^o_{1.5}$	668.757	-

Table C.1 Table of Representative Line Assignments – Continued

λ_{ctr} (nm)	Source	lower state	upper state	λ_{ref} (nm)	lamp
669.457	Ba I	6s5d $^3D_3$	5d6p $^3D^o_2$	669.384	√
670.104	Y I	4d2(1G)5s $^2G_{3.5}$	4d2(a 3F)5p z $^2G^o_{3.5}$	670.064	-
679.517	Y I	4d 5s2 $^2D_{2.5}$	4d 5s2(a 3D)5p z $^4F^o_{2.5}$	679.371	√
686.688	Ba I	6s5d $^1D_2$	5d6p $^3P^o_2$	686.569	√
706.133	Ba I	6s5d $^3D_3$	5d6p $^3F^o_4$	705.994	√
712.099	Ba I	6s5d $^3D_1$	5d6p $^1D^o_2$	712.033	√
719.588	Ba I	6s6p $^3P^o_0$	6s7s $^3S_1$	719.523	√
728.105	Ba I	6s5d $^3D_2$	5d6p $^3F^o_3$	728.030	√
739.335	Ba I	6s6p $^3P^o_1$	6s7s $^3S_1$	739.241	√
741.896	Ba I	6s5d $^3D_3$	5d6p $^1D^o_2$	741.754	-
746.202	unk	-	-	-	-
748.972	Ba I	6s5d $^3D_3$	5d6p $^3F^o_3$	748.808	√
761.172	Ba I	6s5d $^1D_2$	5d6p $^3D^o_2$	761.048	-
764.408	unk	-	-	-	-
767.296	Ba I	6s5d $^3D_1$	5d6p $^3F^o_2$	767.209	√
778.169	Ba I	6s5d $^3D_2$	5d6p $^3F^o_2$	778.048	√
790.690	Ba I	6s6p $^3P^o_2$	6s7s $^3S_1$	790.575	√
791.250	Ba I	6s2 $^1S_0$	6s6p $^3P^o_0$	791.133	√
793.452	Cu I	3d10(1S)4p $^2P^o_{0.5}$	3d10(1S)5s $^2S_{0.5}$	793.313	√
809.436	Cu I	3d10(1S)4p $^2P^o_{1.5}$	3d10(1S)5s $^2S_{0.5}$	809.263	√
821.203	Ba I	6s(2S)6p $^1P^o_1$	6s(2S)6d $^1D_2$	821.025	√
844.88	O I	-	-	-	-
856.218	Ba I	6s5d $^1D_2$	5d6p $^1D^o_2$	856.000	√

Appendix D. Spectral Data

This appendix lists spectral data used to compute the electronic state distributions at each observed condition. The first section includes calibrated spectral charts, the second section gives the emission line fluences for the calibrated spectra., the third section provides the Beer-Lambert coefficients for emission lines terminating on the Ba ^3D metastable state, and the fourth section lists the corrected fluences of the self-absorbed emission lines.

D.1 Spectra

The spectral given below were assembled from the overlapping bandpasses with center wavelengths ranging from 500-850 nm. Photon fluences, Φ, were determined from signal counts, S, using spectral response, R, of the optical multichannel analyzer:

$$\Phi = \frac{S}{R} \tag{D.1}$$

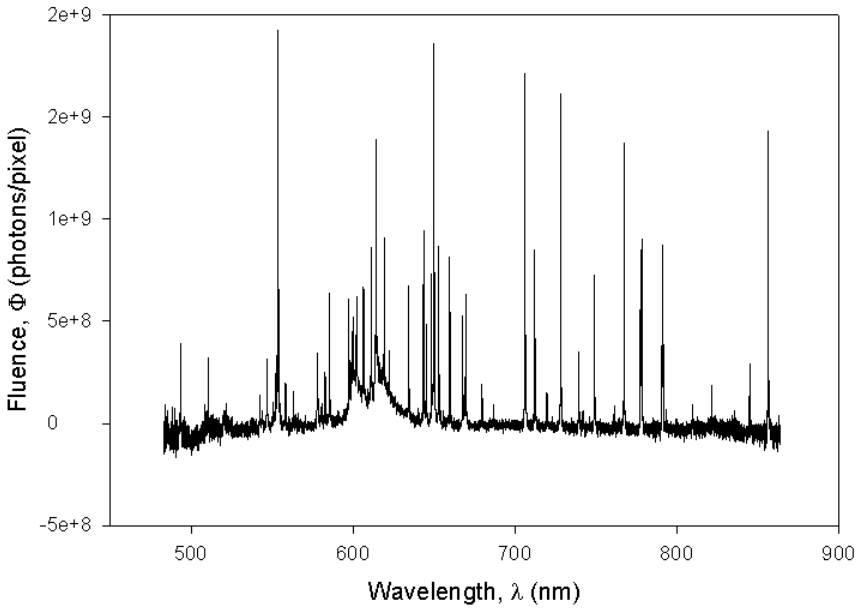

Figure D.1: Calibrated spectrum–50 mTorr, 31.4 mm.

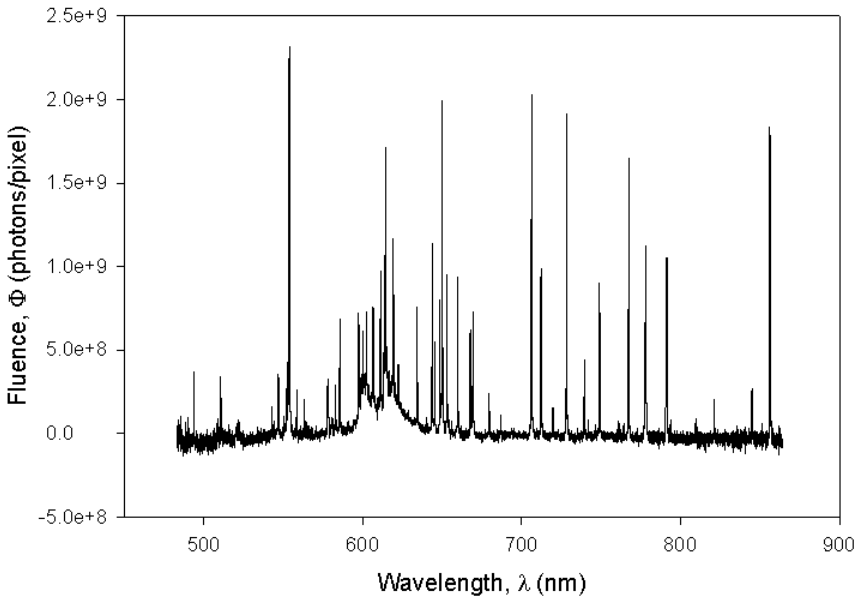

Figure D.2: Calibrated spectrum–50 mTorr, 36.0 mm.

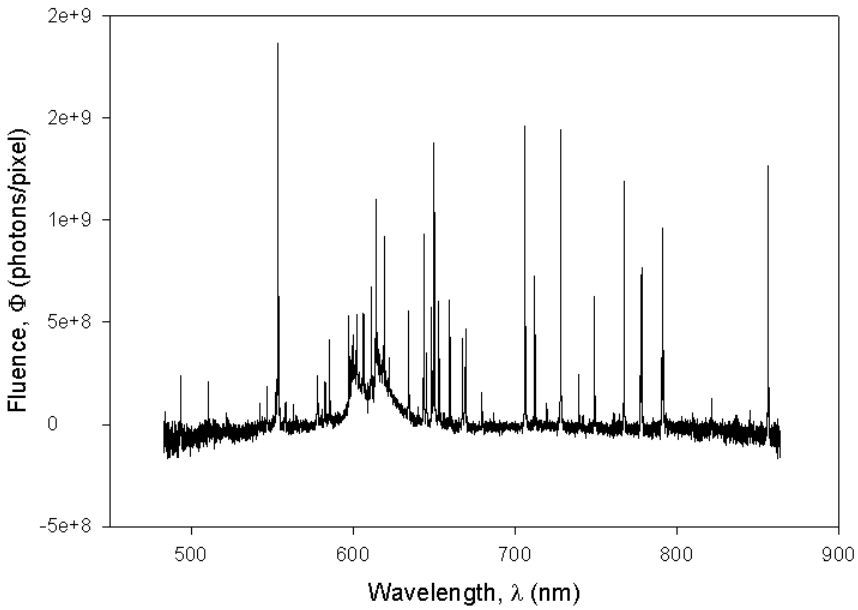

Figure D.3: Calibrated spectrum–50 mTorr, 45.7 mm.

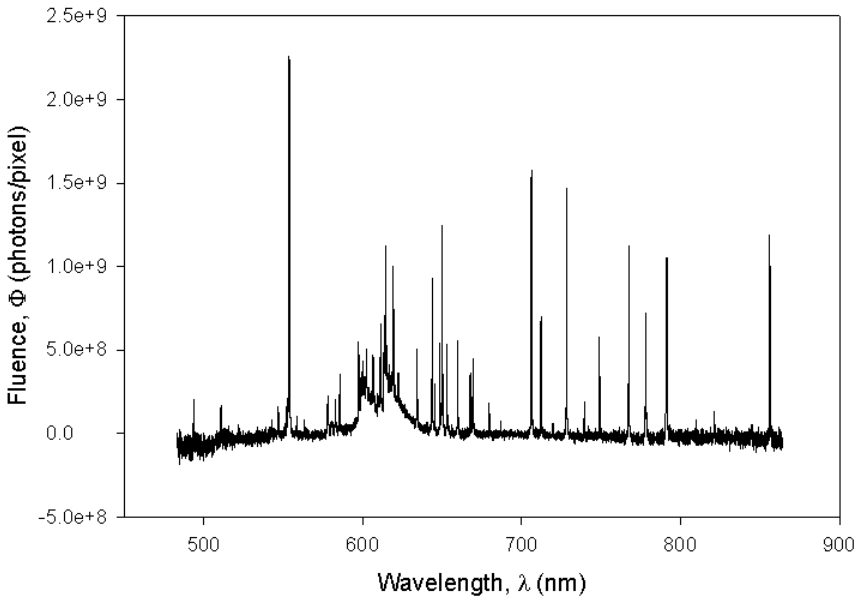

Figure D.4: Calibrated spectrum–50 mTorr, 55.0 mm.

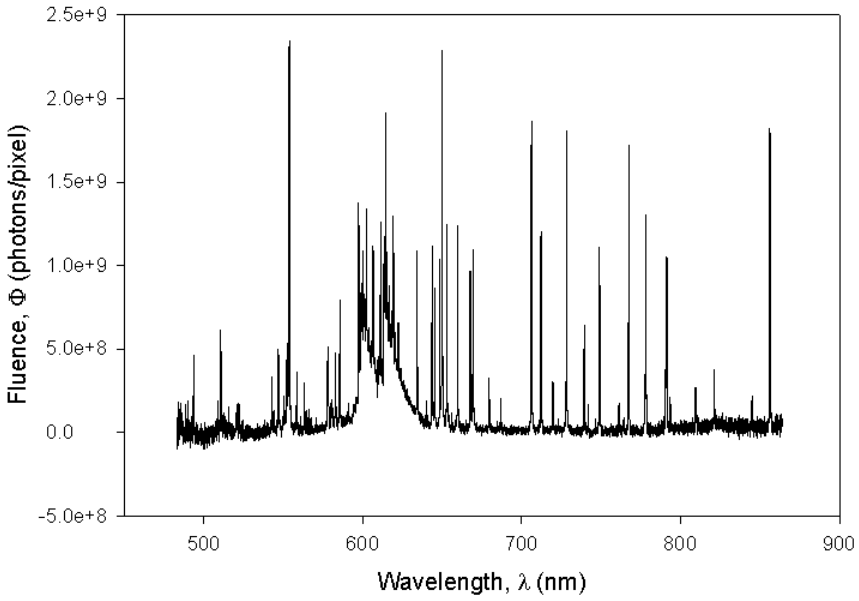

Figure D.5: Calibrated spectrum–150 mTorr, 31.4 mm.

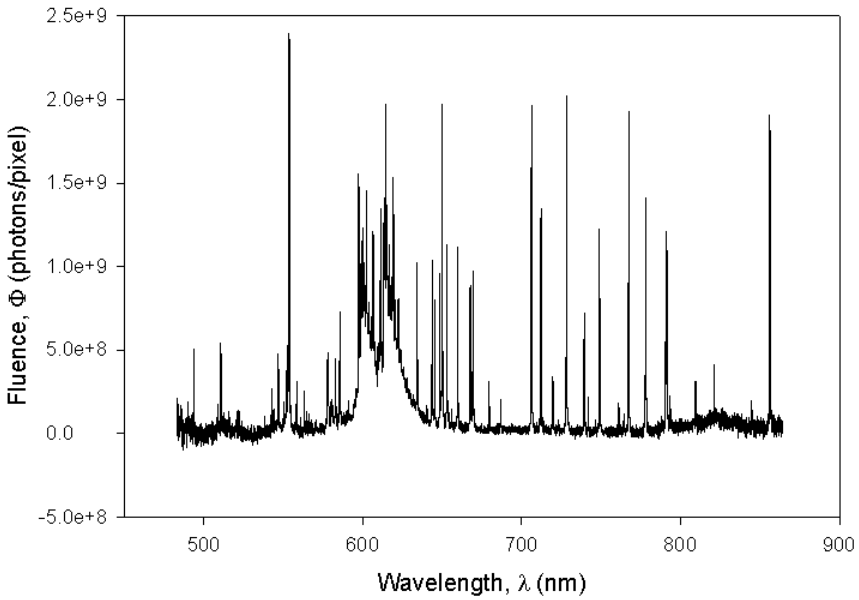

Figure D.6: Calibrated spectrum–150 mTorr, 36.0 mm.

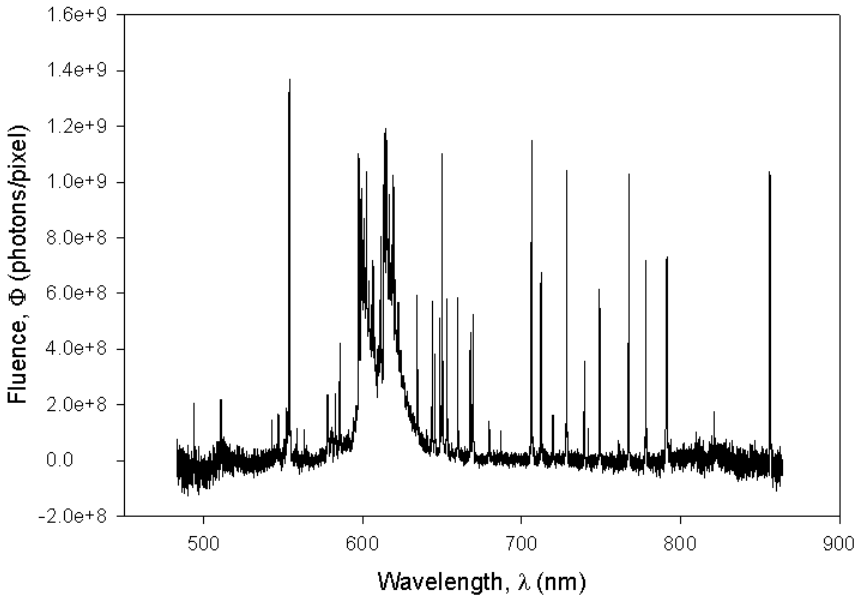

Figure D.7: Calibrated spectrum–150 mTorr, 45.7 mm.

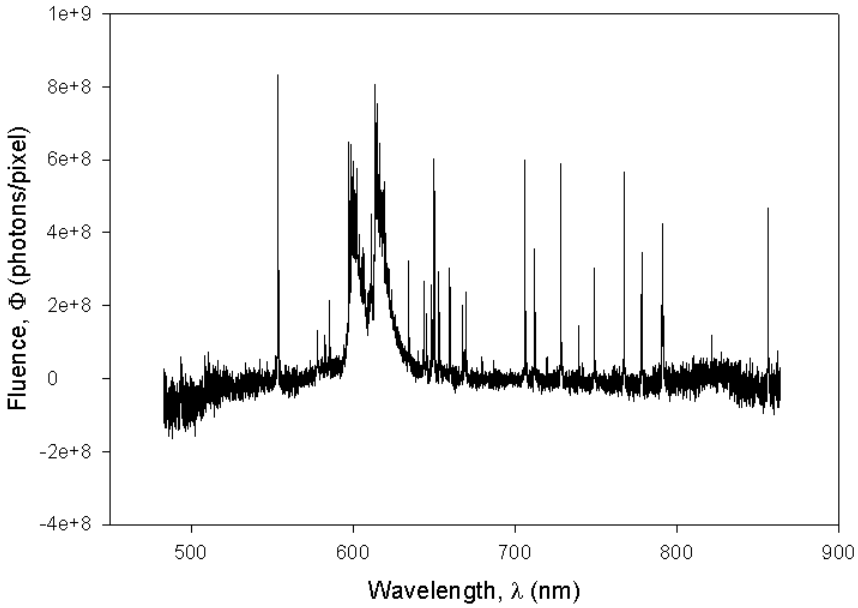

Figure D.8: Calibrated spectrum–150 mTorr, 55.0 mm.

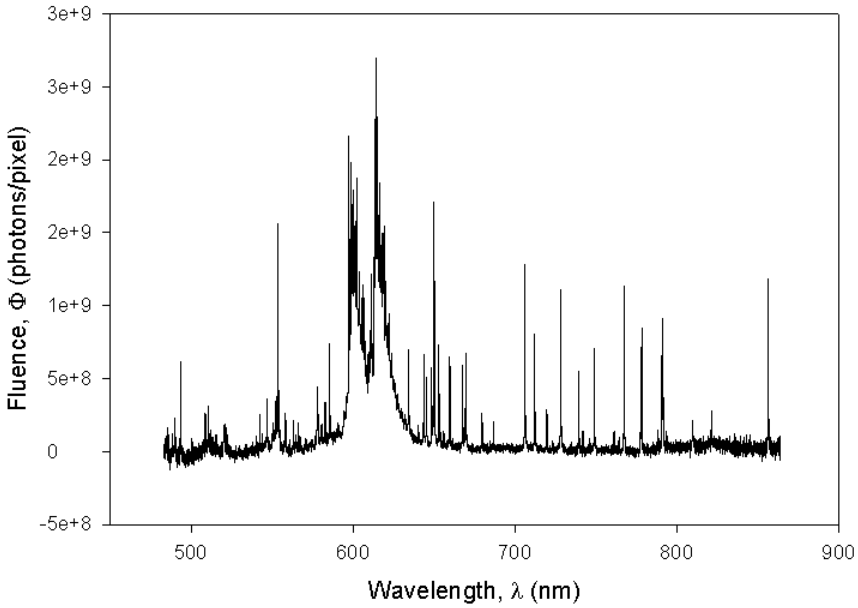

Figure D.9: Calibrated spectrum–400 mTorr, 31.4 mm.

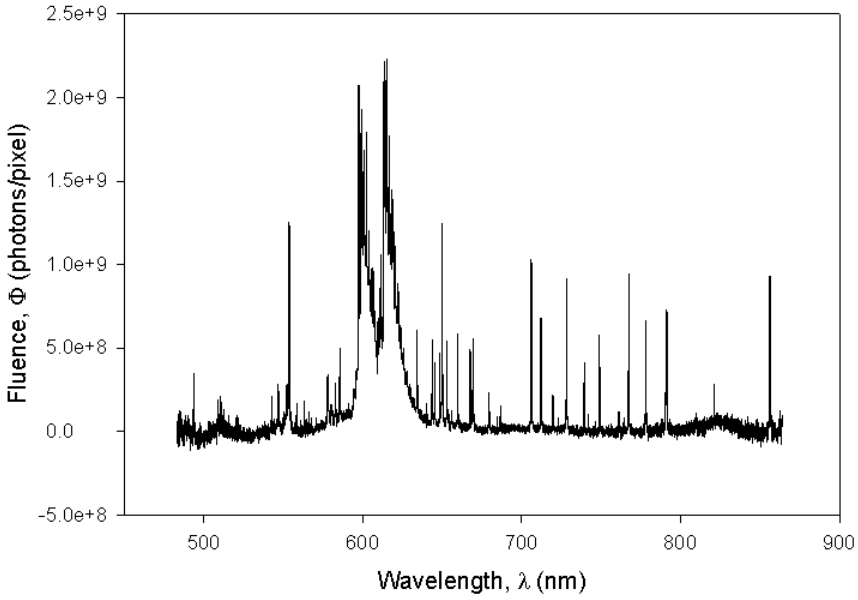

Figure D.10: Calibrated spectrum–400 mTorr, 36.0 mm.

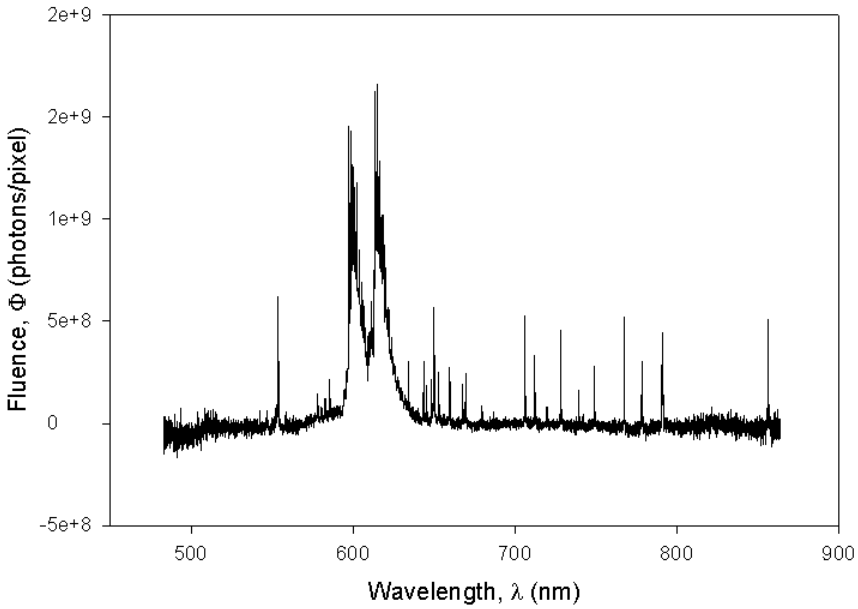

Figure D.11: Calibrated spectrum–400 mTorr, 45.7 mm.

D.2 Emission Line Data

The emission line fluences presented in this section were measured by fitting gaussian lineshapes to the calibrated spectra using Peakfit^{TM}software. The tables below include the center wavelength of the OMA bandpass, the center wavelength of the emission line, the line fluence (Φ_{line}) and its error (σ_Φ), and the assigned emission source. Φ_{line} is defined as the integral of gaussian lineshape $\Phi(\lambda)$:

$$\Phi_{line} = \int_0^{+\infty} \Phi(\lambda)\, d\lambda \tag{D.2}$$

and the σ_Φ is the error associated with fitting the lineshape to the measured spectrum.

Table D.1: Emission Line Data–50 mTorr, 31.4 mm

window (nm)	λ (nm)	Φ_{line} (photons)	σ_Φ (photons)	Source
500	493.4076	1.68E+08	5.23E+06	Ba II
500	508.7423	2.30E+07	4.37E+06	Y II
500	510.5537	8.98E+07	4.57E+06	Cu I

Table D.1: Emission Line Data–50 mTorr, 31.4 mm – Continued

window (nm)	λ (nm)	Φ_{line} (photons)	σ_Φ (photons)	Source
525	508.7423	2.86E+07	2.88E+06	Y II
525	510.5537	1.01E+08	3.33E+06	Cu I
525	515.3231	1.46E+07	2.85E+06	Cu I
525	520.0410	2.19E+07	2.85E+06	Y II
525	520.5715	2.98E+07	2.86E+06	Y II
525	521.8198	3.06E+07	3.36E+06	Cu I
525	522.0100	1.75E+07	3.32E+06	Cu I
550	542.4554	6.01E+07	7.28E+06	Ba I
550	546.6467	1.25E+08	7.28E+06	Y I
550	551.9042	1.01E+08	7.19E+06	Ba I
550	552.7530	1.39E+08	7.20E+06	Y I
550	553.5480	6.52E+08	8.49E+06	Ba I
550	558.1832	8.78E+07	7.11E+06	Y I
550	563.0130	5.45E+07	7.04E+06	Y I
575	560.6317	1.43E+07	3.00E+06	Y I
575	563.0130	6.68E+07	3.03E+06	Y I
575	564.4661	2.01E+07	3.48E+06	Y I
575	570.0237	1.11E+07	2.95E+06	Cu I
575	577.7618	1.22E+08	3.12E+06	Ba I
575	578.2130	5.65E+07	2.98E+06	Cu I
575	580.0225	3.06E+07	2.93E+06	Ba I
575	580.5678	3.11E+07	2.93E+06	Ba I
575	582.6273	9.29E+07	2.98E+06	Ba I
575	585.3668	1.790E+08	3.21E+06	Ba II
600	585.3668	1.99E+08	5.28E+06	Ba II
600	590.7633	1.61E+07	5.09E+06	Ba I

Table D.1: Emission Line Data–50 mTorr, 31.4 mm – Continued

window (nm)	λ (nm)	Φ_{line} (photons)	σ_Φ (photons)	Source
600	597.1693	1.89E+08	5.16E+06	Ba I
600	599.7084	9.51E+07	5.05E+06	Ba I
600	601.9465	1.40E+08	5.52E+06	Ba I
600	606.3109	1.92E+08	5.09E+06	Ba I
600	611.0779	2.17E+08	6.67E+06	Ba I
600	614.1713	3.15E+08	3.15E+08	Ba II
625	611.0779	2.39E+08	5.85E+06	Ba I
625	614.1713	4.19E+08	6.25E+06	Ba II
625	619.1733	2.37E+08	5.77E+06	Y I
625	622.2603	7.11E+07	5.55E+06	Y I
625	634.1677	1.81E+08	5.54E+06	Ba I
650	640.2025	2.23E+07	7.68E+06	Y I
650	643.5034	3.01E+08	7.94E+06	Y I
650	645.0850	1.54E+08	7.69E+06	Ba I
650	648.2910	2.39E+08	7.76E+06	Ba I
650	649.6896	4.70E+08	1.05E+07	Ba II
650	649.8757	3.43E+08	1.00E+07	Ba I
650	652.7308	2.85E+08	7.78E+06	Ba I
650	659.5323	2.34E+08	7.59E+06	Ba I
675	667.5267	1.75E+08	2.61E+06	Ba I
675	668.7565	8.21E+07	2.43E+06	Y I
675	669.3840	2.00E+08	2.64E+06	Ba I
675	679.3708	7.01E+07	2.39E+06	Y I
675	686.5687	1.96E+07	4.03E+06	Ba I
700	686.5687	2.91E+07	5.87E+06	Ba I
700	705.9938	5.11E+08	6.69E+06	Ba I

Table D.1: Emission Line Data–50 mTorr, 31.4 mm – Continued

window (nm)	λ (nm)	Φ_{line} (photons)	σ_Φ (photons)	Source
700	712.0326	2.29E+08	5.79E+06	Ba I
725	712.0326	2.51E+08	5.17E+06	Ba I
725	719.5232	4.61E+07	4.90E+06	Ba I
725	728.0297	4.69E+08	5.59E+06	Ba I
725	739.2407	8.64E+07	4.75E+06	Ba I
750	739.2407	1.20E+08	2.97E+06	Ba I
750	741.7530	2.91E+07	2.82E+06	Ba I
750	748.8077	2.25E+08	3.26E+06	Ba I
750	761.0480	1.84E+07	2.63E+05	Ba I
775	761.0480	2.57E+07	4.89E+06	Ba I
775	767.2087	4.16E+08	5.44E+06	Ba I
775	778.0479	2.90E+08	5.00E+06	Ba I
800	790.5748	1.80E+08	3.13E+06	Ba I
800	791.1334	2.64E+08	3.33E+06	Ba I
800	793.3124	2.57E+07	2.98E+06	Cu I
800	809.2631	3.92E+07	2.87E+06	Cu I
825	821.0249	6.59E+07	3.00E+06	Ba I
850	856.0000	4.56E+08	6.31E+06	Ba I

Table D.2: Emission Line Data–50 mTorr, 36.0 mm

window (nm)	λ (nm)	Φ_{line} (photons)	σ_Φ (photons)	Source
500	488.3686	3.99E+07	4.60E+06	Y II
500	493.4076	1.70E+08	5.16E+06	Ba II
500	508.7423	3.46E+07	4.37E+06	Y II
500	510.5537	9.96E+07	4.58E+06	Cu I
525	508.7423	2.70E+07	2.48E+06	Y II

Table D.2: Emission Line Data–50 mTorr, 36.0 mm – Continued

window (nm)	λ (nm)	Φ_{line} (photons)	σ_{Φ} (photons)	Source)
525	510.5537	1.18E+08	2.88E+06	Cu I
525	515.3231	2.23E+07	2.47E+06	Cu I
525	520.0410	2.44E+07	2.46E+06	Y II
525	520.5715	3.35E+07	2.48E+06	Y II
525	521.8198	4.07E+07	3.37E+06	Cu I
525	522.0100	2.18E+07	3.32E+06	Cu I
550	542.4554	6.09E+07	7.78E+06	Ba I
550	546.6467	1.41E+08	7.77E+06	Y I
550	551.9042	1.19E+08	7.68E+06	Ba I
550	552.7530	1.70E+08	7.70E+06	Y I
550	553.5480	7.73E+08	9.09E+06	Ba I
550	558.1832	9.92E+07	7.59E+06	Y I
550	563.0130	6.60E+07	7.52E+06	Y I
575	560.6317	1.94E+07	4.05E+06	Y I
575	563.0130	7.92E+07	4.10E+06	Y I
575	564.4661	1.97E+07	5.58E+06	Y I
575	567.5280	1.61E+07	4.47E+06	Y I
575	567.9995	1.08E+07	4.47E+06	Ba I
575	570.0237	1.23E+07	4.00E+06	Cu I
575	577.7618	1.35E+08	4.25E+06	Ba I
575	578.2130	6.57E+07	4.09E+06	Cu I
575	580.0225	4.30E+07	3.97E+06	Ba I
575	580.5678	4.14E+07	3.97E+06	Ba I
575	582.6273	1.17E+08	4.04E+06	Ba I
575	585.3668	2.21E+08	4.37E+06	Ba II
600	585.3668	2.07E+08	5.54E+06	Ba II

Table D.2: Emission Line Data–50 mTorr, 36.0 mm – Continued

window (nm)	λ (nm)	Φ_{line} (photons)	σ_{Φ} (photons)	Source)
600	590.7633	1.46E+07	5.33E+06	Ba I
600	597.1693	2.03E+08	5.42E+06	Ba I
600	599.7084	1.14E+08	5.30E+06	Ba I
600	601.9465	1.55E+08	5.73E+06	Ba I
600	606.3109	1.94E+08	5.33E+06	Ba I
600	611.0779	2.45E+08	5.37E+06	Ba I
600	614.1713	3.37E+08	5.54E+06	Ba II
625	611.0779	2.81E+08	7.70E+06	Ba I
625	614.1713	4.37E+08	8.08E+06	Ba II
625	619.1733	3.34E+08	7.72E+06	Y I
625	622.2603	9.01E+07	7.28E+06	Y I
625	634.1677	2.30E+08	7.30E+06	Ba I
650	640.2025	2.20E+07	8.51E+06	Y I
650	643.5034	3.61E+08	8.90E+06	Y I
650	645.0859	1.65E+08	8.53E+06	Ba I
650	648.2910	2.55E+08	8.61E+06	Ba I
650	649.6896	4.49E+08	1.11E+07	Ba II
650	649.8757	4.04E+08	1.09E+07	Ba I
650	652.7308	2.99E+08	8.62E+06	Ba I
650	659.5323	2.57E+08	8.44E+06	Ba I
675	659.5323	2.91E+08	3.56E+06	Ba I
675	667.5267	2.02E+08	3.34E+06	Ba I
675	668.7565	9.62E+06	3.19E+06	Y I
675	669.3840	2.33E+09	3.37E+06	Ba I
675	670.0635	3.21E+07	3.16E+06	Y I
675	679.3708	8.30E+07	3.14E+06	Y I

Table D.2: Emission Line Data–50 mTorr, 36.0 mm – Continued

window (nm)	λ (nm)	Φ_{line} (photons)	σ_Φ (photons)	Source)
675	686.5687	2.92E+07	3.07E+06	Ba I
700	686.5687	3.46E+07	5.54E+06	Ba I
700	705.9938	6.11E+08	6.41E+06	Ba I
700	712.0326	2.74E+08	5.47E+06	Ba I
725	712.0326	3.39E+08	8.83E+06	Ba I
725	719.5232	6.17E+07	8.39E+06	Ba I
725	728.0297	6.42E+08	9.57E+06	Ba I
725	739.2407	1.20E+08	8.14E+06	Ba I
750	739.2407	1.38E+08	3.51E+06	Ba I
750	741.7530	3.01E+07	3.34E+06	Ba I
750	748.8077	2.69E+08	3.87E+06	Ba I
750	761.0480	2.19E+07	3.20E+06	Ba I
775	761.0480	2.85E+07	5.55E+06	Ba I
775	767.2087	4.79E+08	6.15E+06	Ba I
775	778.0479	3.50E+08	5.70E+06	Ba I
800	790.5748	1.89E+08	3.37E+06	Ba I
800	791.1334	3.19E+08	3.66E+06	Ba I
800	793.3124	2.68E+07	3.22E+06	Cu I
800	809.2631	4.14E+07	3.10E+06	Cu I
825	821.0249	7.19E+07	2.93E+06	Ba I
850	856.0000	5.37E+08	6.85E+06	Ba I

Table D.3: Emission Line Data–50 mTorr, 45.7 mm

window (nm)	λ (nm)	Φ_{line} (photons)	σ_Φ (photons)	Source
500	493.4076	1.24E+08	4.94E+06	Ba II
500	510.5537	7.93E+07	4.41E+06	Cu I

Table D.3: Emission Line Data–50 mTorr, 45.7 mm – Continued

window (nm)	λ (nm)	Φ_{line} (photons)	σ_{Φ} (photons)	Source
525	510.5537	7.54E+07	2.74E+06	Cu I
525	515.3231	9.75E+06	2.27E+06	Cu I
525	521.8198	2.16E+07	2.48E+06	Cu I
525	522.0100	1.04E+07	2.44E+06	Cu I
550	542.4554	2.66E+07	3.55E+06	Ba I
550	546.6467	2.99E+07	3.53E+06	Y I
550	551.9042	3.78E+07	3.51E+06	Ba I
550	552.7530	4.11E+07	3.50E+06	Y I
550	553.5480	2.18E+08	4.16E+06	Ba I
550	558.1832	1.88E+07	3.46E+06	Y I
550	563.0130	1.52E+07	3.43E+06	Y I
575	563.0130	3.95E+07	2.40E+06	Y I
575	577.7618	9.36E+07	2.57E+06	Ba I
575	578.2130	4.31E+07	2.45E+06	Cu I
575	580.0225	1.92E+07	2.37E+06	Ba I
575	580.5678	2.74E+07	2.37E+06	Ba I
575	582.6273	7.61E+07	2.40E+06	Ba I
575	585.3668	1.30E+08	2.56E+06	Ba II
600	585.3668	1.31E+08	4.51E+06	Ba II
600	590.7633	1.35E+07	4.35E+06	Ba I
600	597.1693	1.55E+08	4.46E+06	Ba I
600	599.7084	7.20E+07	4.33E+06	Ba I
600	601.9465	1.07E+08	4.81E+06	Ba I
600	606.3109	1.24E+08	4.34E+06	Ba I
600	611.0779	1.68E+08	4.39E+06	Ba I
600	614.1713	2.21E+07	4.50E+06	Ba II

Table D.3: Emission Line Data–50 mTorr, 45.7 mm – Continued

window (nm)	λ (nm)	Φ_{line} (photons)	σ_Φ (photons)	Source
625	611.0779	1.52E+08	3.73E+06	Ba I
625	614.1713	2.24E+08	3.88E+06	Ba II
625	619.1733	2.18E+08	3.82E+06	Y I
625	622.2603	5.91E+07	3.54E+06	Y I
625	634.1677	1.26E+08	3.54E+06	Ba I
650	640.2025	2.02E+07	6.37E+06	Y I
650	643.5034	3.01E+08	6.73E+06	Y I
650	645.0850	1.13E+08	6.37E+06	Ba I
650	648.2910	1.94E+08	6.45E+06	Ba I
650	649.6896	3.32E+08	8.59E+06	Ba II
650	649.8757	2.86E+08	8.41E+06	Ba I
650	652.7308	2.05E+08	6.41E+06	Ba I
650	659.5323	1.72E+08	6.28E+06	Ba I
675	667.5267	1.38E+08	3.10E+06	Ba I
675	668.7565	7.64E+07	2.92E+06	Y I
675	669.3840	1.58E+08	3.14E+06	Ba I
675	679.3708	6.29E+07	2.87E+06	Y I
675	686.5687	2.23E+07	2.79E+06	Ba I
700	686.5687	1.99E+07	4.73E+06	Ba I
700	705.9938	4.47E+08	5.42E+06	Ba I
700	712.0326	1.90E+08	4.66E+06	Ba I
725	712.0326	2.14E+08	5.29E+06	Ba I
725	719.5232	3.59E+07	5.75E+06	Ba I
725	728.0297	4.21E+08	5.16E+06	Ba I
725	739.2407	7.78E+07	6.31E+06	Ba I
750	739.2407	8.11E+07	2.64E+06	Ba I

Table D.3: Emission Line Data–50 mTorr, 45.7 mm – Continued

window (nm)	λ (nm)	Φ_{line} (photons)	σ_Φ (photons)	Source
750	741.7530	2.28E+07	2.54E+06	Ba I
750	748.8077	1.97E+08	2.98E+06	Ba I
750	761.0480	1.33E+07	2.43E+06	Ba I
775	761.0480	2.20E+07	3.83E+06	Ba I
775	767.2087	3.38E+08	4.37E+06	Ba I
775	778.0479	2.20E+08	4.25E+06	Ba I
800	790.5748	1.29E+08	2.78E+06	Ba I
800	791.1334	2.75E+08	3.12E+06	Ba I
800	793.3124	1.94E+07	2.69E+06	Cu I
800	809.2631	2.77E+07	2.59E+06	Cu I
825	821.0249	4.61E+07	2.31E+06	Ba I
850	856.0000	3.83E+08	5.68E+06	Ba I

Table D.4: Emission Line Data–50 mTorr, 55.0 mm

window (nm)	λ (nm)	Φ_{line} (photons)	σ_Φ (photons)	Source
500	493.4076	1.12E+08	5.10E+06	Ba II
500	510.5537	8.65E+07	4.70E+06	Cu I
525	510.5537	6.36E+07	2.93E+06	Cu I
525	515.3231	1.62E+07	2.51E+06	Cu I
525	521.8198	2.20E+07	2.64E+06	Cu I
525	522.0100	1.71E+07	2.61E+06	Cu I
550	542.4554	3.21E+07	6.40E+06	Ba I
550	546.6467	6.17E+07	6.37E+06	Y I
550	551.9042	6.24E+07	6.31E+06	Ba I
550	552.7530	8.48E+07	6.31E+06	Y I
550	553.5480	7.37E+08	7.63E+06	Ba I

Table D.4: Emission Line Data–50 mTorr, 55.0 mm – Continued

window (nm)	λ (nm)	Φ_{line} (photons)	σ_{Φ} (photons)	Source
550	558.1832	3.61E+07	6.24E+06	Y I
550	563.0130	1.88E+07	6.19E+06	Y I
575	563.0130	3.05E+07	2.19E+06	Y I
575	577.7618	8.25E+07	2.31E+06	Ba I
575	578.2130	3.85E+07	2.20E+06	Cu I
575	580.0225	2.60E+07	2.14E+06	Ba I
575	580.5678	2.53E+07	2.14E+06	Ba I
575	582.6273	7.78E+07	2.20E+06	Ba I
575	585.3668	1.16E+08	2.32E+06	Ba II
600	585.3668	1.04E+08	4.14E+06	Ba II
600	597.1693	1.60E+08	4.15E+06	Ba I
600	599.7084	5.12E+07	3.98E+06	Ba I
600	601.9465	9.70E+07	4.45E+06	Ba I
600	606.3109	1.02E+08	3.99E+06	Ba I
600	611.0779	1.47E+08	4.08E+06	Ba I
600	614.1713	2.09E+08	4.16E+06	Ba II
625	611.0779	1.46E+08	3.90E+06	Ba I
625	614.1713	2.30E+08	4.56E+06	Ba II
625	619.1733	2.37E+08	4.07E+06	Y I
625	622.2603	6.33E+07	4.35E+06	Y I
625	634.1677	1.27E+08	3.72E+06	Ba I
650	640.2025	1.45E+07	5.58E+06	Y I
650	643.5034	2.96E+08	5.95E+06	Y I
650	645.0850	8.84E+07	5.57E+06	Ba I
650	648.2910	1.78E+08	5.65E+06	Ba I
650	649.6896	2.82E+08	7.42E+06	Ba II

Table D.4: Emission Line Data–50 mTorr, 55.0 mm – Continued

window (nm)	λ (nm)	Φ_{line} (photons)	σ_{Φ} (photons)	Source
650	649.8757	2.64E+08	7.35E+06	Ba I
650	652.7308	1.79E+08	5.61E+06	Ba I
650	659.5323	1.52E+08	5.49E+06	Ba I
675	659.5323	1.75E+08	2.56E+06	Ba I
675	667.5267	1.22E+08	2.40E+06	Ba I
675	668.7565	7.34E+07	2.31E+06	Y I
675	669.3840	1.45E+08	2.43E+06	Ba I
675	679.3708	6.56E+07	2.28E+06	Y I
675	686.5687	1.61E+07	2.21E+06	Ba I
700	686.5687	1.84E+07	5.26E+06	Ba I
700	705.9938	4.68E+08	6.03E+06	Ba I
700	712.0326	1.89E+08	5.15E+06	Ba I
725	712.0326	2.10E+08	4.69E+06	Ba I
725	719.5232	2.38E+07	4.46E+06	Ba I
725	728.0297	4.25E+08	5.14E+06	Ba I
725	739.2407	4.59E+07	4.31E+06	Ba I
750	739.2407	7.04E+07	2.43E+06	Ba I
750	741.7530	2.32E+07	2.35E+06	Ba I
750	748.8077	1.89E+08	2.76E+06	Ba I
750	761.0480	1.29E+07	2.25E+06	Ba I
775	761.0480	1.82E+07	3.94E+06	Ba I
775	767.2087	3.37E+08	4.49E+06	Ba I
775	778.0479	2.20E+08	4.08E+06	Ba I
800	790.5748	1.08E+08	3.16E+06	Ba I
800	791.1334	3.17E+08	3.66E+06	Ba I
800	793.3124	1.01E+07	3.10E+06	Cu I

Table D.4: Emission Line Data–50 mTorr, 55.0 mm – Continued

window (nm)	λ (nm)	Φ_{line} (photons)	σ_Φ (photons)	Source
800	809.2631	2.30E+07	2.98E+06	Cu I
825	821.0249	6.01E+07	2.89E+06	Ba I
850	856.0000	3.76E+08	5.13E+06	Ba I

Table D.5: Emission Line Data–150 mTorr, 31.4 mm

window (nm)	λ (nm)	Φ_{line} (photons)	σ_Φ (photons)	Source
500	488.3686	4.37E+07	6.65E+06	Y II
500	493.4076	1.91E+08	7.21E+06	Ba II
500	508.7423	4.08E+07	6.32E+06	Y II
500	510.5537	1.71E+08	6.87E+06	Cu I
525	508.7423	3.84E+07	3.13E+06	Y II
525	510.5537	1.74E+08	3.65E+06	Cu I
525	515.3231	3.50E+07	3.12E+06	Cu I
525	520.0410	3.61E+07	3.11E+06	Y II
525	520.5715	5.22E+07	3.13E+06	Y II
525	521.8198	4.75E+07	5.54E+06	Cu I
525	522.0100	2.70E+07	5.51E+06	Cu I
550	542.4554	1.00E+08	8.26E+06	Ba I
550	546.6467	1.77E+08	8.22E+06	Y I
550	551.9042	1.53E+08	8.17E+06	Ba I
550	552.7530	1.86E+08	8.10E+06	Y I
550	553.5480	7.57E+08	9.56E+06	Ba I
550	558.1832	1.20E+08	8.37E+06	Y I
550	560.6317	1.92E+07	8.00E+06	Y I
550	563.0130	8.13E+07	1.12E+07	Y I
575	560.6317	2.51E+07	4.48E+06	Y I

Table D.5: Emission Line Data–150 mTorr, 31.4 mm – Continued

window (nm)	λ (nm)	Φ_{line} (photons)	σ_Φ (photons)	Source
575	563.0130	1.09E+08	1.12E+07	Y I
575	564.4661	4.62E+07	5.18E+06	Y I
575	567.5280	3.06E+07	4.47E+06	Y I
575	570.0237	1.35E+07	4.41E+06	Cu I
575	577.7618	1.67E+08	4.66E+06	Ba I
575	578.2130	1.03E+08	4.51E+06	Cu I
575	580.0225	6.66E+07	4.38E+06	Ba I
575	580.5678	5.91E+07	4.37E+06	Ba I
575	582.6273	1.55E+08	4.49E+06	Ba I
575	585.3668	2.29E+08	4.69E+06	Ba II
600	585.3668	2.31E+08	7.64E+06	Ba II
600	590.7633	3.54E+07	7.42E+06	Ba I
600	597.1693	3.91E+08	7.76E+06	Ba I
600	599.7084	1.53E+08	7.38E+06	Ba I
600	601.9465	2.60E+08	8.06E+06	Ba I
600	606.3109	2.45E+08	7.40E+06	Ba I
600	611.0779	3.11E+08	7.44E+06	Ba I
600	614.1713	3.37E+08	7.45E+06	Ba II
625	611.0779	2.86E+08	6.91E+06	Ba I
625	614.1713	3.45E+08	7.03E+06	Ba II
625	619.1733	2.53E+08	6.75E+06	Y I
625	622.2603	9.18E+07	6.86E+06	Y I
625	634.1677	2.56E+08	6.59E+06	Ba I
625	640.2025	3.12E+07	6.24E+06	Y I
650	640.2025	3.13E+07	8.80E+06	Y I
650	643.5034	3.17E+08	9.05E+06	Y I

Table D.5: Emission Line Data–150 mTorr, 31.4 mm – Continued

window (nm)	λ (nm)	Φ_{line} (photons)	σ_Φ (photons)	Source
650	645.0850	2.25E+08	8.87E+06	Ba I
650	648.2910	2.96E+08	8.93E+06	Ba I
650	649.6896	4.24E+08	1.15E+07	Ba II
650	649.8757	4.23E+08	1.15E+07	Ba I
650	652.7308	3.50E+08	8.97E+06	Ba I
650	659.5323	3.09E+08	8.77E+06	Ba I
675	659.5323	3.73E+08	4.64E+06	Ba I
675	667.5267	2.96E+08	4.42E+06	Ba I
675	668.7565	1.14E+08	4.18E+06	Y I
675	669.3840	3.31E+08	4.45E+06	Ba I
675	670.0635	5.17E+07	4.15E+06	Y I
675	679.3708	1.04E+08	4.12E+06	Y I
675	686.5687	5.54E+07	4.03E+06	Ba I
700	686.5687	5.37E+07	6.20E+06	Ba I
700	705.9938	5.37E+08	6.94E+06	Ba I
700	712.0326	3.13E+08	6.23E+06	Ba I
725	712.0326	3.46E+08	6.32E+06	Ba I
725	719.5232	8.86E+07	5.92E+06	Ba I
725	728.0297	5.18E+08	6.60E+06	Ba I
725	739.2407	1.66E+08	5.79E+06	Ba I
750	739.2407	1.91E+08	3.92E+06	Ba I
750	741.7530	4.61E+07	3.68E+06	Ba I
750	748.8077	3.10E+08	4.20E+06	Ba I
750	761.0480	3.74E+07	3.52E+06	Ba I
775	761.0480	5.03E+07	5.10E+06	Ba I
775	767.2087	4.65E+08	5.77E+06	Ba I

Table D.5: Emission Line Data–150 mTorr, 31.4 mm – Continued

window (nm)	λ (nm)	Φ_{line} (photons)	σ_Φ (photons)	Source
775	778.0479	3.59E+08	5.51E+06	Ba I
800	790.5748	2.72E+08	3.78E+06	Ba I
800	791.1334	3.03E+08	3.85E+06	Ba I
800	793.3124	5.48E+07	3.52E+06	Cu I
800	809.2631	7.49E+07	3.39E+06	Cu I
825	821.0249	1.07E+08	2.73E+06	Ba I
850	856.0000	5.22E+08	6.06E+06	Ba I

Table D.6: Emission Line Data–150 mTorr, 36.0 mm

window (nm)	λ (nm)	Φ_{line} (photons)	σ_Φ (photons)	Source
500	493.4076	1.94E+08	6.09E+06	Ba II
500	508.7423	4.10E+07	5.28E+06	Y II
500	510.5537	1.63E+08	5.72E+06	Cu I
525	508.7423	3.13E+07	2.77E+06	Y II
525	510.5537	1.46E+08	3.21E+06	Cu I
525	515.3231	4.02E+07	2.78E+06	Cu I
525	520.0410	3.10E+07	2.76E+06	Y II
525	520.5715	3.94E+07	2.76E+06	Y II
525	521.8198	4.35E+07	3.53E+06	Cu I
525	522.0100	2.71E+07	3.49E+06	Cu I
550	542.4554	7.98E+07	7.32E+06	Ba I
550	546.6467	1.59E+08	7.28E+06	Y I
550	551.9042	1.33E+08	7.24E+06	Ba I
550	552.7530	1.69E+08	7.17E+06	Y I
550	553.548	7.60E+08	8.53E+06	Ba I
550	558.1832	1.00E+08	7.48E+06	Y I

Table D.6: Emission Line Data–150 mTorr, 36.0 mm – Continued

window (nm)	λ (nm)	Φ_{line} (photons)	σ_{Φ} (photons)	Source
550	563.0130	7.95E+07	7.21E+06	Y I
575	560.6317	2.46E+07	4.04E+06	Y I
575	563.0130	9.39E+07	4.06E+06	Y I
575	564.4661	3.41E+07	4.68E+06	Y I
575	567.5280	2.65E+07	4.17E+06	Y I
575	567.9995	1.44E+07	4.14E+06	Ba I
575	570.0237	1.27E+07	3.99E+06	Cu I
575	577.7618	1.62E+08	4.19E+06	Ba I
575	578.2130	1.03E+08	4.06E+06	Cu I
575	580.0225	5.76E+07	3.95E+06	Ba I
575	580.5678	6.16E+07	3.95E+06	Ba I
575	582.6273	1.50E+08	4.05E+06	Ba I
575	585.3668	2.19E+08	4.23E+06	Ba II
600	585.3668	1.39E+08	1.03E+07	Ba II
600	590.7633	2.33E+07	1.02E+07	Ba I
600	597.1693	6.33E+08	1.08E+07	Ba I
600	599.7084	9.67E+07	1.00E+07	Ba I
600	601.9465	3.19E+08	1.02E+07	Ba I
600	606.3109	1.23E+08	9.94E+06	Ba I
600	611.0779	1.89E+08	1.00E+07	Ba I
600	614.1713	2.60E+08	9.88E+06	Ba II
625	611.0779	3.00E+08	8.13E+06	Ba I
625	614.1713	3.57E+08	8.23E+06	Ba II
625	619.1733	2.91E+08	8.00E+06	Y I
625	622.2603	1.04E+08	8.07E+06	Y I
625	634.1677	2.61E+08	7.75E+06	Ba I

Table D.6: Emission Line Data–150 mTorr, 36.0 mm – Continued

window (nm)	λ (nm)	Φ_{line} (photons)	σ_{Φ} (photons)	Source
625	640.2025	2.44E+07	7.40E+06	Y I
650	640.2025	3.22E+07	8.56E+06	Y I
650	643.5034	3.17E+08	8.81E+06	Y I
650	645.0850	2.24E+08	8.63E+06	Ba I
650	648.2910	2.95E+08	8.69E+06	Ba I
650	649.6896	4.22E+08	1.12E+07	Ba II
650	649.8757	4.22E+08	1.12E+07	Ba I
650	652.7308	3.48E+08	8.72E+06	Ba I
650	659.5323	3.06E+08	8.54E+06	Ba I
675	659.5323	3.19E+08	4.00E+06	Ba I
675	667.5267	2.61E+08	3.83E+06	Ba I
675	668.7565	1.10E+08	3.62E+06	Y I
675	669.3840	2.93E+08	3.86E+06	Ba I
675	670.0635	4.27E+07	3.60E+06	Y I
675	679.3708	9.03E+07	3.56E+06	Y I
675	686.5687	4.80E+07	3.49E+06	Ba I
700	686.5687	5.68E+07	6.59E+06	Ba I
700	705.9938	5.75E+08	7.39E+06	Ba I
700	712.0326	3.33E+08	6.62E+06	Ba I
725	712.0326	3.84E+08	7.03E+06	Ba I
725	719.5232	9.42E+07	6.59E+06	Ba I
725	728.0297	5.81E+08	7.36E+06	Ba I
725	739.2407	1.76E+08	6.43E+06	Ba I
750	739.2407	2.12E+08	4.34E+06	Ba I
750	741.7530	6.27E+07	4.09E+06	Ba I
750	748.8077	3.49E+08	4.67E+06	Ba I

Table D.6: Emission Line Data–150 mTorr, 36.0 mm – Continued

window (nm)	λ (nm)	Φ_{line} (photons)	σ_Φ (photons)	Source
750	761.0480	3.53E+07	3.91E+06	Ba I
775	761.0480	5.04E+07	5.81E+06	Ba I
775	767.2087	5.45E+08	6.52E+06	Ba I
775	778.0479	4.03E+08	6.04E+06	Ba I
800	790.5748	2.88E+08	3.97E+06	Ba I
800	791.1334	3.58E+08	4.12E+06	Ba I
800	793.3124	5.25E+07	3.73E+06	Cu I
800	809.2631	8.33E+07	3.60E+06	Cu I
825	821.0249	1.07E+08	3.44E+06	Ba I
850	856.0000	5.29E+08	6.83E+06	Ba I

Table D.7: Emission Line Data–150 mTorr, 45.7 mm

window (nm)	λ (nm)	Φ_{line} (photons)	σ_Φ (photons)	Source
500	493.4076	8.32E+07	4.76E+06	Ba II
500	510.5537	6.98E+07	4.47E+06	Cu I
525	510.5537	6.87E+07	2.79E+06	Cu I
525	515.3231	1.25E+07	2.32E+06	Cu I
525	521.8198	1.52E+07	2.33E+06	Cu I
550	542.4554	4.11E+07	4.66E+06	Ba I
550	546.6467	5.54E+07	4.61E+06	Y I
550	551.9042	6.54E+07	4.60E+06	Ba I
550	552.7530	6.55E+07	4.54E+06	Y I
550	553.5480	4.50E+08	5.50E+06	Ba I
550	558.1832	3.44E+07	4.58E+06	Y I
550	563.0130	3.29E+07	4.59E+06	Y I
575	563.0130	3.71E+07	2.91E+06	Y I

Table D.7: Emission Line Data–150 mTorr, 45.7 mm – Continued

window (nm)	λ (nm)	Φ_{line} (photons)	σ_{Φ} (photons)	Source
575	577.7618	8.74E+07	3.09E+06	Ba I
575	578.2130	4.58E+07	2.96E+06	Cu I
575	580.0225	3.37E+07	2.87E+06	Ba I
575	580.5678	4.03E+07	2.88E+06	Ba I
575	582.6273	8.07E+07	2.94E+06	Ba I
575	585.3668	1.19E+08	3.08E+06	Ba II
600	585.3668	1.16E+08	5.60E+06	Ba II
600	590.7633	2.05E+07	5.50E+06	Ba I
600	597.1693	3.42E+08	5.84E+06	Ba I
600	599.7084	6.78E+07	5.44E+06	Ba I
600	601.9465	2.04E+08	5.54E+06	Ba I
600	606.3109	1.27E+08	5.41E+06	Ba I
600	611.0779	1.61E+08	5.49E+06	Ba I
600	614.1713	1.58E+08	5.36E+06	Ba II
625	611.0779	1.68E+08	6.00E+06	Ba I
625	614.1713	1.61E+08	5.96E+06	Ba II
625	619.1733	1.75E+08	5.94E+06	Y I
625	622.2603	6.22E+07	5.94E+06	Y I
625	634.1677	1.37E+08	5.70E+06	Ba I
625	640.2025	1.17E+07	5.49E+06	Y I
650	640.2025	1.63E+07	5.06E+06	Y I
650	643.5034	1.87E+08	5.22E+06	Y I
650	645.0850	1.18E+08	5.09E+06	Ba I
650	648.2910	1.64E+08	5.13E+06	Ba I
650	649.6896	2.21E+08	6.83E+06	Ba II
650	649.8757	2.53E+08	6.93E+06	Ba I

Table D.7: Emission Line Data–150 mTorr, 45.7 mm – Continued

window (nm)	λ (nm)	Φ_{line} (photons)	σ_{Φ} (photons)	Source
650	652.7308	1.92E+08	5.14E+06	Ba I
650	659.5323	1.72E+08	5.04E+06	Ba I
675	659.5323	1.80E+08	2.94E+06	Ba I
675	667.5267	1.48E+08	2.82E+06	Ba I
675	668.7565	6.33E+07	2.67E+06	Y I
675	669.3840	1.63E+08	2.84E+06	Ba I
675	679.3708	4.99E+07	2.62E+06	Y I
675	686.5687	3.01E+07	2.57E+06	Ba I
700	686.5687	3.28E+06	4.19E+06	Ba I
700	705.9938	3.52E+08	4.72E+06	Ba I
700	712.0326	1.93E+08	4.19E+06	Ba I
725	712.0326	2.05E+08	3.77E+06	Ba I
725	719.5232	2.22E+08	3.24E+06	Ba I
725	728.0297	3.13E+08	3.96E+06	Ba I
725	739.2407	8.12E+07	3.44E+06	Ba I
750	739.2407	1.04E+08	2.46E+06	Ba I
750	741.7530	3.28E+07	2.33E+06	Ba I
750	748.8077	1.84E+08	2.67E+06	Ba I
750	761.0480	1.52E+07	2.22E+06	Ba I
775	761.0480	2.47E+07	3.51E+06	Ba I
775	767.2087	2.97E+08	3.97E+06	Ba I
775	778.0479	2.13E+08	3.66E+06	Ba I
800	790.5748	1.41E+08	3.01E+06	Ba I
800	791.1334	2.22E+08	3.24E+06	Ba I
800	793.3124	1.75E+07	2.87E+06	Cu I
800	809.2631	2.25E+07	2.76E+06	Cu I

Table D.7: Emission Line Data–150 mTorr, 45.7 mm – Continued

window (nm)	λ (nm)	Φ_{line} (photons)	σ_Φ (photons)	Source
825	821.0249	5.74E+07	2.59E+06	Ba I
850	856.0000	3.32E+08	5.04E+06	Ba I

Table D.8: Emission Line Data–150 mTorr, 55.0 mm

window (nm)	λ (nm)	Φ_{line} (photons)	σ_Φ (photons)	Source
500	493.4076	5.22E+07	3.86E+06	Ba II
500	510.5537	2.71E+07	3.33E+06	Cu I
525	510.5537	4.04E+07	2.68E+06	Cu I
550	542.4554	1.32E+07	3.53E+06	Ba I
550	546.6467	2.17E+07	3.48E+06	Y I
550	551.9042	3.02E+07	3.48E+06	Ba I
550	552.7530	2.72E+07	3.43E+06	Y I
550	553.5480	2.90E+08	4.21E+06	Ba I
550	558.1832	1.38E+07	3.43E+06	Y I
575	577.7618	3.92E+07	1.84E+06	Ba I
575	578.2130	1.45E+07	1.82E+06	Cu I
575	580.0225	1.17E+07	1.61E+06	Ba I
575	580.5678	1.61E+07	1.62E+06	Ba I
575	582.6273	3.24E+07	1.66E+06	Ba I
575	585.3668	5.53E+07	1.78E+06	Ba II
600	585.3668	6.04E+07	3.57E+06	Ba II
600	590.7633	1.29E+07	3.52E+06	Ba I
600	597.1693	2.03E+08	3.72E+06	Ba I
600	599.7084	3.59E+07	3.47E+06	Ba I
600	601.9465	1.13E+08	3.52E+06	Ba I
600	606.3109	6.23E+07	3.45E+06	Ba I

Table D.8: Emission Line Data–150 mTorr, 55.0 mm – Continued

window (nm)	λ (nm)	Φ_{line} (photons)	σ_{Φ} (photons)	Source
600	611.0779	7.45E+07	3.43E+06	Ba I
600	614.1713	6.48E+07	3.40E+06	Ba II
625	611.0779	8.27E+07	3.41E+06	Ba I
625	614.1713	8.12E+07	3.40E+06	Ba II
625	619.1733	8.11E+07	3.36E+06	Y I
625	622.2603	2.24E+07	3.49E+06	Y I
625	634.1677	6.75E+07	3.25E+06	Ba I
650	640.2025	1.10E+07	3.16E+06	Y I
650	643.5034	8.84E+07	3.23E+06	Y I
650	645.0850	5.98E+07	3.17E+06	Ba I
650	649.6896	1.12E+08	4.42E+06	Ba II
650	649.8757	1.59E+08	4.59E+06	Ba I
650	652.7308	1.06E+08	3.21E+06	Ba I
650	659.5323	8.78E+07	3.13E+06	Ba I
675	659.5323	9.82E+07	1.73E+06	Ba I
675	667.5267	7.44E+07	1.63E+06	Ba I
675	668.7565	2.60E+07	1.53E+06	Y I
675	669.3840	8.68E+07	1.65E+06	Ba I
675	679.3708	2.35E+07	1.51E+06	Y I
675	686.5687	1.14E+07	1.48E+06	Ba I
700	686.5687	1.23E+07	2.38E+06	Ba I
700	705.9938	2.00E+08	2.71E+06	Ba I
700	712.0326	9.54E+07	2.36E+06	Ba I
725	712.0326	1.10E+08	2.65E+06	Ba I
725	719.5232	1.81E+07	2.49E+06	Ba I
725	728.0297	1.83E+08	2.82E+06	Ba I

Table D.8: Emission Line Data–150 mTorr, 55.0 mm – Continued

window (nm)	λ (nm)	Φ_{line} (photons)	σ_Φ (photons)	Source
725	739.2407	3.40E+07	2.41E+06	Ba I
750	739.2407	5.08E+07	1.98E+06	Ba I
750	741.7530	1.49E+07	1.89E+06	Ba I
750	748.8077	1.03E+08	2.19E+06	Ba I
775	761.0480	1.88E+07	2.61E+06	Ba I
775	767.2087	1.69E+08	2.98E+06	Ba I
775	778.0479	1.11E+08	2.70E+06	Ba I
800	790.5748	7.66E+07	2.45E+06	Ba I
800	791.1334	1.36E+08	2.69E+06	Ba I
800	809.2631	1.26E+07	2.28E+06	Cu I
825	821.0249	1.61E+07	2.24E+06	Ba I
850	856.0000	1.70E+08	3.56E+06	Ba I

Table D.9: Emission Line Data–400 mTorr, 31.4 mm

window (nm)	λ (nm)	Φ_{line} (photons)	σ_Φ (photons)	Source
500	488.3686	6.95E+07	6.45E+06	Y II
500	493.4076	2.70E+08	5.78E+06	Ba II
500	508.7423	7.36E+07	6.14E+06	Y II
500	510.5537	9.66E+07	6.18E+06	Cu I
525	508.7423	7.34E+07	4.17E+06	Y II
525	510.5537	1.04E+08	4.27E+06	Cu I
525	515.3231	4.25E+07	4.08E+06	Cu I
525	520.0410	8.32E+07	4.17E+06	Y II
525	520.5715	8.94E+07	4.20E+06	Y II
525	521.8198	7.92E+07	4.17E+06	Cu I
550	542.4554	9.32E+07	7.72E+06	Ba I

Table D.9: Emission Line Data–400 mTorr, 31.4 mm – Continued

window (nm)	λ (nm)	Φ_{line} (photons)	σ_Φ (photons)	Source
550	546.6467	1.46E+08	7.67E+06	Y I
550	551.9042	1.46E+08	7.65E+06	Ba I
550	552.7530	1.54E+08	7.54E+06	Y I
550	553.5480	5.61E+08	8.72E+06	Ba I
550	558.1832	9.82E+07	7.53E+06	Y I
550	560.6317	1.74E+07	7.47E+06	Y I
550	563.0130	7.96E+07	7.59E+06	Y I
575	560.6317	2.89E+07	4.95E+06	Y I
575	563.0130	8.90E+07	7.59E+06	Y I
575	564.4661	4.03E+07	6.03E+06	Y I
575	567.5280	3.94E+07	4.95E+06	Y I
575	570.0237	1.83E+07	4.88E+06	Cu I
575	577.7618	1.60E+08	5.22E+06	Ba I
575	578.2130	8.55E+07	5.02E+06	Cu I
575	580.0225	5.89E+07	4.87E+06	Ba I
575	580.5678	5.74E+07	4.87E+06	Ba I
575	582.6273	1.22E+08	4.92E+06	Ba I
575	585.3668	2.12E+08	5.19E+06	Ba II
600	585.3668	2.04E+08	5.99E+06	Ba II
600	590.7633	1.78E+07	5.79E+06	Ba I
600	597.1693	1.92E+08	5.85E+06	Ba I
600	599.7084	1.22E+08	5.75E+06	Ba I
600	601.9465	1.46E+08	6.36E+06	Ba I
600	606.3109	1.98E+08	5.77E+06	Ba I
600	611.0779	2.34E+08	5.83E+06	Ba I
600	614.1713	4.19E+08	6.14E+06	Ba II

Table D.9: Emission Line Data–400 mTorr, 31.4 mm – Continued

window (nm)	λ (nm)	Φ_{line} (photons)	σ_Φ (photons)	Source
625	611.0779	2.30E+08	1.15E+07	Ba I
625	614.1713	5.28E+08	1.17E+07	Ba II
625	619.1733	2.30E+08	1.12E+07	Y I
625	622.2603	1.12E+08	1.30E+07	Y I
625	634.1677	1.76E+08	1.08E+07	Ba I
650	640.2025	3.46E+07	7.34E+06	Y I
650	643.5034	2.08E+08	7.48E+06	Y I
650	645.0850	1.47E+08	7.36E+06	Ba I
650	648.2910	1.85E+08	7.38E+06	Ba I
650	649.6896	3.31E+08	9.97E+06	Ba II
650	649.8757	4.13E+08	1.03E+07	Ba I
650	652.7308	2.35E+08	7.41E+06	Ba I
650	659.5323	1.99E+08	7.25E+06	Ba I
675	659.5323	2.03E+08	3.28E+06	Ba I
675	667.5267	1.85E+08	3.20E+06	Ba I
675	668.7565	9.40E+07	3.04E+06	Y I
675	669.3840	2.10E+08	3.22E+06	Ba I
675	670.0635	3.77E+07	3.01E+06	Y I
675	679.3708	9.11E+07	3.00E+06	Y I
675	686.5687	4.17E+07	2.93E+06	Ba I
700	686.5687	5.40E+07	4.81E+06	Ba I
700	705.9938	3.82E+08	5.36E+06	Ba I
700	712.0326	2.24E+08	4.82E+06	Ba I
725	712.0326	2.46E+08	4.95E+06	Ba I
725	719.5232	8.31E+07	4.65E+06	Ba I
725	728.0297	3.43E+08	5.10E+06	Ba I

Table D.9: Emission Line Data–400 mTorr, 31.4 mm – Continued

window (nm)	λ (nm)	Φ_{line} (photons)	σ_Φ (photons)	Source
725	739.2407	1.39E+08	4.56E+06	Ba I
750	739.2407	1.58E+08	2.86E+06	Ba I
750	741.7530	4.05E+07	2.62E+06	Ba I
750	748.8077	2.04E+08	3.10E+06	Ba I
750	761.0480	3.00E+07	2.50E+06	Ba I
775	761.0480	4.29E+07	4.31E+06	Ba I
775	767.2087	3.28E+08	4.85E+06	Ba I
775	778.0479	2.43E+08	4.52E+06	Ba I
800	790.5748	2.32E+08	3.66E+06	Ba I
800	791.1334	2.68E+08	3.75E+06	Ba I
800	793.3124	3.88E+07	3.43E+06	Cu I
800	809.2631	5.05E+07	3.30E+06	Cu I
825	821.0249	7.17E+07	3.15E+06	Ba I
850	856.0000	3.71E+08	5.59E+06	Ba I

Table D.10: Emission Line Data–400 mTorr, 36.0 mm

window (nm)	λ (nm)	Φ_{line} (photons)	σ_Φ (photons)	Source
500	488.3686	4.48E+07	5.78E+06	Y II
500	493.4076	1.77E+08	6.44E+06	Ba II
500	508.7423	5.87E+07	5.54E+06	Y II
500	510.5537	6.99E+07	5.57E+06	Cu I
525	508.7423	3.02E+07	2.99E+06	Y II
525	510.5537	6.32E+07	3.17E+06	Cu I
525	520.0410	3.52E+07	2.97E+06	Y II
525	520.5715	4.61E+07	3.03E+06	Y II
525	521.8198	3.23E+07	2.99E+06	Cu I

Table D.10: Emission Line Data–400 mTorr, 36.0 mm – Continued

window (nm)	λ (nm)	Φ_{line} (photons)	σ_{Φ} (photons)	Source
550	542.4554	7.51E+07	6.50E+06	Ba I
550	546.6467	1.15E+08	6.46E+06	Y I
550	551.9042	1.20E+08	6.45E+06	Ba I
550	552.7530	1.21E+08	6.35E+06	Y I
550	553.5480	4.50E+08	7.39E+06	Ba I
550	558.1832	6.74E+07	7.94E+06	Y I
550	560.6317	1.96E+07	6.29E+06	Y I
550	563.0130	6.07E+07	6.39E+06	Y I
575	560.6317	2.19E+07	3.89E+06	Y I
575	563.0130	6.96E+07	3.92E+06	Y I
575	564.4661	3.03E+07	5.24E+06	Y I
575	567.5280	3.15E+07	3.99E+06	Y I
575	567.9995	1.29E+07	3.95E+06	Ba I
575	577.7618	1.24E+08	4.12E+06	Ba I
575	578.2130	6.41E+07	3.93E+06	Cu I
575	580.0225	4.91E+07	3.86E+06	Ba I
575	580.5678	4.21E+07	3.84E+06	Ba I
575	582.6273	9.92E+07	3.89E+06	Ba I
575	585.3668	1.45E+08	4.04E+06	Ba II
600	585.3668	1.44E+08	1.07E+07	Ba II
600	590.7633	2.48E+07	1.05E+07	Ba I
600	597.1693	6.65E+08	1.11E+07	Ba I
600	599.7084	1.34E+08	1.04E+07	Ba I
600	601.9465	3.01E+08	1.75E+07	Ba I
600	606.3109	1.28E+08	1.03E+07	Ba I
600	611.0779	2.16E+08	1.05E+07	Ba I

Table D.10: Emission Line Data–400 mTorr, 36.0 mm – Continued

window (nm)	λ (nm)	Φ_{line} (photons)	σ_{Φ} (photons)	Source
600	614.1713	3.60E+08	1.03E+07	Ba II
625	611.0779	1.76E+08	1.10E+07	Ba I
625	614.1713	3.28E+08	1.12E+07	Ba II
625	619.1733	1.92E+08	1.09E+07	Y I
625	622.2603	9.18E+07	1.28E+07	Y I
625	634.1677	1.47E+08	1.05E+07	Ba I
650	640.2025	2.96E+07	5.72E+06	Y I
650	643.5034	1.71E+08	5.84E+06	Y I
650	645.0850	1.23E+08	5.75E+06	Ba I
650	648.2910	1.49E+08	5.75E+06	Ba I
650	649.6896	3.27E+08	8.17E+06	Ba II
650	649.8757	2.24E+08	7.74E+06	Ba I
650	652.7308	1.78E+08	5.74E+06	Ba I
650	659.5323	1.53E+08	5.64E+06	Ba I
675	659.5323	1.72E+08	2.72E+06	Ba I
675	667.5267	1.46E+08	2.61E+06	Ba I
675	668.7565	7.81E+07	2.46E+06	Y I
675	669.3840	1.73E+08	2.62E+06	Ba I
675	670.0635	2.92E+07	2.44E+06	Y I
675	679.3708	7.58E+07	2.43E+06	Y I
675	686.5687	3.12E+07	2.36E+06	Ba I
700	686.5687	4.16E+07	4.24E+06	Ba I
700	705.9938	3.17E+08	4.73E+06	Ba I
700	712.0326	1.87E+08	4.25E+06	Ba I
725	712.0326	2.03E+08	4.03E+06	Ba I
725	719.5232	7.04E+07	3.78E+06	Ba I

Table D.10: Emission Line Data–400 mTorr, 36.0 mm – Continued

window (nm)	λ (nm)	Φ_{line} (photons)	σ_Φ (photons)	Source
725	728.0297	2.80E+08	4.15E+06	Ba I
725	739.2407	1.10E+08	3.70E+06	Ba I
750	739.2407	1.32E+08	2.77E+06	Ba I
750	741.7530	3.51E+07	2.57E+06	Ba I
750	748.8077	1.80E+08	2.89E+06	Ba I
750	761.0480	2.63E+07	2.46E+06	Ba I
775	761.0480	3.08E+07	4.27E+06	Ba I
775	767.2087	2.77E+08	4.81E+06	Ba I
775	778.0479	2.01E+08	4.44E+06	Ba I
800	790.5748	1.83E+08	2.95E+06	Ba I
800	791.1334	2.20E+08	3.04E+06	Ba I
800	793.3124	1.93E+07	2.76E+06	Cu I
800	809.2631	2.90E+07	2.66E+06	Cu I
825	821.0249	7.29E+07	3.19E+06	Ba I
850	856.0000	3.17E+08	5.73E+06	Ba I

Table D.11: Emission Line Data–400 mTorr, 45.7 mm

window (nm)	λ (nm)	Φ_{line} (photons)	σ_Φ (photons)	Source
500	493.4076	4.65E+07	4.75E+06	Ba II
525	508.7423	1.52E+07	1.70E+06	Y II
525	510.5537	2.19E+07	1.77E+06	Cu I
525	515.3231	1.15E+07	1.64E+06	Cu I
525	522.0100	6.04E+06	1.60E+06	Cu I
550	542.4554	2.87E+07	3.39E+06	Ba I
550	546.6467	3.24E+07	3.35E+06	Y I
550	551.9042	4.23E+07	3.35E+06	Ba I

Table D.11: Emission Line Data–400 mTorr, 45.7 mm – Continued

window (nm)	λ (nm)	Φ_{line} (photons)	σ_Φ (photons)	Source
550	552.7530	4.48E+07	3.30E+06	Y I
550	553.5480	2.45E+08	3.96E+06	Ba I
550	558.1832	1.92E+07	3.30E+06	Y I
550	563.0130	1.86E+07	3.33E+06	Y I
575	563.0130	1.63E+07	2.16E+06	Y I
575	577.7618	5.54E+07	2.42E+06	Ba I
575	578.2130	2.76E+07	2.27E+06	Cu I
575	580.0225	2.09E+07	2.14E+06	Ba I
575	580.5678	1.87E+07	2.13E+06	Ba I
575	582.6273	3.49E+07	2.16E+06	Ba I
575	585.3668	5.96E+07	2.33E+06	Ba II
600	585.3668	6.05E+07	1.00E+07	Ba II
600	597.1693	4.43E+08	1.05E+07	Ba I
600	599.7084	4.50E+07	9.78E+06	Ba I
600	601.9465	2.14E+08	9.89E+06	Ba I
600	606.3109	6.51E+07	9.66E+06	Ba I
600	611.0779	1.08E+08	9.70E+06	Ba I
600	614.1713	7.67E+07	9.52E+06	Ba II
625	611.0779	8.72E+07	7.93E+06	Ba I
625	614.1713	4.33E+07	9.96E+06	Ba II
625	619.1733	1.10E+08	7.84E+06	Y I
625	622.2603	4.32E+07	9.93E+06	Y I
625	634.1677	7.55E+07	7.60E+06	Ba I
650	634.1677	1.04E+08	6.70E+06	Ba I
650	640.2025	1.27E+07	3.13E+06	Y I
650	643.5034	9.51E+07	3.21E+06	Y I

Table D.11: Emission Line Data–400 mTorr, 45.7 mm – Continued

window (nm)	λ (nm)	Φ_{line} (photons)	σ_{Φ} (photons)	Source
650	645.0850	6.17E+07	3.14E+06	Ba I
650	648.2910	8.00E+07	3.15E+06	Ba I
650	649.6896	1.44E+08	4.60E+06	Ba II
650	649.8757	1.24E+08	4.52E+06	Ba I
650	652.7308	9.34E+07	3.15E+06	Ba I
650	659.5323	8.77E+07	3.10E+06	Ba I
675	659.5323	8.70E+07	1.88E+06	Ba I
675	667.5267	6.89E+07	1.79E+06	Ba I
675	668.7565	3.83E+07	1.71E+06	Y I
675	669.3840	8.38E+07	1.82E+06	Ba I
675	679.3708	3.59E+07	1.70E+06	Y I
675	686.5687	1.65E+07	1.65E+06	Ba I
700	686.5687	2.02E+07	2.54E+06	Ba I
700	705.9938	1.76E+08	2.85E+06	Ba I
700	712.0326	9.37E+07	2.52E+06	Ba I
725	712.0326	1.07E+08	2.59E+06	Ba I
725	719.5232	2.77E+07	2.42E+06	Ba I
725	728.0297	1.49E+08	2.67E+06	Ba I
725	739.2407	5.54E+07	2.37E+06	Ba I
750	739.2407	6.42E+07	1.92E+06	Ba I
750	741.7530	1.83E+07	1.80E+06	Ba I
750	748.8077	9.87E+07	2.05E+06	Ba I
775	761.0480	1.26E+07	2.40E+06	Ba I
775	767.2087	1.59E+08	2.75E+06	Ba I
775	778.0479	1.03E+08	2.48E+06	Ba I
800	790.5748	7.98E+07	3.50E+06	Ba I

Table D.11: Emission Line Data–400 mTorr, 45.7 mm – Continued

window (nm)	λ (nm)	Φ_{line} (photons)	σ_Φ (photons)	Source
800	791.1334	1.38E+08	3.83E+06	Ba I
850	856.0000	1.76E+08	3.81E+06	Ba I

D.3 Ba I Beer-Lambert Correction Factors

The Ba I Beer-Lambert self-absorption factor, $N_j x$ for each observed condition is listed below, along with the associated error. These values were determined using spectral data for the Ba I $^3F^\circ \rightarrow {}^3D$ manifold.

Table D.12: Beer-Lambert Correction Factors for Ba I

Pressure (mTorr)	Distance (mm)	$N_j x$ (1E8 nm^2)	σ (1E8 nm^2)
50	31.4	1.108E-04	1.63E-05
50	36.0	1.066E-04	1.51E-05
50	45.7	1.028E-04	1.15E-05
50	55.0	9.736E-05	1.19E-05
150	31.4	1.308E-04	1.07E-05
150	36.0	1.345E-04	1.31E-05
150	45.7	1.236E-04	1.34E-05
150	55.0	1.180E-04	1.33E-05
400	31.4	1.270E-04	1.38E-05
400	36.0	1.303E-04	1.33E-05
400	45.7	1.274E-04	1.66E-05

D.4 Corrected Ba I Fluences

The tables below present the corrected fluences for Ba I transitions terminating on the ^3D metastable states. Corrections were performed by using the Beer-Lambert law using self-absorption correction factors shown in the previous section.

Table D.13: Corrected Ba I Fluences–50 mTorr, 31.4 mm

Window (nm)	λ (nm)	Φ_{line} (photons)	σ_{Φ} (photons)
600	590.7633	1.67E+07	5.54E+06
600	597.1693	2.43E+08	3.09E+07
600	599.7084	1.48E+08	3.40E+07
600	601.9465	2.16E+08	4.55E+07
600	606.3109	3.30E+08	8.03E+07
600	611.0799	4.15E+08	1.19E+08
625	611.0799	4.56E+08	1.28E+08
625	634.1677	2.44E+08	3.63E+07
650	645.0850	2.16E+08	2.87E+07
650	649.8757	9.38E+08	4.02E+08
650	652.7308	5.30E+08	9.58E+07
650	659.5323	4.84E+08	1.03E+08
675	667.5267	2.19E+08	1.54E+07
675	669.3840	2.46E+08	1.58E+07
700	705.9938	2.10E+09	1.20E+09
700	712.0326	3.45E+08	6.49E+07
725	712.0326	3.78E+08	6.94E+07
725	728.0297	1.34E+09	5.72E+08
750	748.8077	2.69E+08	2.32E+07
775	767.2087	7.96E+08	2.16E+08
775	778.0479	3.55E+08	3.48E+07

Table D.14: Corrected Ba I Fluences–50 mTorr, 36.0 mm

Window (nm)	λ (nm)	Φ_{line} (photons)	σ_{Φ} (photons)
575	580.5678	4.14E+07	3.97E+06
600	590.7633	1.46E+07	5.33E+06

Table D.14: Corrected Ba I Fluences–50 mTorr, 36.0 mm – Continued

Window (nm)	λ (nm)	Φ_{line} (photons)	σ_{Φ} (photons)
600	597.1693	2.59E+08	3.15E+07
600	599.7084	1.75E+08	3.74E+07
600	601.9465	2.35E+08	4.69E+07
600	606.3109	3.27E+08	7.61E+07
600	611.0779	2.45E+08	5.37E+06
625	611.0779	2.81E+08	7.70E+06
625	634.1677	3.07E+08	4.41E+07
650	645.0850	2.28E+08	2.96E+07
650	649.8757	1.06E+09	4.31E+08
650	652.7308	5.42E+08	9.37E+07
650	659.5323	5.19E+08	1.05E+08
675	659.5323	5.87E+07	1.07E+08
675	667.5267	2.50E+08	1.71E+07
675	669.3840	2.84E+08	1.77E+07
700	705.9938	2.38E+09	1.29E+09
700	712.0326	2.74E+08	5.47E+06
725	712.0326	3.39E+08	8.83E+06
725	728.0297	1.76E+09	7.19E+08
750	748.8077	3.20E+08	2.64E+07
775	767.2087	8.94E+08	2.30E+08
775	778.0479	4.26E+08	3.94E+07

Table D.15: Corrected Ba I Fluences–50 mTorr, 45.7 mm

Window (nm)	λ (nm)	Φ_{line} (photons)	σ_{Φ} (photons)
575	580.5678	2.74E+07	2.37E+06
600	590.7633	1.35E+07	4.35E+06

Table D.15: Corrected Ba I Fluences–50 mTorr, 45.7 mm – Continued

Window (nm)	λ (nm)	Φ_{line} (photons)	σ_{Φ} (photons)
600	597.1693	1.96E+08	2.22E+07
600	599.7084	1.09E+08	2.28E+07
600	601.9465	1.59E+08	3.03E+07
600	606.3109	2.06E+08	4.49E+07
600	611.0779	1.68E+08	4.39E+06
625	611.0779	1.52E+08	3.73E+06
625	634.1677	1.66E+08	2.13E+07
650	645.0850	1.54E+08	1.89E+07
650	649.8757	7.26E+08	2.67E+08
650	652.7308	3.64E+08	5.58E+07
650	659.5323	3.37E+08	6.07E+07
675	667.5267	1.69E+08	1.12E+07
675	669.3840	1.91E+08	1.15E+07
700	705.9938	1.66E+09	8.07E+08
700	712.0326	1.90E+08	4.66E+06
725	712.0326	2.14E+08	5.29E+06
725	728.0297	1.11E+09	4.05E+08
750	741.7530	2.28E+07	2.54E+06
750	748.8077	2.33E+08	1.76E+07
775	767.2087	6.17E+08	1.42E+08
775	778.0479	2.66E+08	2.32E+07

Table D.16: Corrected Ba I Fluences–50 mTorr, 55.0 mm

Window (nm)	λ (nm)	Φ_{line} (photons)	σ_{Φ} (photons)
600	597.1693	1.99E+08	2.16E+07
600	599.7084	7.57E+07	1.69E+07

Table D.16: Corrected Ba I Fluences–50 mTorr, 55.0 mm – Continued

Window (nm)	λ (nm)	Φ_{line} (photons)	σ_Φ (photons)
600	601.9465	1.42E+08	2.65E+07
600	606.3109	1.65E+08	3.59E+07
600	611.0779	1.47E+08	4.08E+06
625	611.0779	1.46E+08	3.90E+06
625	634.1677	1.66E+08	2.10E+07
650	645.0850	1.19E+08	1.53E+07
650	649.8757	6.40E+08	2.28E+08
650	652.7308	3.09E+08	4.71E+07
650	659.5323	2.89E+08	5.15E+07
675	659.5323	3.32E+08	5.21E+07
675	667.5267	1.48E+08	9.36E+06
675	669.3840	1.74E+08	9.91E+06
700	705.9938	1.62E+09	7.69E+08
700	712.0326	1.89E+08	5.15E+06
725	712.0326	2.10E+08	4.69E+06
725	728.0297	1.07E+09	3.78E+08
750	741.7530	2.32E+07	2.35E+06
750	748.8077	2.22E+08	1.63E+07
775	767.2087	5.95E+08	1.34E+08
775	778.0479	2.63E+08	2.24E+07

Table D.17: Corrected Ba I Fluences–150 mTorr, 31.4 mm

Window (nm)	λ (nm)	Φ_{line} (photons)	σ_Φ (photons)
600	590.7633	3.54E+07	7.42E+06
600	597.1693	5.26E+08	6.23E+07
600	599.7084	2.58E+08	5.74E+07

Table D.17: Corrected Ba I Fluences–150 mTorr, 31.4 mm – Continued

Window (nm)	λ (nm)	Φ_{line} (photons)	σ_{Φ} (photons)
600	601.9465	4.32E+08	8.65E+07
600	606.3109	4.67E+08	1.14E+08
600	611.0779	3.11E+08	7.44E+06
625	611.0779	2.86E+08	6.91E+06
625	634.1677	3.64E+08	5.19E+07
650	645.0850	3.35E+08	3.74E+07
650	649.8757	1.39E+09	5.84E+08
650	652.7308	7.28E+08	1.16E+08
650	659.5323	7.30E+08	1.35E+08
675	659.5323	8.81E+08	1.49E+08
675	667.5267	3.84E+08	2.42E+07
675	669.3840	4.22E+08	2.44E+07
700	705.9938	2.85E+09	1.61E+09
700	712.0326	3.13E+07	6.22E+06
725	712.0326	3.46E+07	6.32E+06
725	728.0297	1.78E+09	7.54E+08
750	748.8077	3.83E+08	3.23E+07
775	767.2087	9.99E+08	2.67E+08
775	778.0479	4.56E+08	4.32E+07

Table D.18: Corrected Ba I Fluences–150 mTorr, 36.0 mm

Window (nm)	λ (nm)	Φ_{line} (photons)	σ_{Φ} (photons)
575	580.5678	6.16E+07	3.95E+06
600	590.7633	2.33E+07	1.02E+07
600	597.1693	8.59E+08	1.06E+08
600	599.7084	1.66E+08	4.82E+07

Table D.18: Corrected Ba I Fluences–150 mTorr, 36.0 mm – Continued

Window (nm)	λ (nm)	Φ_{line} (photons)	σ_{Φ} (photons)
600	601.9465	5.38E+08	1.15E+08
600	606.3109	2.38E+08	7.39E+07
600	611.0779	1.89E+08	1.00E+07
625	611.0779	3.00E+08	8.13E+06
625	634.1677	3.74E+08	5.81E+07
650	645.0850	3.37E+08	4.01E+07
650	649.8757	1.43E+09	6.44E+08
650	652.7308	7.39E+08	1.28E+08
650	659.5323	7.40E+08	1.50E+08
675	659.5323	7.73E+08	1.45E+08
675	667.5267	3.42E+08	2.33E+07
675	669.3840	3.76E+08	2.35E+07
700	705.9938	3.19E+09	1.94E+09
700	712.0326	3.33E+08	6.62E+06
725	712.0326	3.84E+08	7.03E+06
725	728.0297	2.07E+09	9.41E+08
750	741.7530	6.27E+07	4.09E+06
750	748.8077	4.35E+08	3.89E+07
775	767.2087	1.20E+09	3.42E+08
775	778.0479	5.15E+08	5.18E+07

Table D.19: Corrected Ba I Fluences–150 mTorr, 45.7 mm

Window (nm)	λ (nm)	Φ_{line} (photons)	σ_{Φ} (photons)
600	590.7633	2.05E+07	5.50E+06
600	597.1693	4.53E+08	5.33E+07
600	599.7084	1.11E+08	2.87E+07

Table D.19: Corrected Ba I Fluences–150 mTorr, 45.7 mm – Continued

Window (nm)	λ (nm)	Φ_{line} (photons)	σ_{Φ} (photons)
600	601.9465	3.31E+08	6.60E+07
600	606.3109	2.33E+08	6.07E+07
600	611.0779	1.61E+08	5.49E+06
625	611.0779	1.68E+08	6.00E+06
625	634.1677	1.91E+08	3.06E+07
650	645.0850	1.72E+08	2.03E+07
650	649.8757	7.76E+08	3.33E+08
650	652.7308	3.83E+08	6.53E+07
650	659.5323	3.87E+08	7.69E+07
675	659.5323	4.06E+08	7.54E+07
675	667.5267	1.90E+08	1.34E+07
675	669.3840	2.05E+08	1.34E+07
700	705.9938	1.70E+09	9.83E+08
700	712.0326	1.93E+08	4.19E+06
725	712.0326	2.05E+08	3.77E+06
725	728.0297	1.00E+09	4.33E+08
750	741.7530	3.28E+07	2.33E+06
750	748.8077	2.25E+08	1.95E+07
775	767.2087	6.12E+08	1.67E+08
775	778.0479	2.67E+08	2.62E+07

Table D.20: Corrected Ba I Fluences–150 mTorr, 55.0 mm

Window (nm)	λ (nm)	Φ_{line} (photons)	σ_{Φ} (photons)
600	590.7633	1.29E+07	3.52E+06
600	597.1693	2.66E+08	3.07E+07
600	599.7084	5.77E+07	1.55E+07

Table D.20: Corrected Ba I Fluences–150 mTorr, 55.0 mm – Continued

Window (nm)	λ (nm)	Φ_{line} (photons)	σ_{Φ} (photons)
600	601.9465	1.78E+08	3.53E+07
600	606.3109	1.11E+08	2.96E+07
600	611.0779	7.45E+07	3.43E+06
625	611.0779	8.27E+07	3.41E+06
625	634.1677	9.28E+07	1.51E+07
650	645.0850	8.55E+07	1.11E+07
650	649.8757	4.65E+08	1.94E+08
650	652.7308	2.05E+08	3.49E+07
650	659.5323	1.91E+08	3.83E+07
675	659.5323	2.13E+08	3.90E+07
675	667.5267	9.44E+07	6.83E+06
675	669.3840	1.08E+08	7.10E+06
700	705.9938	8.98E+08	5.02E+08
700	712.0326	1.48E+08	2.70E+07
725	712.0326	1.70E+08	3.09E+07
725	728.0297	5.58E+08	2.34E+08
750	741.7530	1.51E+07	1.99E+06
750	748.8077	1.25E+08	1.13E+07
775	767.2087	3.38E+08	9.05E+07
775	778.0479	1.38E+08	1.41E+07

Table D.21: Corrected Ba I Fluences–400 mTorr, 31.4 mm

Window (nm)	λ (nm)	Φ_{line} (photons)	σ_{Φ} (photons)
600	590.7633	1.78E+07	5.79E+06
600	597.1693	2.56E+08	3.42E+07
600	599.7084	2.03E+08	4.65E+07

Table D.21: Corrected Ba I Fluences–400 mTorr, 31.4 mm – Continued

Window (nm)	λ (nm)	Φ_{line} (photons)	σ_Φ (photons)
600	601.9465	2.39E+08	5.28E+07
600	606.3109	3.69E+08	9.33E+07
600	611.0779	2.34E+08	5.83E+06
625	611.0779	2.30E+08	1.15E+07
625	634.1677	2.48E+08	4.55E+07
650	645.0850	2.16E+08	2.82E+07
650	649.8757	1.31E+09	5.73E+08
650	652.7308	4.78E+08	8.59E+07
650	659.5323	4.60E+08	9.67E+07
675	659.5323	4.69E+08	8.92E+07
675	667.5267	2.39E+08	1.69E+07
675	669.3840	2.65E+08	1.71E+07
700	705.9938	1.93E+09	1.14E+09
700	712.0326	3.58E+08	6.80E+07
725	712.0326	3.93E+08	7.40E+07
725	728.0297	1.14E+09	5.06E+08
750	741.7530	4.11E+07	2.88E+06
750	748.8077	2.50E+08	2.24E+07
775	767.2087	6.89E+08	1.94E+08
775	778.0479	3.07E+08	3.13E+07

Table D.22: Corrected Ba I Fluences–400 mT, 36.0 mm

Window (nm)	λ (nm)	Φ_{line} (photons)	σ_Φ (photons)
600	590.7633	2.48E+07	1.05E+07
600	597.1693	8.94E+08	1.08E+08
600	599.7084	2.27E+08	5.92E+07

Table D.22: Corrected Ba I Fluences–400 mTorr, 36.0 mm – Continued

Window (nm)	λ (nm)	Φ_{line} (photons)	σ_{Φ} (photons)
600	601.9465	5.00E+08	1.18E+08
600	606.3109	2.43E+08	7.43E+07
600	611.0779	2.16E+08	1.05E+07
625	611.0779	1.76E+08	1.10E+07
625	634.1677	2.08E+08	4.06E+07
650	645.0850	1.83E+08	2.32E+07
650	649.8757	7.31E+08	3.30E+08
650	652.7308	3.71E+08	6.66E+07
650	659.5323	3.61E+08	7.58E+07
675	659.5323	4.06E+08	7.67E+07
675	667.5267	1.89E+08	1.34E+07
675	669.3840	2.21E+08	1.41E+07
700	705.9938	1.67E+09	1.00E+09
700	712.0326	3.03E+08	2.18E+07
725	712.0326	3.29E+08	2.27E+07
725	728.0297	9.59E+08	4.30E+08
750	741.7530	3.56E+07	2.67E+06
750	748.8077	2.22E+08	2.02E+07
775	767.2087	5.94E+08	1.70E+08
775	778.0479	2.55E+08	2.70E+07

Table D.23: Corrected Ba I Fluences–400 mTorr, 45.7 mm

Window (nm)	λ (nm)	Φ_{line} (photons)	σ_{Φ} (photons)
600	597.1693	5.91E+08	7.90E+07
600	599.7084	7.50E+07	3.08E+07
600	601.9465	3.51E+08	8.25E+07

Table D.23: Corrected Ba I Fluences–400 mTorr, 45.7 mm – Continued

Window (nm)	λ (nm)	Φ_{line} (photons)	σ_{Φ} (photons)
600	606.3109	1.22E+08	4.71E+07
600	611.0779	1.08E+08	9.70E+06
625	611.0779	8.72E+07	7.93E+06
625	634.1677	1.06E+08	2.45E+07
650	634.1677	1.46E+08	2.85E+07
650	645.0850	9.08E+07	1.27E+07
650	649.8757	3.94E+08	1.88E+08
650	652.7308	1.91E+08	3.77E+07
650	659.5323	2.03E+08	4.63E+07
675	659.5323	2.01E+08	4.31E+07
675	667.5267	8.90E+07	7.57E+06
675	669.3840	1.06E+08	8.10E+06
700	705.9938	8.94E+08	5.67E+08
700	712.0326	1.50E+08	3.09E+07
725	712.0326	1.71E+08	3.49E+07
725	728.0297	4.97E+08	2.36E+08
750	741.7530	1.86E+07	1.94E+06
750	748.8077	1.22E+08	1.21E+07
775	767.2087	3.35E+08	1.00E+08
775	778.0479	1.30E+08	1.46E+07

Appendix E. Electronic State Distributions

This section presents the tabulated electronic state distributions for Y, Ba, and Cu neutrals. The results are presented as a ratio, R_{pop} of the upper state population to the ground state population:

$$R_{pop} = \frac{N_i/g_i}{N_o/g_o} \tag{E.1}$$

where N_i and N_o are respectively the upper and ground state populations, and g_i and g_o are respectively the upper and ground state degeneracies.

The upper state populations are estimated from the spectral fluences by the relation:

$$\Phi_{line} = kA_{ij}N_i \tag{E.2}$$

where Φ_{line} is the line fluence, A_{ij} is the transition probability, and k is the dimensionless ratio of $d\Omega/4\pi$, where $d\Omega$ is the effective solid angle (in steradians) subtended by the detector element. It is assumed this ratio is independent of wavelength. Substitution into equation E.1 yields:

$$R_{pop} = \frac{\Phi_{line}/(A_{ij}g_i)}{kN_o/g_o} = \frac{\Phi_{line}/(A_{ij}g_i)}{\alpha} \tag{E.3}$$

where $\alpha = kN_o/g_o$.

The unknown, α, can be determined by invoking a boundary condition, requiring that $R_{pop} = 1$ in the limit where the upper state energy approaches zero. This is done by plotting the values of $\mathrm{Ln}(\Phi_{line}/(A_{ij}g_i))$ as a function of upper state energy, fitting the data to a model (such as the Boltzmann LTE model), and assigning the value of the y-intercept to $\mathrm{Ln}(\alpha)$.

The electronic state distributions were also studied for deviations from the nascent stoichiometry of Y:Ba:Cu in proportion to 1:2:3. This was done by plot-

ting their electronic state distributions (R_{pop} vs E_i) with the value of α for each element adjusted for the nascent stoichiometry. Noting the value of the geometric optical factor, k, is independent of the element observed yields the relation between values of α for each element, given the stoichiometric and degeneracy ratios:

$$k = \frac{\alpha_Y}{N_Y/(g_o)_Y} = \frac{\alpha_{Ba}}{N_{Ba}/(g_o)_{Ba}} = \frac{\alpha Cu}{N_{Cu}/(g_o)_{Cu}} \tag{E.4}$$

In this study, α_Y is used as the basis for comparison, and α_{Ba} and α_{Cu} are expressed in terms of α_Y. As previously stated, the stoichiometric ratio is 1:2:3 for Y:Ba:Cu. It is also noted the the ground state term for Y is ${}^2D_{3/2}$, for Ba is ${}^1S_0$, while for Cu, it is ${}^2S_{1/2}$. [65] This results in a Y:Ba:Cu ground state degeneracy ratio of 4:1:2. Using the stoichiometric and degeneracy ratios, the values of α_{Ba} and α_{Cu} are expressed in terms of α_Y as:

$$\alpha_Y = \frac{1}{8}\alpha_{Ba} = \frac{1}{6}\alpha_{Cu} \tag{E.5}$$

or

$$\alpha_{Ba} = 8\alpha_Y \tag{E.6}$$

and

$$\alpha_{Cu} = 6\alpha_Y \tag{E.7}$$

By plotting the electronic state distributions on a semilog plot (Ln(R_{pop}) vs (E_i), using values of α determined from the stoichiometric ratios, deviations from nascent stoichiometry may be monitored. At nascent stoichiometry, the y-intercepts of the plot for Ba and Cu should be equal to zero within rounding error. (As the element of comparison, the yttrium y-intercept will automatically equal zero–any slight deviation being due to rounding error). If the y-intercept is greater than zero, this indicates the

α computed from stoichiometry is too small because the bulk stoichiometric ratio of Ba:Y or Cu:Y is greater than the actual stoichiometric ratio, possibly due to depletion of atomic Y from oxide formation. Likewise, if the y-intercept for Ba or Cu is less than zero, this would indicate that the actual stoichiometric ratio reflects depletion of atomic Ba or Cu relative to the atomic Y population.

E.1 50 mTorr, 31.4 mm

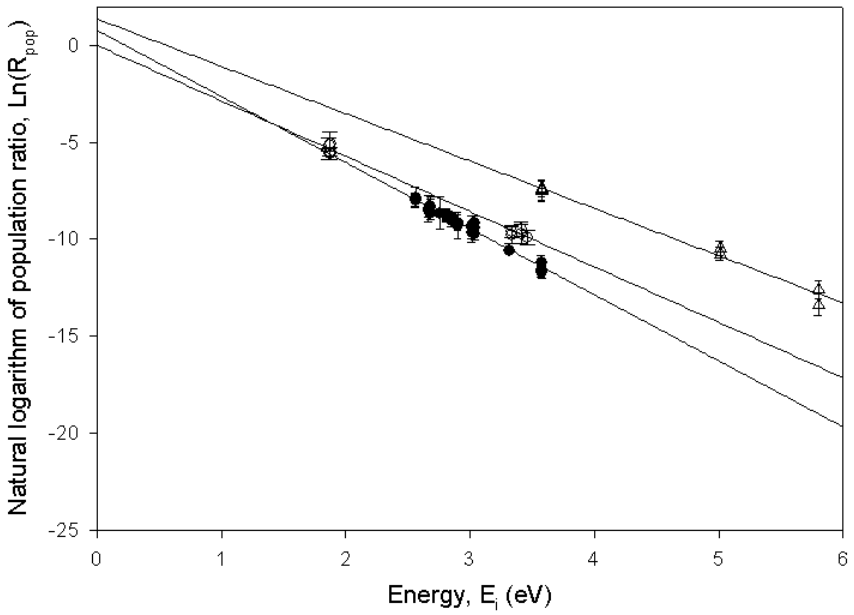

Figure E.1: Electronic State Distributions at 50 mTorr, 31.4 mm. (○ Y I, • Ba I, △ Cu I)

Table E.1: Y I Electronic State Distributions at 50 mTorr, 31.4 mm

Window (nm)	λ (nm)	E_i (eV)	Ln(R_{pop})	σ
625	619.1730	1.876	-5.585	0.290
650	643.5000	1.867	-5.593	0.291
625	622.2590	1.867	-5.121	0.344
650	640.2010	1.876	-5.091	0.608
550	546.6460	3.465	-9.916	0.355
550	552.7540	3.412	-9.475	0.348

Table E.1: Y I Electronic State Distributions at 50 mTorr, 31.4 mm – Continued

Window (nm)	λ (nm)	E_i (eV)	Ln(R_{pop})	σ
550	563.0130	3.334	-9.805	0.426
575	563.0130	3.334	-9.602	0.322
575	560.6330	3.412	-9.709	0.487

Table E.2: Ba I Electronic State Distributions at 50 mTorr, 31.4 mm

Window (nm)	λ (nm)	E_i (eV)	Ln(R_{pop})	σ
775	767.2085	2.564	-7.838	0.532
775	778.0478	2.564	-7.965	0.360
750	748.8075	2.667	-8.538	0.346
725	728.0296	2.667	-8.415	0.689
725	712.0331	2.681	-8.272	0.443
850	856.0000	2.681	-8.684	0.288
700	712.0331	2.681	-8.364	0.451
700	705.9943	2.761	-8.661	0.836
675	667.5270	2.811	-8.848	0.183
650	659.5325	2.811	-8.754	0.329
675	669.3842	2.851	-8.985	0.177
650	652.7311	2.851	-9.033	0.296
650	645.0851	2.851	-8.834	0.247
650	649.8760	2.903	-9.291	0.693
625	634.1680	2.903	-9.134	0.416
700	686.5686	3.016	-9.270	0.462
675	686.5686	3.016	-9.669	0.470
600	590.7636	3.016	-9.397	0.602
725	739.2405	3.040	-9.730	0.318
800	790.5747	3.040	-9.400	0.278

Table E.2: Ba I Electronic State Distributions at 50 mTorr, 31.4 mm – Continued

Window (nm)	λ (nm)	E_i (eV)	Ln(R_{pop})	σ
750	739.2405	3.040	-9.404	0.284
725	719.5230	3.040	-9.190	0.367
575	582.6274	3.318	-10.573	0.158
575	580.0230	3.573	-11.567	0.371
550	551.9044	3.573	-11.236	0.368
575	577.7618	3.581	-11.727	0.301

Table E.3: Cu I Electronic State Distributions at 50 mTorr, 31.4 mm

Window (nm)	λ (nm)	E_i (eV)	Ln(R_{pop})	σ
500	510.5540	3.577	-7.494	0.547
525	510.5540	3.577	-7.379	0.401
575	570.0200	3.577	-7.461	0.540
800	793.3130	5.013	-10.450	0.376
800	809.2631	5.013	-10.765	0.335
525	515.3240	5.803	-13.403	0.556
525	521.8200	5.804	-12.600	0.464

E.2 50 mTorr, 36.0 mm

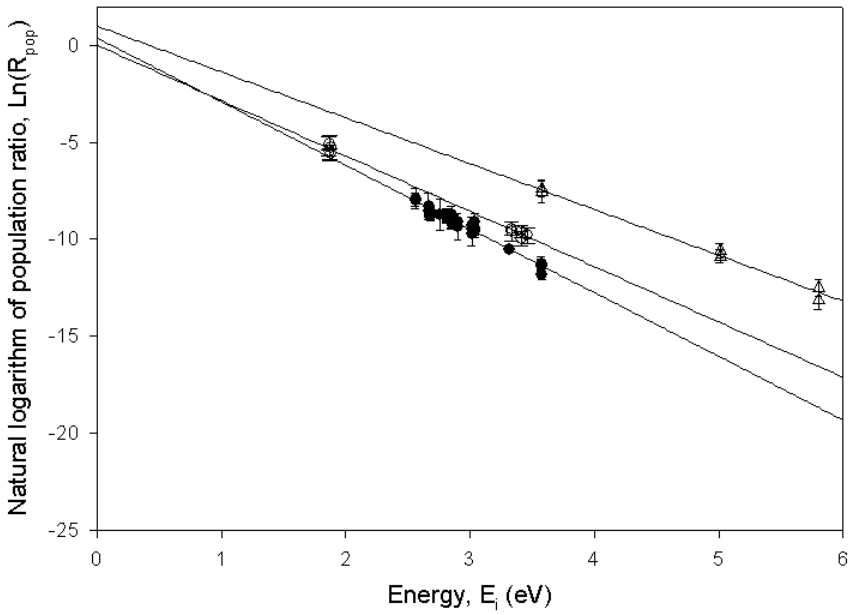

Figure E.2: Electronic State Distributions at 50 mTorr, 36.0 mm. (○ Y I, • Ba I, △ Cu I)

Table E.4: Y I Electronic State Distributions at 50 mTorr, 36.0 mm

Window (nm)	λ (nm)	E_i (eV)	Ln(R_{pop})	σ
625	619.1730	1.876	-5.586	0.289
650	643.5000	1.867	-5.061	0.347
625	622.2590	1.867	-5.420	0.289
650	640.2010	1.876	-5.281	0.650
550	546.6460	3.465	-9.791	0.410
550	552.7540	3.412	-9.610	0.328
550	563.0130	3.334	-9.451	0.342
575	563.0130	3.334	-9.584	0.486
575	560.6330	3.412	-9.974	0.352

Table E.5: Ba I Electronic State Distributions at 50 mTorr, 36.0 mm

Window (nm)	λ (nm)	E_i (eV)	Ln(R_{pop})	σ
775	767.2085	2.564	-7.899	0.518
775	778.0478	2.564	-7.961	0.355
725	728.0296	2.667	-8.317	0.670
750	748.8075	2.667	-8.541	0.342
700	712.0331	2.681	-8.772	0.282
725	712.0331	2.681	-8.559	0.286
850	856.0000	2.681	-8.697	0.287
700	705.9943	2.761	-8.712	0.804
650	659.5325	2.811	-8.862	0.318
675	659.5325	2.811	-8.739	0.296
675	667.5270	2.811	-8.892	0.182
650	652.7311	2.851	-9.188	0.288
675	669.3842	2.851	-9.019	0.176
650	645.0851	2.851	-8.954	0.244
750	761.0477	2.851	-8.997	0.407
775	761.0477	2.851	-8.731	0.455
650	649.8760	2.903	-9.343	0.670
625	634.1680	2.903	-9.092	0.411
600	590.7636	3.016	-9.711	0.636
675	686.5686	3.016	-9.447	0.369
700	686.5686	3.016	-9.274	0.421
800	790.5747	3.040	-9.528	0.278
725	739.2405	3.040	-9.582	0.331
750	739.2405	3.040	-9.582	0.331
725	719.5230	3.040	-9.077	0.396
575	582.6274	3.318	-10.520	0.160

Table E.5: Ba I Electronic State Distributions at 50 mTorr, 36.0 mm – Continued

Window (nm)	λ (nm)	E_i (eV)	Ln(R_{pop})	σ
550	551.9044	3.573	-11.251	0.361
575	580.0230	3.573	-11.404	0.368
575	577.7618	3.581	-11.801	0.307

Table E.6: Cu I Electronic State Distributions at 50 mTorr, 36.0 mm

Window (nm)	λ (nm)	E_i (eV)	Ln(R_{pop})	σ
500	510.5540	3.577	-7.568	0.542
525	510.5540	3.577	-7.400	0.392
575	570.0200	3.577	-7.535	0.600
800	793.3130	5.013	-10.583	0.380
800	809.2631	5.013	-10.888	0.337
525	515.3240	5.803	-13.160	0.473
525	521.8200	5.804	-12.493	0.437

E.3 50 mTorr, 45.7 mm

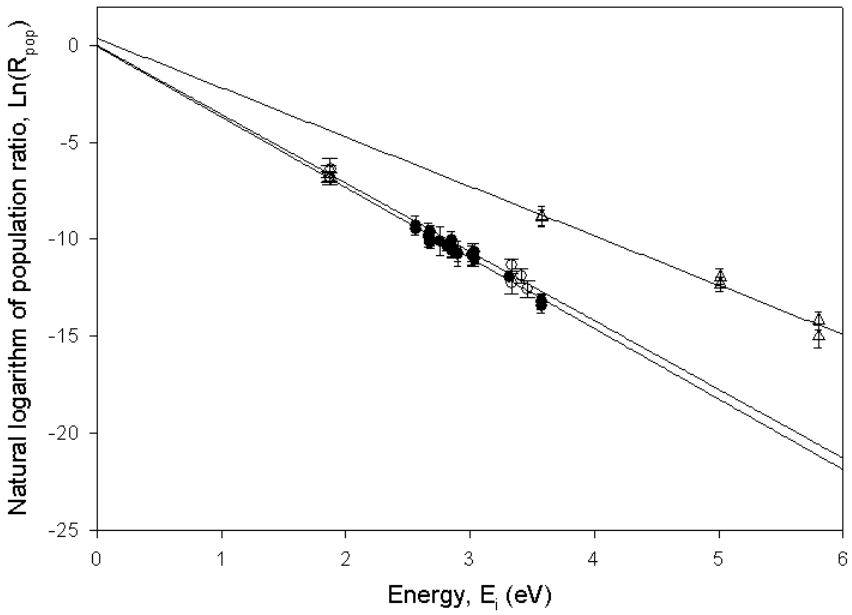

Figure E.3: Electronic State Distributions at 50 mTorr, 45.7 mm. (○ Y I, • Ba I, △ Cu I)

Table E.7: Y I Electronic State Distributions at 50 mTorr, 45.7 mm

Window (nm)	λ (nm)	E_i (eV)	Ln(R_{pop})	σ
650	643.5000	1.867	-6.801	0.287
625	622.2590	1.867	-6.515	0.326
625	619.1730	1.876	-6.879	0.283
650	640.2010	1.876	-6.399	0.579
550	563.0130	3.334	-12.288	0.521
575	563.0130	3.334	-11.336	0.337
550	552.7540	3.412	-11.904	0.382
550	546.6460	3.465	-12.561	0.416

Table E.8: Ba I Electronic State Distributions at 50 mTorr, 45.7 mm

Window (nm)	λ (nm)	E_i (eV)	Ln(R_{pop})	σ
775	767.2085	2.564	-9.302	0.492
775	778.0478	2.564	-9.463	0.349
725	728.0296	2.667	-9.805	0.625
750	748.8075	2.667	-9.891	0.335
700	712.0331	2.681	-10.170	0.287
725	712.0331	2.681	-10.051	0.285
750	741.7536	2.681	-9.631	0.370
850	856.0000	2.681	-10.065	0.289
700	705.9943	2.761	-10.104	0.748
650	659.5325	2.811	-10.323	0.296
675	667.5270	2.811	-10.316	0.180
650	652.7311	2.851	-10.618	0.268
675	669.3842	2.851	-10.447	0.174
650	645.0851	2.851	-10.379	0.237
750	761.0477	2.851	-10.528	0.444
775	761.0477	2.851	-10.021	0.435
650	649.8760	2.903	-10.729	0.395
625	634.1680	2.903	-10.756	0.632
600	590.7636	3.016	-10.817	0.592
675	686.5686	3.016	-10.747	0.389
700	686.5686	3.016	-10.862	0.499
800	790.5747	3.040	-10.947	0.282
725	739.2405	3.040	-11.043	0.344
750	739.2405	3.040	-11.001	0.291
725	719.5230	3.040	-10.648	0.420
575	582.6274	3.318	-11.981	0.157

Table E.8: Ba I Electronic State Distributions at 50 mTorr, 45.7 mm – Continued

Window (nm)	λ (nm)	E_i (eV)	Ln(R_{pop})	σ
550	551.9044	3.573	-13.429	0.389
575	580.0230	3.573	-13.242	0.399
575	577.7618	3.581	-13.197	0.303

Table E.9: Cu I Electronic State Distributions at 50 mTorr, 45.7 mm

Window (nm)	λ (nm)	E_i (eV)	Ln(R_{pop})	σ
500	510.5540	3.577	-8.826	0.552
525	510.5540	3.577	-8.877	0.404
800	793.3130	5.013	-11.942	0.399
800	809.2631	5.013	-12.320	0.355
525	515.3240	5.803	-15.017	0.595
525	521.8200	5.804	-14.203	0.474

E.4 50 mTorr, 55.0 mm

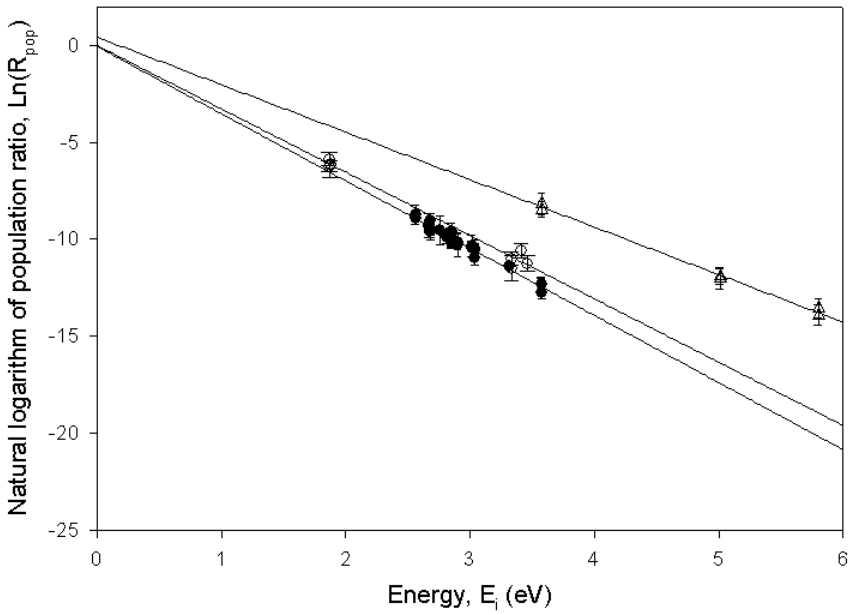

Figure E.4: Electronic State Distributions at 50 mTorr, 55.0 mm. (○ Y I, • Ba I, △ Cu I)

Table E.10: Y I Electronic State Distributions at 50 mTorr, 55.0 mm

Window (nm)	λ (nm)	E_i (eV)	Ln(R_{pop})	σ
650	643.5000	1.867	-6.263	0.284
625	622.2590	1.867	-5.861	0.335
625	619.1730	1.876	-6.210	0.283
650	640.2010	1.876	-6.149	0.650
550	563.0130	3.334	-11.493	0.625
575	563.0130	3.334	-11.009	0.348
550	552.7540	3.412	-10.596	0.371
550	546.6460	3.465	-11.249	0.401

Table E.11: Ba I Electronic State Distributions at 50 mTorr, 55.0 mm

Window (nm)	λ (nm)	E_i (eV)	Ln(R_{pop})	σ
775	767.2085	2.564	-8.752	0.489
775	778.0478	2.564	-8.887	0.346
725	728.0296	2.667	-9.263	0.622
750	748.8075	2.667	-9.356	0.334
700	712.0331	2.681	-9.590	0.427
725	712.0331	2.681	-9.483	0.418
750	741.7536	2.681	-9.028	0.365
850	856.0000	2.681	-9.500	0.286
700	705.9943	2.761	-9.543	0.747
650	659.5325	2.811	-9.895	0.300
675	659.5325	2.811	-9.755	0.278
675	667.5270	2.811	-9.864	0.176
650	652.7311	2.851	-10.196	0.272
675	669.3842	2.851	-9.956	0.170
650	645.0851	2.851	-10.053	0.246
750	761.0477	2.851	-9.974	0.436
775	761.0477	2.851	-9.629	0.476
650	649.8760	2.903	-10.298	0.630
625	634.1680	2.903	-10.145	0.397
675	686.5686	3.016	-10.488	0.400
700	686.5686	3.016	-10.353	0.546
800	790.5747	3.040	-10.538	0.289
725	739.2405	3.040	-10.985	0.356
750	739.2405	3.040	-10.559	0.293
725	719.5230	3.040	-10.476	0.447
575	582.6274	3.318	-11.375	0.155

Table E.11: Ba I Electronic State Distributions at 50 mTorr, 55.0 mm – Continued

Window (nm)	λ (nm)	E_i (eV)	Ln(R_{pop})	σ
550	551.9044	3.573	-12.343	0.398
575	580.0230	3.573	-12.354	0.359
575	577.7618	3.581	-12.739	0.304

Table E.12: Cu I Electronic State Distributions at 50 mT, 55.0 mm

Window (nm)	λ (nm)	E_i (eV)	Ln(R_{pop})	σ
500	510.5540	3.577	-8.156	0.550
525	510.5540	3.577	-8.463	0.414
800	793.3130	5.013	-12.007	0.567
800	809.2631	5.013	-11.924	0.392
525	515.3240	5.803	-13.925	0.516
525	521.8200	5.804	-13.556	0.474

E.5 150 mTorr, 31.4 mm

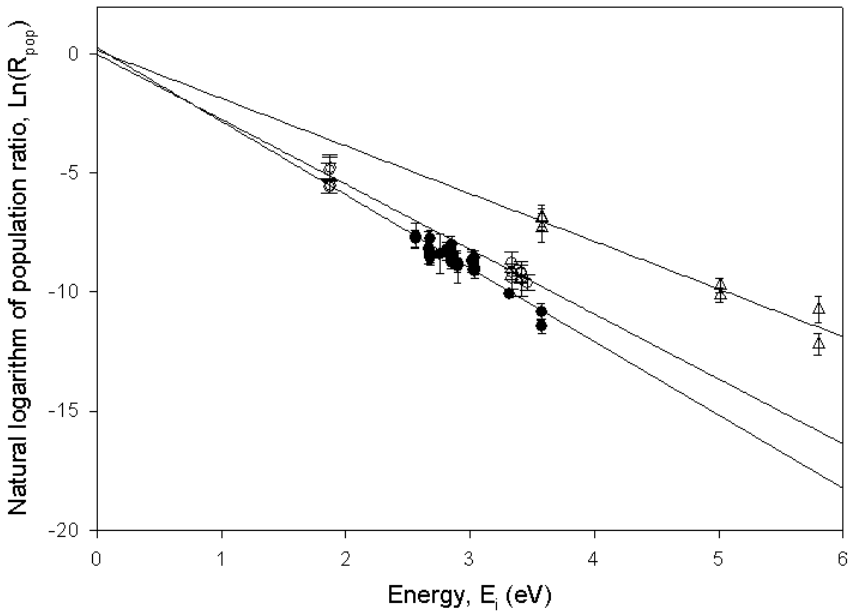

Figure E.5: Electronic State Distributions at 150 mTorr, 31.4 mm. (○ Y I, • Ba I, △ Cu I)

Table E.13: Y I Electronic State Distributions at 150 mTorr, 31.4 mm

Window (nm)	λ (nm)	E_i (eV)	Ln(R_{pop})	σ
650	643.5000	1.867	-5.569	0.293
625	622.2590	1.867	-4.895	0.341
625	619.1730	1.876	-5.551	0.292
625	640.2010	1.876	-4.789	0.468
650	640.2010	1.876	-4.783	0.545
550	563.0130	3.334	-9.436	0.435
575	563.0130	3.334	-9.143	0.318
575	567.5270	3.334	-8.752	0.422
550	552.7540	3.412	-9.214	0.340
550	560.6330	3.412	-9.445	0.713
575	560.6330	3.412	-9.176	0.455
550	546.6460	3.465	-9.603	0.344

Table E.14: Ba I Electronic State Distributions at 150 mTorr, 31.4 mm

Window (nm)	λ (nm)	E_i (eV)	Ln(R_{pop})	σ
775	767.2085	2.564	-7.640	0.527
775	778.0478	2.564	-7.745	0.357
725	728.0296	2.667	-8.156	0.684
750	748.8075	2.667	-8.215	0.344
700	712.0331	2.681	-8.490	0.282
725	712.0331	2.681	-8.392	0.278
750	741.7536	2.681	-7.748	0.339
850	856.0000	2.681	-8.578	0.286
700	705.9943	2.761	-8.386	0.828
650	659.5325	2.811	-8.374	0.301
675	659.5325	2.811	-8.186	0.283
675	667.5270	2.811	-8.316	0.176
650	652.7311	2.851	-8.745	0.274
675	669.3842	2.851	-8.475	0.171
650	645.0851	2.851	-8.425	0.226
750	761.0477	2.851	-8.313	0.355
775	761.0477	2.851	-8.018	0.362
650	649.8760	2.903	-8.931	0.686
625	634.1680	2.903	-8.763	0.409
600	590.7636	3.016	-8.677	0.480
675	686.5686	3.016	-8.658	0.336
700	686.5686	3.016	-8.689	0.376
800	790.5747	3.040	-9.018	0.274
725	739.2405	3.040	-9.110	0.298
750	739.2405	3.040	-8.967	0.279
725	719.5230	3.040	-8.567	0.327

Table E.14: Ba I Electronic State Distributions at 150 mTorr, 31.4 mm – Continued

Window (nm)	λ (nm)	E_i (eV)	Ln(R_{pop})	σ
575	582.6274	3.318	-10.091	0.155
550	551.9044	3.573	-10.854	0.350
575	580.0230	3.573	-10.819	0.341
575	577.7618	3.581	-11.441	0.303

Table E.15: Cu I Electronic State Distributions at 150 mTorr, 31.4 mm

Window (nm)	λ (nm)	E_i (eV)	Ln(R_{pop})	σ
500	510.5540	3.577	-6.881	0.536
525	510.5540	3.577	-6.862	0.389
575	570.0200	3.577	-7.299	0.602
800	793.3130	5.013	-9.723	0.325
800	809.2631	5.013	-10.148	0.307
525	515.3240	5.803	-12.191	0.471
525	521.8200	5.804	-10.740	0.558

E.6 150 mTorr, 36.0 mm

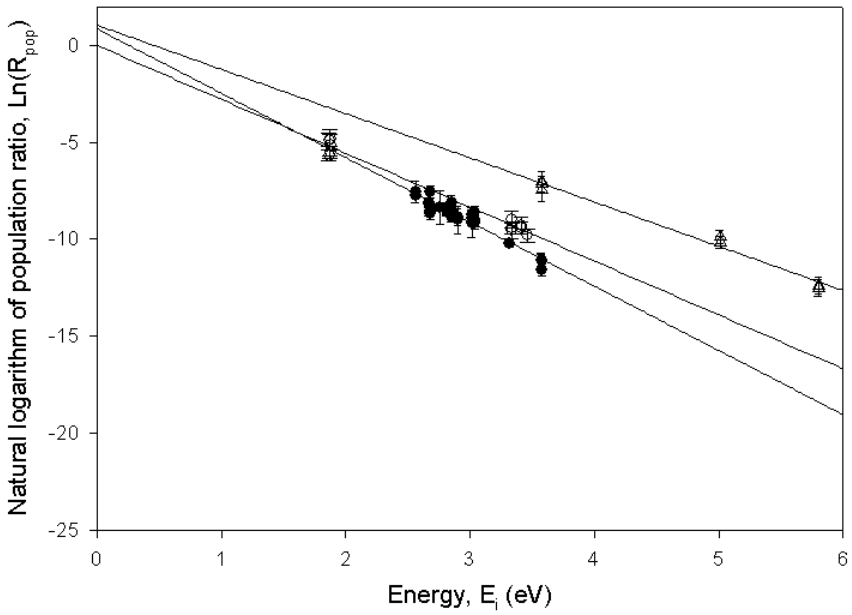

Figure E.6: Electronic State Distributions at 150 mTorr, 36.0 mm. (○ Y I, • Ba I, △ Cu I)

Table E.16: Y I Electronic State Distributions at 150 mTorr, 36.0 mm

Window (nm)	λ (nm)	E_i (eV)	Ln(R_{pop})	σ
650	643.5000	1.867	-5.674	0.292
625	622.2590	1.867	-4.874	0.343
625	619.1730	1.876	-5.514	0.293
625	640.2010	1.876	-5.137	0.572
650	640.2010	1.876	-4.859	0.530
550	563.0130	3.334	-9.561	0.387
575	563.0130	3.334	-9.394	0.320
575	567.5270	3.334	-8.997	0.433
550	552.7540	3.412	-9.414	0.339
575	560.6330	3.412	-9.299	0.441
550	546.6460	3.465	-9.815	0.343

Table E.17: Ba I Electronic State Distributions at 150 mTorr, 36.0 mm

Window (nm)	λ (nm)	E_i (eV)	Ln(R_{pop})	σ
775	767.2085	2.564	-7.562	0.546
775	778.0478	2.564	-7.725	0.362
725	728.0296	2.667	-8.108	0.715
750	748.8075	2.667	-8.191	0.349
700	712.0331	2.681	-8.533	0.282
725	712.0331	2.681	-8.389	0.278
750	741.7536	2.681	-7.543	0.324
850	856.0000	2.681	-8.668	0.287
700	705.9943	2.761	-8.373	0.870
650	659.5325	2.811	-8.462	0.319
675	659.5325	2.811	-8.419	0.301
675	667.5270	2.811	-8.535	0.181
650	652.7311	2.851	-8.834	0.289
675	669.3842	2.851	-8.694	0.176
650	645.0851	2.851	-8.519	0.233
750	761.0477	2.851	-8.474	0.371
775	761.0477	2.851	-8.117	0.376
650	649.8760	2.903	-9.003	0.715
625	634.1680	2.903	-8.838	0.422
600	590.7636	3.016	-9.197	0.707
675	686.5686	3.016	-8.904	0.336
700	686.5686	3.016	-8.735	0.377
800	790.5747	3.040	-9.062	0.274
725	739.2405	3.040	-9.152	0.299
750	739.2405	3.040	-8.967	0.279
725	719.5230	3.040	-8.609	0.330

Table E.17: Ba I Electronic State Distributions at 150 mTorr, 36.0 mm – Continued

Window (nm)	λ (nm)	E_i (eV)	Ln(R_{pop})	σ
575	582.6274	3.318	-10.230	0.153
550	551.9044	3.573	-11.098	0.351
575	580.0230	3.573	-11.067	0.344
575	577.7618	3.581	-11.573	0.301

Table E.18: Cu I Electronic State Distributions at 150 mTorr, 36.0 mm

Window (nm)	λ (nm)	E_i (eV)	Ln(R_{pop})	σ
500	510.5540	3.577	-7.030	0.531
525	510.5540	3.577	-7.142	0.390
575	570.0200	3.577	-7.464	0.590
800	793.3130	5.013	-9.869	0.331
800	809.2631	5.013	-10.144	0.305
525	515.3240	5.803	-12.526	0.431
525	521.8200	5.804	-12.382	0.435

E.7 150 mTorr, 45.7 mm

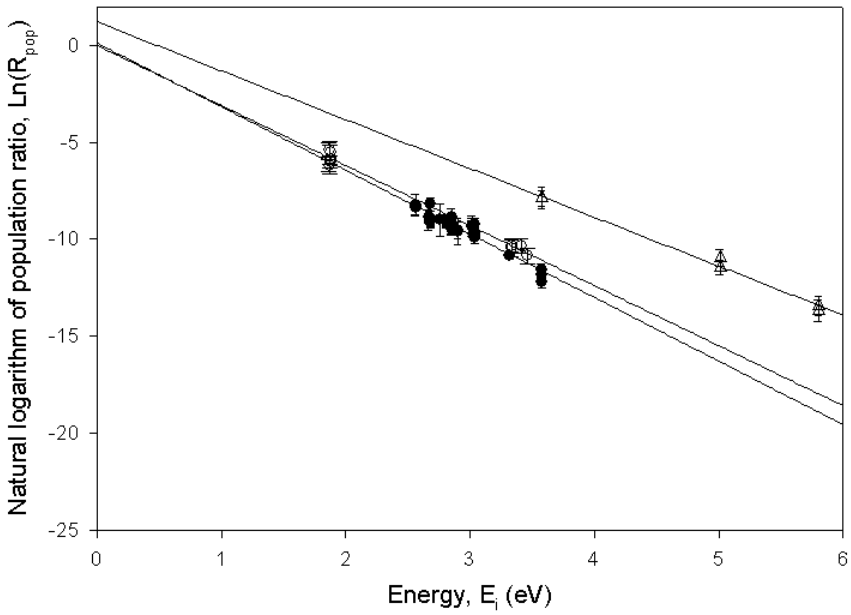

Figure E.7: Electronic State Distributions at 150 mTorr, 45.7 mm. (○ Y I, • Ba I, △ Cu I)

Table E.19: Y I Electronic State Distributions at 150 mTorr, 45.7 mm

Window (nm)	λ (nm)	E_i (eV)	Ln(R_{pop})	σ
650	643.5000	1.867	-6.201	0.292
625	622.2590	1.867	-5.387	0.361
625	619.1730	1.876	-6.024	0.300
625	640.2010	1.876	-5.871	0.738
650	640.2010	1.876	-5.541	0.576
550	563.0130	3.334	-10.443	0.436
575	563.0130	3.334	-10.321	0.355
550	552.7540	3.412	-10.362	0.366
550	546.6460	3.465	-10.866	0.381

Table E.20: Ba I Electronic State Distributions at 150 mTorr, 45.7 mm

Window (nm)	λ (nm)	E_i (eV)	Ln(R_{pop})	σ
775	767.2085	2.564	-8.232	0.533
775	778.0478	2.564	-8.384	0.360
725	728.0296	2.667	-8.831	0.692
750	748.8075	2.667	-8.850	0.346
700	712.0331	2.681	-9.075	0.284
725	712.0331	2.681	-9.016	0.278
750	741.7536	2.681	-8.189	0.330
850	856.0000	2.681	-9.131	0.289
700	705.9943	2.761	-9.002	0.839
650	659.5325	2.811	-9.109	0.315
675	659.5325	2.811	-9.062	0.300
675	667.5270	2.811	-9.125	0.184
650	652.7311	2.851	-9.491	0.286
675	669.3842	2.851	-9.299	0.178
650	645.0851	2.851	-9.192	0.235
750	761.0477	2.851	-9.318	0.407
775	761.0477	2.851	-8.831	0.403
650	649.8760	2.903	-9.612	0.694
625	634.1680	2.903	-9.512	0.428
675	686.5686	3.016	-9.325	0.539
700	686.5686	3.016	-9.371	0.349
800	790.5747	3.040	-9.777	0.281
725	739.2405	3.040	-9.924	0.305
750	739.2405	3.040	-9.676	0.283
725	719.5230	3.040	-9.234	0.330
575	582.6274	3.318	-10.846	0.162

Table E.20: Ba I Electronic State Distributions at 150 mTorr, 45.7 mm – Continued

Window (nm)	λ (nm)	E_i (eV)	Ln(R_{pop})	σ
550	551.9044	3.573	-11.804	0.367
575	580.0230	3.573	-11.602	0.361
575	577.7618	3.581	-12.190	0.311

Table E.21: Cu I Electronic State Distributions at 150 mTorr, 45.7 mm

Window (nm)	λ (nm)	E_i (eV)	Ln(R_{pop})	σ
500	510.5540	3.577	-7.878	0.560
525	510.5540	3.577	-7.894	0.408
800	793.3130	5.013	-10.967	0.424
800	809.2631	5.013	-11.451	0.384
525	515.3240	5.803	-13.694	0.548
525	521.8200	5.804	-13.433	0.507

E.8 150 mTorr, 55.0 mm

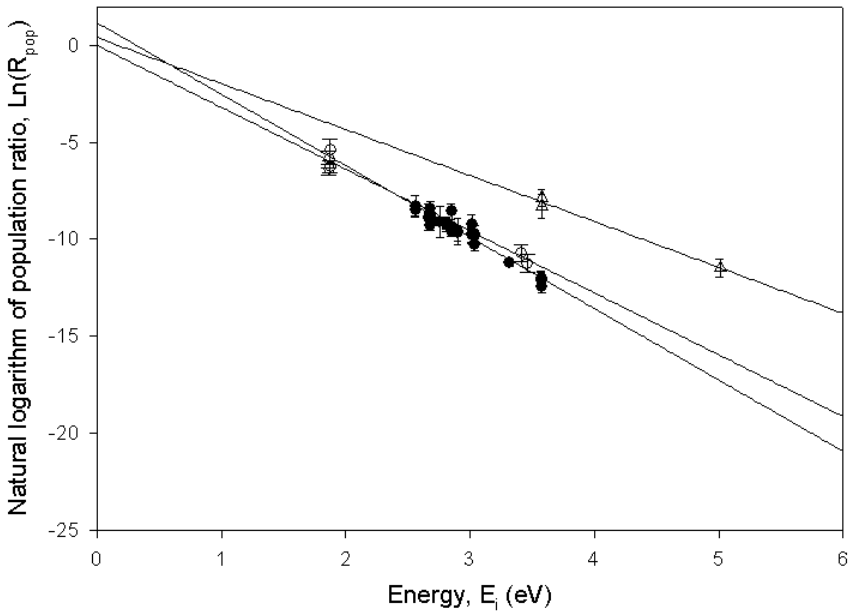

Figure E.8: Electronic State Distributions at 150 mTorr, 55.0 mm. (○ Y I, • Ba I, △ Cu I)

Table E.22: Y I Electronic State Distributions at 150 mTorr, 55.0 mm

Window (nm)	λ (nm)	E_i (eV)	Ln(R_{pop})	σ
650	643.5000	1.867	-6.408	0.301
625	622.2590	1.867	-5.868	0.422
625	619.1730	1.876	-6.249	0.307
650	640.2010	1.876	-5.393	0.552
550	552.7540	3.412	-10.699	0.422
550	546.6460	3.465	-11.264	0.458

Table E.23: Ba I Electronic State Distributions at 150 mTorr, 55.0 mm

Window (nm)	λ (nm)	E_i (eV)	Ln(R_{pop})	σ
775	767.2085	2.564	-8.287	0.529
775	778.0478	2.564	-8.502	0.364

Table E.23: Ba I Electronic State Distributions at 150 mTorr, 55.0 mm – Continued

Window (nm)	λ (nm)	E_i (eV)	Ln(R_{pop})	σ
725	728.0296	2.667	-8.878	0.681
750	748.8075	2.667	-8.899	0.350
700	712.0331	2.681	-8.804	0.446
725	712.0331	2.681	-8.665	0.442
750	741.7536	2.681	-8.423	0.391
850	856.0000	2.681	-9.263	0.295
700	705.9943	2.761	-9.100	0.821
650	659.5325	2.811	-9.276	0.317
675	659.5325	2.811	-9.165	0.297
675	667.5270	2.811	-9.281	0.186
650	652.7311	2.851	-9.576	0.286
675	669.3842	2.851	-9.399	0.179
650	645.0851	2.851	-9.350	0.243
775	761.0477	2.851	-8.559	0.399
650	649.8760	2.903	-9.584	0.682
625	634.1680	2.903	-9.692	0.430
600	590.7636	3.016	-9.246	0.543
675	686.5686	3.016	-9.797	0.393
700	686.5686	3.016	-9.725	0.455
800	790.5747	3.040	-9.847	0.292
725	739.2405	3.040	-10.253	0.333
750	739.2405	3.040	-9.853	0.298
725	719.5230	3.040	-9.718	0.398
575	582.6274	3.318	-11.218	0.177
550	551.9044	3.573	-12.036	0.412
575	580.0230	3.573	-12.118	0.413

Table E.23: Ba I Electronic State Distributions at 150 mTorr, 55.0 mm – Continued

Window (nm)	λ (nm)	E_i (eV)	Ln(R_{pop})	σ
575	577.7618	3.581	-12.451	0.322

Table E.24: Cu I Electronic State Distributions at 150 mTorr, 55.0 mm

Window (nm)	λ (nm)	E_i (eV)	Ln(R_{pop})	σ
500	510.5540	3.577	-8.283	0.619
525	510.5540	3.577	-7.883	0.434
800	809.2631	5.013	-11.491	0.443

E.9 400 mTorr, 31.4 mm

Table E.25: Y I Electronic State Distributions at 400 mTorr, 31.4 mm

Window (nm)	λ (nm)	E_i (eV)	Ln(R_{pop})	σ
650	643.5000	1.867	-5.740	0.300
625	622.2590	1.867	-4.451	0.382
625	619.1730	1.876	-5.395	0.314
650	640.2010	1.876	-4.433	0.477
550	563.0130	3.334	-9.205	0.392
575	563.0130	3.334	-9.093	0.332
575	567.5270	3.334	-8.247	0.401
550	552.7540	3.412	-9.155	0.345
550	560.6330	3.412	-9.289	0.724
575	560.6330	3.412	-8.783	0.448
550	546.6460	3.465	-9.543	0.350

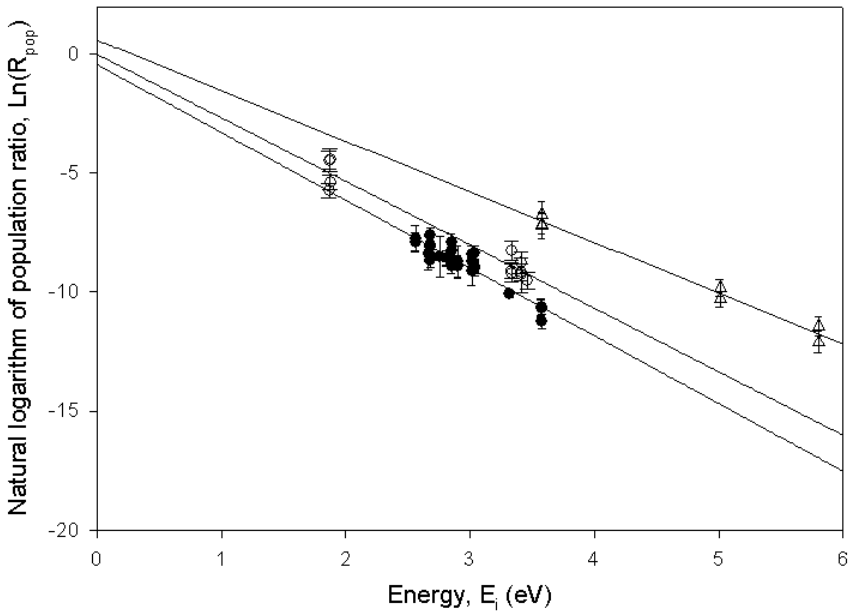

Figure E.9: Electronic State Distributions at 400 mTorr, 31.4 mm. (○ Y I, • Ba I, △ Cu I)

Table E.26: Ba I Electronic State Distributions at 400 mTorr, 31.4 mm

Window (nm)	λ (nm)	E_i (eV)	Ln(R_{pop})	σ
775	767.2085	2.564	-7.760	0.542
775	778.0478	2.564	-7.889	0.364
725	728.0296	2.667	-8.353	0.706
750	748.8075	2.667	-8.389	0.349
700	712.0331	2.681	-8.104	0.452
725	712.0331	2.681	-8.012	0.448
750	741.7536	2.681	-7.610	0.329
850	856.0000	2.681	-8.668	0.289
700	705.9943	2.761	-8.524	0.856
650	659.5325	2.811	-8.583	0.327
675	659.5325	2.811	-8.563	0.304
675	667.5270	2.811	-8.538	0.184

Table E.26: Ba I Electronic State Distributions at 400 mTorr, 31.4 mm – Continued

Window (nm)	λ (nm)	E_i (eV)	Ln(R_{pop})	σ
650	652.7311	2.851	-8.913	0.295
675	669.3842	2.851	-8.687	0.178
650	645.0851	2.851	-8.609	0.245
750	761.0477	2.851	-8.283	0.344
775	761.0477	2.851	-7.925	0.361
650	649.8760	2.903	-8.736	0.703
625	634.1680	2.903	-8.897	0.451
600	590.7636	3.016	-9.113	0.596
675	686.5686	3.016	-8.689	0.334
700	686.5686	3.016	-8.431	0.350
800	790.5747	3.040	-8.928	0.276
725	739.2405	3.040	-9.033	0.295
750	739.2405	3.040	-8.902	0.277
725	719.5230	3.040	-8.379	0.316
575	582.6274	3.318	-10.076	0.166
550	551.9044	3.573	-10.643	0.349
575	580.0230	3.573	-10.689	0.358
575	577.7618	3.581	-11.231	0.308

Table E.27: Cu I Electronic State Distributions at 400 mTorr, 31.4 mm

Window (nm)	λ (nm)	E_i (eV)	Ln(R_{pop})	σ
500	510.5540	3.577	-7.200	0.560
525	510.5540	3.577	-7.129	0.409
575	570.0200	3.577	-6.743	0.542
800	793.3130	5.013	-9.817	0.349
800	809.2631	5.013	-10.290	0.328

Table E.27: Y I Electronic State Distributions at 400 mTorr, 31.4 mm – Continued

Window (nm)	λ (nm)	E_i (eV)	Ln(R_{pop})	σ
525	515.3240	5.803	-12.114	0.458
525	521.8200	5.804	-11.428	0.407

E.10 400 mTorr, 36.0 mm

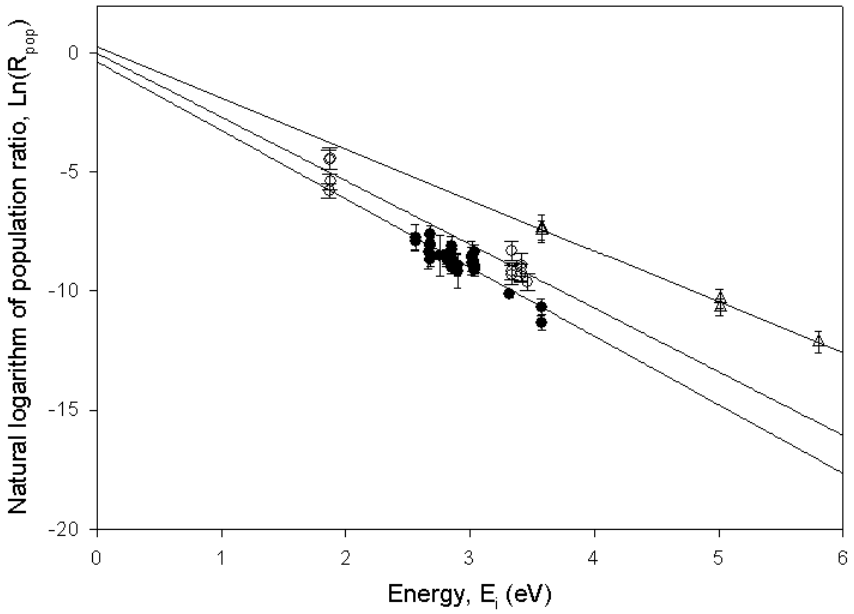

Figure E.10: Electronic State Distributions at 400 mTorr, 36.0 mm. (○ Y I, • Ba I, △ Cu I)

Table E.28: Y I Electronic State Distributions at 400 mTorr, 36.0 mm

Window (nm)	λ (nm)	E_i (eV)	Ln(R_{pop})	σ
650	643.5000	1.867	-5.769	0.298
625	622.2590	1.867	-4.477	0.405
625	619.1730	1.876	-5.407	0.322
650	640.2010	1.876	-4.420	0.457
550	563.0130	3.334	-9.307	0.402
575	563.0130	3.334	-9.170	0.333

Table E.28: Y I Electronic State Distributions at 400 mTorr, 36.0 mm – Continued

Window (nm)	λ (nm)	E_i (eV)	Ln(R_{pop})	σ
575	567.5270	3.334	-8.300	0.402
550	552.7540	3.412	-9.228	0.349
550	560.6330	3.412	-9.003	0.617
575	560.6330	3.412	-8.891	0.454
550	546.6460	3.465	-9.612	0.354

Table E.29: Ba I Electronic State Distributions at 400 mTorr, 36.0 mm

Window (nm)	λ (nm)	E_i (eV)	Ln(R_{pop})	σ
775	767.2085	2.564	-7.739	0.547
775	778.0478	2.564	-7.906	0.368
725	728.0296	2.667	-8.355	0.709
750	748.8075	2.667	-8.340	0.350
700	712.0331	2.681	-8.102	0.334
725	712.0331	2.681	-8.020	0.329
750	741.7536	2.681	-7.584	0.334
850	856.0000	2.681	-8.657	0.292
700	705.9943	2.761	-8.497	0.861
650	659.5325	2.811	-8.657	0.326
675	659.5325	2.811	-8.539	0.303
675	667.5270	2.811	-8.603	0.184
650	652.7311	2.851	-8.999	0.294
675	669.3842	2.851	-8.703	0.177
650	645.0851	2.851	-8.606	0.241
750	761.0477	2.851	-8.244	0.354
775	761.0477	2.851	-8.086	0.399
650	649.8760	2.903	-9.150	0.715

Table E.29: Ba I Electronic State Distributions at 400 mTorr, 36.0 mm – Continued

Window (nm)	λ (nm)	E_i (eV)	Ln(R_{pop})	σ
625	634.1680	2.903	-8.902	0.462
600	590.7636	3.016	-8.613	0.695
675	686.5686	3.016	-8.811	0.339
700	686.5686	3.016	-8.525	0.363
800	790.5747	3.040	-8.993	0.276
725	739.2405	3.040	-9.096	0.296
750	739.2405	3.040	-8.919	0.280
725	719.5230	3.040	-8.377	0.314
575	582.6274	3.318	-10.118	0.165
550	551.9044	3.573	-10.674	0.350
575	580.0230	3.573	-10.702	0.354
575	577.7618	3.581	-11.315	0.309

Table E.30: Cu I Electronic State Distributions at 400 mTorr, 36.0 mm

Window (nm)	λ (nm)	E_i (eV)	Ln(R_{pop})	σ
500	510.5540	3.577	-7.354	0.576
525	510.5540	3.577	-7.455	0.418
800	793.3130	5.013	-10.344	0.403
800	809.2631	5.013	-10.678	0.354
525	521.8200	5.804	-12.156	0.447

E.11 400 mTorr, 45.7 mm

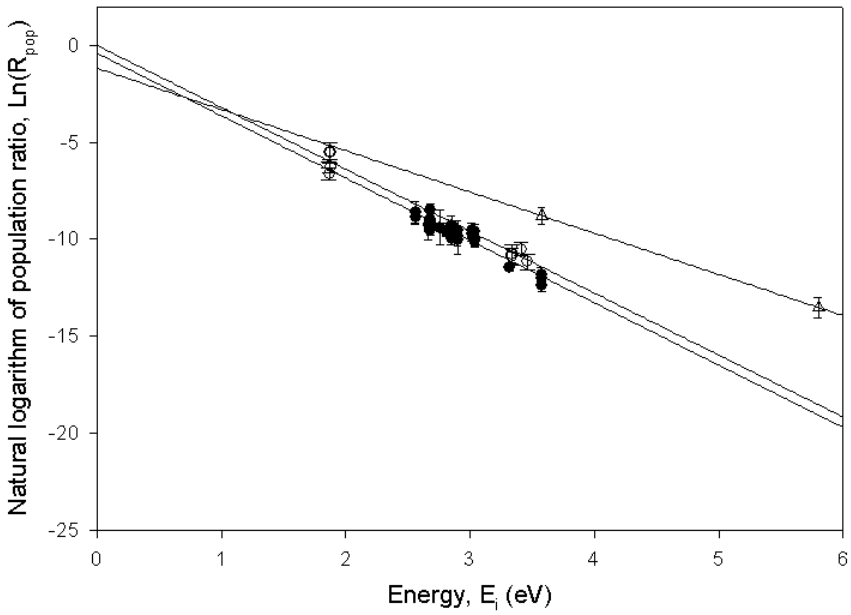

Figure E.11: Electronic State Distributions at 400 mTorr, 45.7 mm. (○ Y I, • Ba I, △ Cu I)

Table E.31: Y I Electronic State Distributions at 400 mTorr, 45.7 mm

Window (nm)	λ (nm)	E_i (eV)	Ln(R_{pop})	σ
650	643.5000	1.867	-6.632	0.298
625	622.2590	1.867	-5.506	0.496
625	619.1730	1.876	-6.240	0.337
650	640.2010	1.876	-5.541	0.509
550	563.0130	3.334	-10.767	0.475
575	563.0130	3.334	-10.901	0.409
550	552.7540	3.412	-10.499	0.370
550	546.6460	3.465	-11.159	0.401

Table E.32: Ba I Electronic State Distributions at 400 mTorr, 45.7 mm

Window (nm)	λ (nm)	E_i (eV)	Ln(R_{pop})	σ
775	767.2085	2.564	-8.590	0.562
775	778.0478	2.564	-8.861	0.375
725	728.0296	2.667	-9.292	0.737
750	748.8075	2.667	-9.222	0.359
700	712.0331	2.681	-9.084	0.469
725	712.0331	2.681	-8.951	0.463
750	741.7536	2.681	-8.513	0.363
850	856.0000	2.681	-9.520	0.296
700	705.9943	2.761	-9.401	0.895
650	659.5325	2.811	-9.512	0.344
675	659.5325	2.811	-9.520	0.329
675	667.5270	2.811	-9.636	0.198
650	652.7311	2.851	-9.944	0.313
675	669.3842	2.851	-9.713	0.189
650	645.0851	2.851	-9.587	0.254
775	761.0477	2.851	-9.259	0.451
650	649.8760	2.903	-10.046	0.741
625	634.1680	2.903	-9.852	0.498
650	634.1680	2.903	-9.535	0.463
675	686.5686	3.016	-9.724	0.363
700	686.5686	3.016	-9.523	0.386
800	790.5747	3.040	-10.103	0.304
725	739.2405	3.040	-10.062	0.305
750	739.2405	3.040	-9.915	0.289
725	719.5230	3.040	-9.589	0.348
575	582.6274	3.318	-11.439	0.188

Table E.32: Ba I Electronic State Distributions at 400 mTorr, 45.7 mm – Continued

Window (nm)	λ (nm)	E_i (eV)	Ln(R_{pop})	σ
550	551.9044	3.573	-11.995	0.376
575	580.0230	3.573	-11.836	0.378
575	577.7618	3.581	-12.402	0.319

Table E.33: Cu I Electronic State Distributions at 400 mTorr, 45.7 mm

Window (nm)	λ (nm)	E_i (eV)	Ln(R_{pop})	σ
525	510.5540	3.577	-8.792	0.449
525	515.3240	5.803	-13.532	0.504

E.12 Electronic Temperatures

Table E.34: Summary of Calculated Electronic Temperatures (in eV)

Pressure (mTorr) / distance (mm)	Y I	Ba I	Cu I
50 / 31.4	0.35 ± 0.01	0.29 ± 0.01	0.41 ± 0.02
50 / 36.0	0.35 ± 0.01	0.30 ± 0.01	0.42 ± 0.02
50 / 45.7	0.28 ± 0.01	0.27 ± 0.01	0.39 ± 0.03
50 / 55.0	0.31 ± 0.02	0.29 ± 0.01	0.41 ± 0.01
150 / 31.4	0.37 ± 0.02	0.32 ± 0.02	0.50 ± 0.05
150 / 36.0	0.36 ± 0.02	0.30 ± 0.02	0.44 ± 0.03
150 / 45.7	0.32 ± 0.01	0.30 ± 0.02	0.40 ± 0.02
150 / 55.0	0.31 ± 0.02	0.27 ± 0.01	0.42 ± 0.04
400 / 31.4	0.37 ± 0.03	0.35 ± 0.03	0.47 ± 0.03
400 / 36.0	0.37 ± 0.03	0.35 ± 0.03	0.47 ± 0.02
400 / 45.7	0.31 ± 0.02	0.31 ± 0.02	0.47 ± ***

*** Insufficient data points to estimate error

E.13 Y-intercepts of population plots

Table E.35: Y-intercepts of population plots

Pressure/distance (mTorr) / (mm)	Y I	Ba I	Cu I
50 / 31.4	7.10E-14 ± 0.30	0.78 ± 0.35	1.37 ± 0.66
50 / 36.0	1.08E-02 ± 0.22	0.39 ± 0.39	1.00 ± 0.49
50 / 45.7	2.50E-05 ± 0.44	0.05 ± 0.41	0.37 ± 0.87
50 / 55.0	2.88E-05 ± 0.45	0.05 ± 0.34	0.43 ± 0.42
150 / 31.4	3.55E-05 ± 0.34	0.27 ± 0.60	0.15 ± 0.94
150 / 36.0	2.83E-05 ± 0.34	0.85 ± 0.59	1.05 ± 0.65
150 / 45.7	2.31E-05 ± 0.32	0.12 ± 0.59	1.21 ± 0.59
150 / 55.0	-2.56E-05 ± 0.58	1.17 ± 0.57	0.41 ± 0.99
400 / 31.4	-2.16E-05 ± 0.59	0.44 ± 0.65	0.60 ± 0.57
400 / 36.0	-3.23E-05 ± 0.59	-0.36 ± 0.67	0.25 ± 0.34
400 / 45.7	-1.86E-05 ± 0.56	-0.40 ± 0.60	-1.17 ± ***

*** Insufficient data points to estimate error

Bibliography

1. *Pi-Max Gated ICCD Cameras for Imaging and Spectroscopy.* Product brochure, Princeton Instruments.
2. "Spectra Pro 2000 Series Monochromators and Spectrographs". Brochure.
3. *CRC Handbook of Chemistry and Physics.* CRC Press, Boca Raton, 82nd edition, 2001.
4. "Tablecurve 2D V 5.01", 2001.
5. "Peakfit V 4.11", 2002.
6. "Atomic Spectra Database". physics.nist.gov/PhysRefData/ASD/index.html, August 2005.
7. Abrikosov, A.A. "Type II Superconductors and the Vortex Lattice". Nobel Lecture, December 2003.
8. Al-Wazzan, R.A., J.M. Hendron, and T. Morrow. "Spatially and temporally resolved emission intensities and number densities in low temperature laser-induced plasmas in vacuum and in ambient gases". *Applied Surface Science*, 96-98:170–174, 1996.
9. Apostol, I., R. Stoian, C. Luculescu, R. Dabu, and A. Stratan. "Ablation threshold and plasma analysis in the PLD process". *Proceedings of the SPIE*, 3404:243–247, 1998.
10. Auciello, O., S. Athavaie, O.E. Hankins, M. Sito, A.F. Schreiner, and N. Biunno. "Spectroscopic analysis of electronically excited species in XeCl excimer laser-induced plasmas from the ablated high-temperature superconductor $YBa_2Cu_3O_7$". *Applied Physics Letters*, 53(1):72–74, July 1988.
11. Becker, R., G. Heller, and F. Sauter. "Über die Stromverteilung in einer Supraleitenden Kugel". *Zeitschrift Für Physik*, 85:772–787, 1933.
12. Bednorz, J.G. and K.A. Muller. "Perovskite-type Oxides - The New Approach to High T_c Superconductivity". Nobel Lecture, December 1987.
13. Bernath, P. *Spectra of Atoms and Molecules.* Oxford University Press, New York, 1995.
14. Bevington, P. and D. Robinson. *Data Reduction and Error Analysis for the Physical Sciences.* McGraw-Hill, New York, 2nd edition, 1992.
15. Biggers, R. Personal Communication, February 2005.
16. Blackstead, H.A. and J.D. Dow. "The Nature of a Correct Theory of High-Temperature Superconductivity". *Physica C*, 341-348:187–188, 2000.

17. Boyd, R.W. *Radiometry and the Detection of Optical Radiation.* John Wiley & Sons, New York, 1983.

18. Cava, R.J. "Oxide Superconductors". *Journal of the American Ceramic Society*, 83(1):5–28, 2000.

19. Chen, C.H., M.P. McCann, and R.C. Phillips. "Real-time monitoring of laser ablation deposition of superconductors by fluorescence and secondary-ion spectra". *Applied Physics Letters*, 53(26):2701–2703, December 1988.

20. Chu, C.W. "High-Temperature Superconducting Materials: A Decade of Impressive Advancement in T_c". *IEEE Transactions on Applied Superconductivity*, 7(2):80–89, June 1997.

21. Cooper, L.N. "Microscopic Quantum Interference Effects in the Theory of Superconductivity". Nobel Lecture, December 1972.

22. Cyrot, M. "Ginzburg-Landau theory for Superconductors". *Reports on Progress in Physics*, 36(2):103–158, February 1973.

23. Demtröder, Wolfgang. *Laser Spectroscopy.* Springer, New York, 2nd edition, 1982.

24. Dow, J.D., H.A. Blackstead, and D.R. Harshman. "High-temperature superconductivity: the roles of oxide layers". *Physica C*, 364-365:74–78, 2001.

25. Druffner, C.J., P.D. Kee, M.A. Lange, G.P. Perram, R.R. Biggers, and P.N. Barnes. "Optical Diagnostics for the Pulsed Laser Deposition of $YBa_2Cu_3O_{7-x}$ Superconducting Wires". *Proceedings of the SPIE*, 5448:153–164, September 2004.

26. Druffner, C.J., G.P. Perram, and R.R. Biggers. "Time-of-flight emission profiles of the entire plume using fast imaging during pulsed laser deposition of $YBa_2Cu_3O_{7-x}$". *Review of Scientific Instruments*, 76, September 2005.

27. Dyer, P.E., R.D. Greenough, A. Issa, and P.H. Key. "Spectroscopic and ion probe measurements of KrF laser ablated Y-Ba-Cu-O bulk samples". *Applied Physics Letters*, 53(6):534–536, August 1988.

28. El-Astal, A.H., S. Ikram, T. Morrow, W.G. Graham, and D.G. Walmsley. "A quantitative investigation of emission from low temperature laser-induced $YBa_2Cu_3O_x$ plasma plumes". *Journal of Applied Physics*, 77(12):6572–6580, June 1995.

29. El-Astal, A.H., T. Morrow, W.G. Graham, and D.G. Walmsley. "The role of gas-phase oxidation and combination during laser deposition of $YBa_2Cu_3O_{7-x}$ in ambient oxygen". *Superconducting Science and Technology*, 8:529–533, 1995.

30. El-Hofy, M.I. "Relationship between critical temperature, oxygen deficiency and Meissner fraction in $YBa_2Cu_3O_{7-\delta}$ superconductors". *Superconducting Science and Technology*, 10:403–408, 1997.

31. Faist, M.B. and R.D. Levine. "On the product electronic state distribution in reactions of alkali dimers with halogen atoms". *Chemical Physics Letters*, 47(1):5–10, April 1977.

32. Finnemore, D.K., K.E. Gray, M.P. Maley, D.O. Welch, D.K. Christen, and D.M. Kroeger. "Coated conductor development: an assessment". *Physica C*, 320(1-2):1–8, 1999.

33. Forrest, A.M. "Meissner and Ochsenfeld revisited". *European Journal of Physics*, 4(2):117–120, 1983.

34. Fried, D., G.P. Reck, T. Kushida, and E.W. Rothe. "Electric field enhancement of optical field emission from plasma plume generated during ArF excimer photoablation of BaO_2, Y_2O_3, CuO, and $YBa_2Cu_3O_7$". *Journal of Physics. D: Applied Physics*, 24:1065–1071, 1991.

35. Gavaler, J.R., M.A. Jonocko, and C.K. Jones. "Preparation and properties of high-T_c Nb-Ge films". *Journal of Applied Physics*, 45:3009–3013, July 1974.

36. Geohegan, D.B. "Fast intensified-CCD photography of $YBa_2Cu_3O_{7-x}$ laser ablation in vacuum and ambient oxygen". *Applied Physics Letters*, 60(22):2732–2734, June 1992.

37. Geohegan, D.B. and D.N. Mashburn. "Characterization of ground-state neutral and ion transport during laser ablation of $Y_1Ba_2Cu_3O_{7-x}$ using transient optical absorption spectroscopy". *Applied Physics Letters*, 55(22):2345–2347, November 1989.

38. Geohegan, D.B. and A.A. Puretzky. "Dynamics of laser ablation plume penetration through low pressure background gases". *Applied Physics Letters*, 67(2):197–199, July 1995.

39. Geyer, T.J. and W.A. Weimer. "Spectral characteristics of plasma emission during ArF excimer laser ablation of $YBa_2Cu_3O_7$". *Applied Physics Letters*, 54(5):469–471, January 1989.

40. Geyer, T.J. and W.A. Weimer. "Parametric effects on plasma emission produced during excimer laser ablation of $YBa_2Cu_3O_{7-x}$". *Applied Spectroscopy*, 44(10):1659–1664, 1990.

41. Ginzburg, V.L. "On superconductivity and superfluidity (what I have and have not managed to do), as well as on the 'physical minimum' at the beginning of the XXI century". Nobel Lecture, December 2003.

42. Göres, J., P.J. Kung, D.B. Fenner, and J.I. Budnick. "In situ plume emission monitoring during pulsed-laser deposition of $YBa_2Cu_3O_{7-\delta}$ and yttria-stablized zirconia thin films". *Review of Scientific Instruments*, 68(1):170–177, January 1997.

43. Griem, H.R. *Plasma Spectroscopy*. McGraw-Hill, New York, 1964.

44. Griem, H.R. *Spectral Line Broadening By Plasmas.* Academic Press, New York, 1974.

45. Harilal, S.S., C.V. Bindhu, V.P.N. Nampoori, and C.P.G. Vallabhan. "Temporal and Spatial Behavior of Electron Density and Temperature in a Laser-Produced Plasma from $YBa_2Cu_3O_7$". *Applied Spectroscopy*, 52(3):449–455, March 1998.

46. Huhtinen, H., J. Järvinen, R. Laiho, P. Paturi, and J. Raittila. "Laser deposition from a nanostructured YBaCuO target Analysis of the plume and growth kinetics of particles on $SrTiO_3$". *Journal of Applied Physics*, 90(3):1521–1528, August 2001.

47. Joo, J., J-G. Kim, and W. Nah. "Improvement of mechanical properties of YBCO-AG composite superconductors made by mixing with metallic Ag powder and solution". *Superconductor Science and Technology*, 11(7):645–649, 1998.

48. Joseph, M.R., N. Xu, and V. Majidi. "Time-resolved emission characteristics and temperature profiles of laser-induced plasmas in helium". *Spectrochimica Acta*, 49B(1):89–103, January 1994.

49. Kelly, R. "On the dual role of the Knudsen layer and unsteady, adiabatic expansion in pulse sputtering phenomena". *Journal of Chemical Physics*, 92(8):5047–5056, April 1990.

50. Kelly, R., A. Miotello, B. Braren, A. Gupta, and K. Casey. "Primary and secondary mechanisms in laser-pulse sputtering". *Nuclear Instruments and Methods in Physics Research*, B65(1-4):187–199, March 1992.

51. Klose, J.Z., J.R. Fuhr, and W.L. Wiese. "Critically evaluated atomic transition probabilities for Ba I and Ba II". *Journal of Physical and Chemical Reference Data*, 31(1):217–230, 2002.

52. Krenos, J.R. and J.C. Tully. "Statistical partitioning of electronic energy: Reactions of alkali dimers with halogen atoms". *Journal of Chemical Physics*, 62(2):420–424, January 1975.

53. Larbalestier, D., A. Gurevich, D.M. Feldmann, and A. Polyanskii. "High-T_c superconducting materials for electric power applications". *Nature*, 414:368–377, November 2001.

54. Li, Y., K. Zdun, L. Hope, J. Xie, S. Corcoran, Y Qiao, J. Reeves, K. Lenseth, and V. Selvamanickam. "Texture Development and Superconducting Properties of YBCO Thick Films Deposited on Buffered Metal Substrates at Various Deposition Rates". *IEEE Transactions on Applied Superconductivity*, 13(2):2758–2761, June 2003.

55. London, F. and H. London. "The Electromagnetic Equations of the Supraconductor". *Proceedings of the Royal Society*, A149:71–88, 1935.

56. Mao, X.L., M.A. Shannon, A.J. Fernandez, and R.E. Russo. "Temperature and Emission Spatial Profiles of Laser-Induced Plasmas during Ablation Using Time-Integrated Emission Spectroscopy". *Applied Spectroscopy*, 49(7):1054–1062, July 1995.

57. Migdalek, J. and W.E. Baylis. "Multiconfiguration Dirac-Fock calculations of two electric quadropole transitions in neutral barium". *Physical Review A*, 42:6897–6899, December 1990.

58. Misra, A., A. Mitra, and R.K. Thareja. "Diagnostics of laser ablated plasmas using fast photography". *Applied Physics Letters*, 74(7):929–931, February 1999.

59. Montgomery, D. *Design and Analysis of Experiments*. John Wiley & Sons, New York, 4th edition, 1997.

60. Namiotka, R.K., E. Ehrlacher, J. Sagle, M. Brewer, D.J. Namiotka, A.P. Hickman, A.D. Streater, and J. Huennekens. "Diffusion of the barium atoms in the 6s5d ^3D_J metastable levels and the $6s^2\ ^1S_0$ ground state through noble-gas perturbers". *Physical Review A*, 54(1):449–461, July 1996.

61. Nasser, E. *Fundamentals of Gaseous Ionization and Plasma Electronics*. John Wiley & Sons, New York, 1971.

62. Onnes, H.K. "Investigations into the properties of substances at low temperatures, which have led, amongst other things, to the preparation of liquid helium". Nobel Lecture, December 1913.

63. Otis, C.E. and R.W. Dreyfus. "Laser ablation of $YBa_2Cu_3O_{7-\delta}$ as probled by laser induced fluorescence spectroscopy". *Physical Review Letters*, 67(15):2102–2105, October 2001.

64. Pathria, R. *Statistical Mechanics*. Butterworth Heinemann, Oxford, 2nd edition, 1996.

65. Payling, R. and P. Larkins. *Optical Emission Lines of the Elements*. John Wiley & Sons, New York, 2000.

66. Pfender, E. *Gaseous Electronics*, chapter 5. Academic Press, 1979.

67. Phelps, C. Personal Communication, October 2006.

68. Phelps, C., C. Druffner, G. Perram, and R. Biggers. "Shock front dynamics in the pulsed laser deposition of $YBa_2Cu_3O_{7-x}$". *Journal of Physics D*, July 2007.

69. Qiao, Y., Y. Li, S. Sathiraju, J. Reeves, K. Lenseth, and V. Selvamanickam. "An overview of the coated conductor progress at IGC-SuperPower". *Physica C*, 382:48–51, 2002.

70. Ready, J.F. *Effects of Laser Radiation*. Academic Press, New York, 1971.

71. Reif, F. *Fundamentals of Statistical and Thermal Physics*. McGraw-Hill, New York, 1965.

72. Riley, D., L. Doyle, and R. Al-Wazzan. "Trapping of radiation in a $YBa_2Cu_3O_7$ plume". *Journal of Applied Physics*, 79(9):7223–7226, May 1996.

73. Saengar, K.L. "Time-resolved optical emission during laser ablation of Cu, CuO, and high-T_c superconductors: $Bi_{1.7}Sr_{1.3}Ca_2Cu_3O_x$ and $Y_1Ba_{1.7}Cu_{2.7}O_y$". *Journal of Applied Physics*, 66(9):4435–4440, November 1989.

74. Sakeek, H.F., T. Morrow, W.G. Graham, and D.G. Walmsley. "Optical absorption spectroscopy study of the role of plasma chemistry in $YBa_2Cu_3O_7$ pulsed laser deposition". *Applied Physics Letters*, 59(27):3631–3633, December 1991.

75. Sakeek, H.F., T. Morrow, W.G. Graham, and D.G. Walmsley. "Emission studies of the plume produced during $YBa_2Cu_3O_7$ film production by laser ablation". *Journal of Applied Physics*, 75(2):1138–1144, January 1994.

76. Selvamanickam, V., H.G. Lee, Y. Li, J. Reeves, Y. Qiao, Y.Y. Xie, K. Lenseth, G. Carota, M. Funk, K. Zdun, J. Xie, K. Likes, M. Jones, L. Hope, and D.W. Hazelton. "Scale Up of High-Performance Y-Ba-Cu-O Coated Conductors". *IEEE Transactions on Applied Superconductivity*, 13(2):2492–2495, June 2003.

77. Seyrafi, K. and S.A. Hovanessian. *Introduction to electro-optical imaging and tracking systems*. Artech House, Boston, 1993.

78. Singh, R.K. and D. Kumar. "Pulsed laser deposition and characterization of high-T_c $YBa_2Cu_3O_{7-x}$ superconducting thin films". *Materials Science and Engineering*, 22(4):113–185, April 1998.

79. Singh, R.K. and J. Narayan. "Pulsed laser evaporation technique for deposition of thin films: Physics and theoretical model". *Physical Reviw B*, 41(13):8843–8861, May 1990.

80. Slater, J.C. "Atomic Radii in Crystals". *Journal of Chemical Physics*, 41(10):3199–3204, November 1964.

81. Sobel'man, I.I., L.A. Vainshtein, and E.A. Yukov. *Excitation of Atoms and and Broadening of Spectral Lines*. Springer, New York, 2nd edition, 1995.

82. Steinfeld, J., J.S. Francisco, and W.L. Hase. *Chemical Kinetics and Dynamics*. Prentice Hall, Upper Saddle River, 2nd edition, 1998.

83. Svobodny, T.P. and R. Biggers. "The pulsed-laser plume dynamics: characterization and modeling". *Proceedings of the SPIE*, 4760:81–92, September 2002.

84. Taylor, G.I. "The Formation of a Blast Wave by a Very Intense Explosion. I. Theoretical Discussion". *Proceedings of the Royal Society of London. Series A, Mathematical and Physical Sciences*, 201(1065):159–174, March 1950.

85. Tinkham, M. *Introduction to Superconductivity*. McGraw-Hill, New York, 2nd edition, 1996.

86. Verdeyen, J. *Laser Electronics*. Prentice Hall, Engelwood Cliffs, 2nd edition, 1989.

87. Wadsworth, W., J.P. Dybwad, and F.M. D'Amico. "High-Speed Passive Imaging Spectrometer for Airborne Chemical Detection". *6th Joint Conference on Standoff Detection for Chemical and Biological Detection.*

88. Weimer, W.A. "Plasma emission from laser ablation of the high-temperature superconductor $YBa_2Cu_3O_7$". *Applied Physics Letters*, 52(25):2171–2173, June 1988.

89. Wiener, A. *An Investigation of the YO(A) → YO(X) Transition in the Pulsed Laser Deposition of Super-Conducting Yttrium Barium Copper Oxide* $YBa_2Cu_3O_{7-x}$. Master's thesis, Wright State University, April 2003.

90. Wu, X.D., B. Dutta, M.S. Hegde, A. Inam, T. Venkatesan, E.W. Chase, C.C. Chang, and R. Howard. "Optical spectroscopy: An in situ diagnostic for pulsed laser deposition of high T_c superconducting thin films". *Applied Physics Letters*, 54(2):179–181, January 1989.

91. Ying, Q.Y., D.T. Shaw, and H.S. Kwok. "Spectroscopic study of plasma-assisted laser deposition Y-Ba-Cu-O". *Applied Physics Letters*, 53(18):1762–1764, October 1988.

92. Zheng, J.P., Z.Q. Huang, D.T. Shaw, and H.S. Kwok. "Generation of high-energy atomic beams in laser-superconducting target interactions". *Applied Physics Letters*, 54(3):280–282, January 1989.

REPORT DOCUMENTATION PAGE

Form Approved
OMB No. 0704–0188

1. REPORT DATE *(DD–MM–YYYY)*	2. REPORT TYPE	3. DATES COVERED *(From — To)*
22–08–2008	Dissertation	Jun 2003 — Aug 2008

4. TITLE AND SUBTITLE

Electronic State Distributions
of $YBa_2Cu_3O_{7-x}$
Laser Ablated Plumes

5a. CONTRACT NUMBER

5b. GRANT NUMBER

5c. PROGRAM ELEMENT NUMBER

6. AUTHOR(S)

Patrick D. Kee

5d. PROJECT NUMBER

5e. TASK NUMBER

5f. WORK UNIT NUMBER

7. PERFORMING ORGANIZATION NAME(S) AND ADDRESS(ES)

Air Force Institute of Technology
Graduate School of Engineering and Management
2950 Hobson Way
WPAFB OH 45433-7765

8. PERFORMING ORGANIZATION REPORT NUMBER

AFIT/DSP/ENP/08-S05

9. SPONSORING / MONITORING AGENCY NAME(S) AND ADDRESS(ES)

Dr. Harold Weinstock
Air Force Office of Scientific Research/NE
Suite 325 Room 3112
875 N. Randolph St
Arlington, VA 22203

10. SPONSOR/MONITOR'S ACRONYM(S)

AFOSR

11. SPONSOR/MONITOR'S REPORT NUMBER(S)

12. DISTRIBUTION / AVAILABILITY STATEMENT

Approval for public release; distribution is unlimited.

13. SUPPLEMENTARY NOTES

14. ABSTRACT

Emission from YBCO laser-ablated plumes was studied to characterize the PLD process. A KrF laser was used to ablate a bulk YBCO target at oxygen pressures ranging from 50-400 mTorr. Spectra were collected for the 500-860 nm bandpass at target distances ranging from 31.4-55.0 mm. Line fluences were corrected for self-absorption, and state distributions were calculated using recently updated transition probabilities. Electronic temperatures ranged from 0.28 $\pm$ 0.01 eV to 0.37 $\pm$ 0.03 eV for Y I, 0.28 $\pm$ 0.01 eV to 0.35 $\pm$ 0.03 eV for Ba I, and 0.40 $\pm$ 0.02 eV to 0.48 $\pm$ 0.05 eV for Cu I–consistent with prior literature. Results were insensitive to position and oxygen pressure. Spectrally-filtered imagery was used to determine plume velocities, shock strengths, and time-of-flight curves. Effects of time-varying temperatures and number densities on observed state distributions were modeled, predicting a slight elevation of Cu temperatures compared to Ba. However, this was not sufficient to explain experimental results. Surprisal analysis of state distributions resulted in linear constraints, consistent with an exponential gap law for electronic excitation.

15. SUBJECT TERMS

YBCO, PLD, emission spectroscopy, superconductivity, materials

16. SECURITY CLASSIFICATION OF:			17. LIMITATION OF ABSTRACT	18. NUMBER OF PAGES	19a. NAME OF RESPONSIBLE PERSON
a. REPORT	b. ABSTRACT	c. THIS PAGE			Glen P. Perram
UU	UU	UU	UU	218	19b. TELEPHONE NUMBER *(include area code)* (937) 255–3636, ext 4504